Quantum Microwave to Optical Transduction with Light-Robust Superconducting Circuits

Thesis by
Steven Wood

In Partial Fulfillment of the Requirements for the
Degree of
Doctor of Philosophy

CALIFORNIA INSTITUTE OF TECHNOLOGY
Pasadena, California

2024
Defended February 7th, 2024

Steven Wood
ORCID: 0009-0004-2582-0627

ACKNOWLEDGEMENTS

To my advisor Oskar Painter, thank you for taking me on as a summer student when I was an undergrad and later accepting me into your group when I returned to Caltech as graduate student. Your approach to research, the level of rigour you demand of all your students, and your deep scientific insights have all been instrumental in shaping my scientific development. This thesis was in large part possible with the support and help of the members of the Painter group to whom I owe many thanks. To Alp Sipahigil, who was my first mentor at Caltech, your humor and scientific curiosity inspired me throughout my Ph.D even after you left for Berkeley. You provided guidance and encouragement when I needed it most for which I will always be grateful. To Srujan Meesala, working together with you on the transduction project was the most fulfilling part of my time at Caltech and would not have been possible without you. Our tag-team round-the-clock cleanroom pushes were a driving force to making this work possible and was an experience I will not soon forget. To Jash Banker, as my first office-mate, I really enjoyed our time together and wish we had more. To David Lake, your insufferable puns and word-play made bad days a little bit better. To Piero Chiappina, thanks for putting up with my endless gripes and complaints during our time working together. I enjoyed our many conversations and sharing an office with you over the years. To Barry Baker, thank you for keeping the labs running. To the QPG staff, especially Matthew McCoy, having you looking after our labs has made doing research so much easier. Thank you for doing such a great job. To Guy DeRose, Bert Mendoza, Lena Wolff, Kelly McKenzie, Alireza Ghaffari, Alex Wertheim, Tiffany Kimoto, Jennifer Palmer, and all the other KNI staff past and present, thank you for keeping KNI running so smoothly. It has been a blessing to have access to such an advanced and well maintained nanofabrication facility. To Christy Jenstad and Jennifer Blankenship, thank you for keeping the department together and well organized.

To my mentors prior to graduate school, Vallorie Peridier, Gerald Lopez, Darren Lipomi, Haim Bau, and Matthew Hunt, I owe all of my academic success to you. To all the friends I made during and prior to my time at Caltech, your support and company was invaluable to me. To my parents who have been with me on this journey not just for 6 years, but for the last 28 years. No amount of words can express my gratitude for all you have done. And last, but not least, my loving partner Brynn. Thank you for your unending support during the better part of the last decade.

ABSTRACT

Modern computing and communication technologies such as supercomputers and the internet are based on optically connected networks of microwave frequency information processors. In recent years, an analogous architecture has emerged for quantum networks with optically distributed entanglement between remote superconducting quantum processors, a leading platform for quantum computing. The high coherence, controllability and scalability of microwave frequency superconducting circuits are ideal test-beds for nodes of a quantum network, however, microwave photons are not well suited for transmission of quantum information over long distances due to the presence of a large thermal background at room temperature. Optical photons are ideal for quantum communication applications due to their low propagation loss and negligible thermal occupation at room temperature. Coherent transduction of single photons from the microwave to the optical domain has the potential to play a key role in quantum networking and distributed quantum computing. In this thesis, we present the design of a piezo-optomechanical quantum transducer where transduction is mediated by a strongly hybridized acoustic mode of a piezoacoustic cavity attached to an optomechanical crystal. Our design involves on-chip integration of a light-robust superconducting circuit with the piezo-optomechanical transducer. Absorption of stray photons from the optical pump used in the transduction process is known to cause excess decoherence and noise in the superconducting circuit. The recovery time of the superconducting circuit after the optical pulse sets a limit on the transducer repetition rate. We fabricate niobium nitride based superconducting circuits and test their response to illumination by a 1550nm laser. We find a bandwidth-limited recovery time of $\sim$ 1us, indicating that a repetition rate exceeding 10kHz should be possible. Combined with the expected efficiency and noise metrics of our design, we expect that a transducer in this parameter regime would be suitable to realize probabilistic schemes for remote entanglement of superconducting quantum processors. We show nonclassical microwave-optical photon correlations of the niobium nitride aluminum nitride transducer operated as a spontaneous parametric down conversion source. We go on to show the preparation and characterization of microwave-optical Bell states prepared by the transducer. And finally, we conclude by discussing the challenges with fabricating niobium nitride superconducting circuits and lithium niobate piezoacoustic devices on silicon-on-insulator substrates and provide steps towards

realizing our enhanced transducer design.

TABLE OF CONTENTS

LIST OF ILLUSTRATIONS

LIST OF TABLES

Part I

Part I: Light-robust aluminum nitride transducer

INTRODUCTION

Part I of this thesis is primarily concerned with the development of a light-robust aluminum nitride-based quantum transducer device that can convert microwave frequency photons from a superconducting qubit (f $\sim$ 5GHz) into optical photons in the telecommunications band (f $\sim$ 200THz). These optical photons can then be transmitted over long distances using low loss optical fibers at room temperature opening up prospects for quantum communication between remote superconducting qubit based quantum processors. There are many different schemes for quantum transduction including schemes based on cold atoms [1–3], rare earth ions [4–7], electro-optics [8–15], and electro/piezo-optomechanics [16–30]. In Part I, we develop a light-robust piezo-optomechanical quantum transducer device.

Our transducer device can be split into three parts: 1. A light-robust superconducting circuit to interface with microwave frequency quantum devices. 2. A piezo-acoustic component that converts microwave photons into microwave phonons using the piezo-electric effect. 3. An optomechanical component that subsequently converts the microwave phonons into optical photons using an optomechanical interaction. Building on past work done in the Painter group, we utilize a modified one dimensional silicon optomechanical crystal (1D-OMC) to mediate optomechanical coupling. A brief summary of the theory of cavity optomechanics and the basic concepts underlying 1D-OMC devices developed by past generations of students in the Painter group is summarized in Chapter 1. The design of the aluminum nitride (AlN) piezo-acoustic cavity and niobium nitride (NbN) circuit is presented in Chapter 2 and 3, respectively. These three independently designed parts are then connected together to form our full transducer device. Details of the design of the full device and analysis of the expected efficiency and added noise of the transducer are also presented in Chapter 3. In Chapter 4, we will discuss the fabrication and initial characterization of the NbN circuit presented in Chapter 3. Quantum transduction has several modes of operation which we will discuss the broad features of in Chapter 6. Chapters 7 and 8 will discuss the integration and nanofabrication challenges in realizing our light-robust NbN-AlN transducer device and subsequent characterization efforts. In the final two chapters of Part I we will discuss the measurement and operation of this transducer as a correlated photon pair generation source and measurements to prepare and characterize a microwave-optical Bell state.

Chapter 1

BACKGROUND: CAVITY OPTOMECHANICS AND 1D OPTOMECHANICAL CRYSTALS

In this chapter, we briefly introduce the theory of cavity optomechanics and the design of optomechanical devices used in the subsequent chapters. This discussion will be brief and focused mainly on one-dimensional optomechanical crystals (1D OMC). For a more complete review of the theory of cavity optomechanics see [31, 32]. For detailed studies of 1D OMC devices carried out in the Painter group see [33–37].

1.1 Cavity Optomechanics Hamiltonian

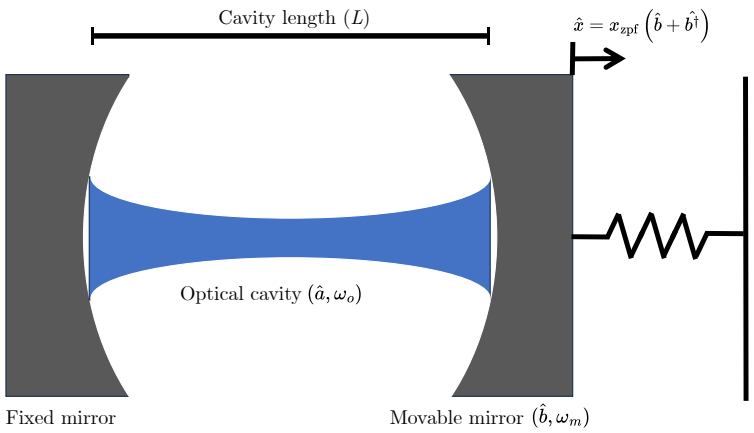

Figure 1.1: **Canonical cavity optomechanical system.** Consists of a Fabry-Perot optical cavity with one movable mirror depicted in the figure as a coupled spring system.

The canonical cavity optomechanical system shown in Fig.1.1 consists of a Fabry-Perot optical cavity where one mirror (of mass 'm') is attached to a spring and free to move (in direction 'x'). Optical photons entering this cavity exert a radiation pressure force which causes displacement of the mirror. This displacement changes the effective length of the Fabry-Perot cavity and modulates the cavity frequency. The Hamiltonian representing this system can be written as:

$$\hat{H} = \hbar\omega_c(x)\hat{a}^{\dagger}\hat{a} + \hbar\omega_m\hat{b}^{\dagger}\hat{b}. \tag{1.1}$$

Here the first term represents the optical cavity at frequency $\omega_c(x)$ which depends on the displacement 'x' of the movable mirror. The second term represents the mechanical motion of the mirror at frequency ω_m. The optical frequency can be written as $\omega_c(x) = 2\pi * c/(2(L+x))$, where c is the speed of light and L+x is the effective length of the Fabry-Perot cavity. For small displacement, $x \ll L$, we can approximate the frequency of the optical cavity as:

$$\begin{aligned} \omega_c(x) &= 2\pi \left(\frac{c}{2L}(1-x)\right) \\ &= \omega_o - \frac{x}{L}\omega_o, \end{aligned} \tag{1.2}$$

where $\omega_o = 2\pi * (c/2L)$ is the bare cavity frequency corresponding to x = 0. Identifying the position operator of the mechanical mode as $\hat{x} = x_{\text{zpf}}\left(\hat{b} + \hat{b^\dagger}\right)$, where $x_{\text{zpf}} = \sqrt{\hbar/(2m\omega_m)}$ is the zero-point motion of the mechanical oscillator, we arrive at the following Hamiltonian

$$\hat{H} = \hbar\omega_o \hat{a}^\dagger \hat{a} + \hbar\omega_m \hat{b}^\dagger \hat{b} - \hbar g_0 \hat{a}^\dagger \hat{a}\left(\hat{b} + \hat{b^\dagger}\right). \tag{1.3}$$

We define the single photon optomechanical coupling rate as $g_0 = \omega_o x_{\text{zpf}}/L$. While we derived the Hamiltonian in Eq.1.3 starting for a Fabry-Perot cavity with a mechanically compliant mirror, it is applicable to a wide variety of cavity optomechanical systems including the nanomechanical 1D optomechanical crystals we will use in this thesis. In our experiments, we will typically drive the optical cavity with a laser at frequency ω_L. We can rewrite the Hamiltonian in Eq.1.3 in a rotating frame at the laser frequency ω_L as

$$\hat{H} = -\hbar\Delta \hat{a}^\dagger \hat{a} + \hbar\omega_m \hat{b}^\dagger \hat{b} - \hbar g_0 \hat{a}^\dagger \hat{a}\left(\hat{b} + \hat{b^\dagger}\right), \tag{1.4}$$

where $\Delta = \omega_L - \omega_o$. The optical field consists of a large coherent part (α) with small quantum fluctuations ($\delta\hat{a}$), so we linearize the Hamiltonian by making the substitution $\hat{a} = \alpha + \delta\hat{a}$. We can then rewrite the interaction part of the Hamiltonian as

$$\begin{aligned} \hat{H_I} &= \hbar g_0 \hat{a}^\dagger \hat{a}\left(\hat{b} + \hat{b^\dagger}\right) \\ &= \hbar g_0 \left(\alpha + \delta\hat{a}^\dagger\right)(\alpha + \delta\hat{a})\left(\hat{b} + \hat{b}^\dagger\right) \\ &= \hbar g_0 \left(\hat{b} + \hat{b}^\dagger\right)\left(\alpha^2 + \alpha\delta\hat{a}^\dagger + \alpha\delta\hat{a} + \delta\hat{a}^\dagger\delta\hat{a}\right). \end{aligned} \tag{1.5}$$

The first term in the last line of Eq.1.5 is proportional to α^2 and corresponds to a static radiation pressure force exerted on the mechanical oscillator causing a constant

displacement. By redefining the origin of displacement we can ignore this term. The last term is smaller by a factor of α, so we will ignore this term too. As a result, we are left with

$$\hat{H}_I = \hbar g_0 \alpha \left(\delta\hat{a} + \delta\hat{a}^\dagger\right)\left(\hat{b} + \hat{b}^\dagger\right). \tag{1.6}$$

The full linearized Hamiltonian in the rotating frame is

$$\hat{H} = -\hbar\Delta\hat{a}^\dagger\hat{a} + \hbar\omega_m\hat{b}^\dagger\hat{b} - \hbar g_0\alpha\left(\delta\hat{a} + \delta\hat{a}^\dagger\right)\left(\hat{b} + \hat{b}^\dagger\right). \tag{1.7}$$

We identify $\alpha = \sqrt{n_{\text{cav}}}$ as the square root of the number of photons in the optical cavity and refer to $G = g_0\sqrt{n_{\text{cav}}}$ as the 'light-enhanced' optomechanical coupling rate.

1.2 Equations of Motion

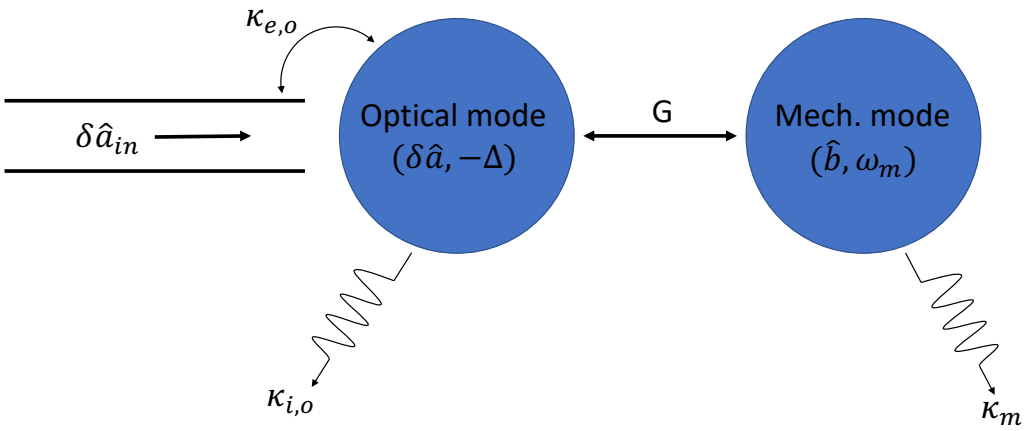

Figure 1.2: **Schematic of a driven optical cavity coupled to a mechanical mode.**

Using the linearized Hamiltonian of Eq.1.7 and applying input-output formalism to the case of a driven optical mode coupled to a mechanical mode as shown in Fig.1.2, we can express the equations of motion for the optical and mechanical fields as

$$\begin{aligned}
\delta\dot{\hat{a}} &= \left(i\Delta - \frac{\kappa_o}{2}\right)\delta\hat{a} + iG\left(b + b^\dagger\right) + \sqrt{\kappa_{e,o}}\delta\hat{a}_{in} + \sqrt{\kappa_{i,o}}\delta\hat{a}_{in,i} \\
\dot{\hat{b}} &= \left(-i\omega_m - \frac{\kappa_m}{2}\right)\hat{b} + iG\left(\delta\hat{a} + \delta\hat{a}^\dagger\right) + \sqrt{\kappa_m}\hat{b}_{in,i}.
\end{aligned} \tag{1.8}$$

Here κ_o is the total optical loss rate which we have divided into intrinsic loss $\kappa_{i,o}$ and extrinsic loss $\kappa_{e,o}$ as shown in Fig.1.2. κ_m is the total mechanics loss rate, $\delta\hat{a}_{in}$ is the input optical field, and $\delta\hat{a}_{in,i}$ and $\hat{b}_{in,i}$ are quantum noise operators for the optical and mechanical modes, respectively.

We can solve these coupled equations by Fourier transforming to the frequency domain which yields

$$\begin{aligned}\delta\hat{a}[\omega] &= \frac{-iG\left(\hat{b}[\omega]+\hat{b}^{\dagger}[\omega]\right)-\sqrt{\kappa_{e,o}}\delta\hat{a}_{in}[\omega]-\sqrt{\kappa_{i,o}}\delta\hat{a}_{in,i}[\omega]}{i\left(\Delta+\omega\right)-\frac{\kappa_o}{2}} \\ \hat{b}[\omega] &= \frac{-iG\left(\delta\hat{a}[\omega]+\delta\hat{a}^{\dagger}[\omega]\right)-\sqrt{\kappa_m}\hat{b}_{in,i}[\omega]}{i\left(\omega-\omega_m\right)-\frac{\kappa_m}{2}}.\end{aligned} \tag{1.9}$$

Substituting the expression for $\delta\hat{a}[\omega]$ in the expression for $\hat{b}[\omega]$ in Eq.1.9, it can be shown that the optomechanical interaction modifies the mechanical frequency as $\omega_m' = \omega_m + \delta\omega_m$ and also modifies the mechanical loss rate as $\kappa_m' = \kappa_m + \gamma_{om}$, where

$$\begin{aligned}\delta\omega_m &= \frac{G^2\omega_m}{\omega}\mathrm{Re}\left[\frac{1}{(\Delta+\omega)+i\frac{\kappa_o}{2}}+\frac{1}{(\Delta-\omega)-i\frac{\kappa_o}{2}}\right] \\ \gamma_{om} &= -\frac{2G^2\omega_m}{\omega}\mathrm{Im}\left[\frac{1}{(\Delta+\omega)+i\frac{\kappa_o}{2}}+\frac{1}{(\Delta-\omega)-i\frac{\kappa_o}{2}}\right].\end{aligned} \tag{1.10}$$

For the purpose of quantum transduction, we are particularly interested in the optomechanical damping rate γ_{om} at the mechanical frequency ($\omega = \omega_m$). Further, we make the following assumptions:

1. We are in the sideband resolved regime, defined by $\omega_m \gg \kappa_o$. For the transducer device considered in this thesis, $\omega_m \sim 2\pi \times 5\text{GHz}$ while $\kappa_o \sim 2\pi \times 500\text{MHz}$ so this assumption is justified.

2. We will drive our transducer device with a laser at a frequency (ω_L) that is detuned from the optical resonance by the mechanical frequency. $\omega_L = \omega_o - \omega_m \implies \Delta = -\omega_m$.

With these assumptions we find

$$\gamma_{om} = \frac{4g_0^2 n_{\text{cav}}}{\kappa_o}, \tag{1.11}$$

where we have explicitly written the optomechanical coupling G in terms of the single photon optomechanical coupling rate g_0 and the intra-cavity photon number n_{cav}.

Intuitively, with a red-detuned pump we are converting phonons from the mechanical mode into photons in the optical cavity. This is a parametric process where the laser drive acts as a pump to compensate for the frequency difference between

the phonons and the optical photons ($\omega_L = \omega_m - \omega_o$). The rate at which we can convert phonons to photons is given by the optomechanical scattering rate γ_{om} which is dependent on the laser pump power via the intra-cavity photon number n_{cav} as shown in 1.11 An important figure of merit is the optomechanical cooperativity defined as

$$C_{om} = \frac{\gamma_{om}}{\kappa_m}. \tag{1.12}$$

We can think of γ_{om} as the 'useful damping' rate where phonons in the mechanical mode are being converted into photons in the optical mode which we can then detect. κ_m on the other hand is the undesirable 'bad damping' rate where phonons in the mechanical mode are leaking out into the environment and being irretrievably lost. We can then understand the optomechanical cooperativity as the ratio of the 'useful damping' into the optical mode (γ_{om}) divided by the 'bad damping' κ_m. This will be a very important figure of merit to keep in mind when we discuss the performance of our quantum transducer device in Chapter 2.

1.3 1D Optomechanical Crystals

There are a wide variety of systems that have realized optomechanical coupling. These range from microscopic systems such as cold atoms coupled to an optical cavity [38, 39] to macroscopic, kilogram-scale suspended mirrors [40–42]. In our transducer, we will utilize a nanoscale device called a one-dimensional optomechanical crystal (1D OMC). We are interested in coupling microwave-frequency phonons ($\sim$ 5GHz) to telecom band photons ($\sim$ 200 THz). Due to the large difference in the velocity of light and sound, the wavelength of telecom band photons and microwave phonons is roughly equal ($\sim \mu m$ scale). This is convenient as it allows us to co-localize microwave-frequency mechanical modes and telecom band optical modes in the same wavelength scale device ($\sim \mu m$). From our expression for $g_0 = \omega_0 x_{\mathrm{zpf}}/L$, shrinking the length (L) of our optomechanical system down to the wavelength scale allows us to achieve large single photon optomechanical coupling. Here we describe the basic design of a 1D OMC. This topic has been covered in great detail in previous work from the Painter group so our discussion here will be brief.

A 1D optomechanical crystal is shown in Fig. 1.3 a. It consists of a nano-beam patterned from a 220 nm thick silicon device layer of a silicon on insulator substrate. By shrinking the thickness and width of the beam to be sub-wavelength, we get an effective 1D structure. At either end of the nano-beam, we have the 'mirror region' which consists of an array of identical periodically patterned elliptical holes that act

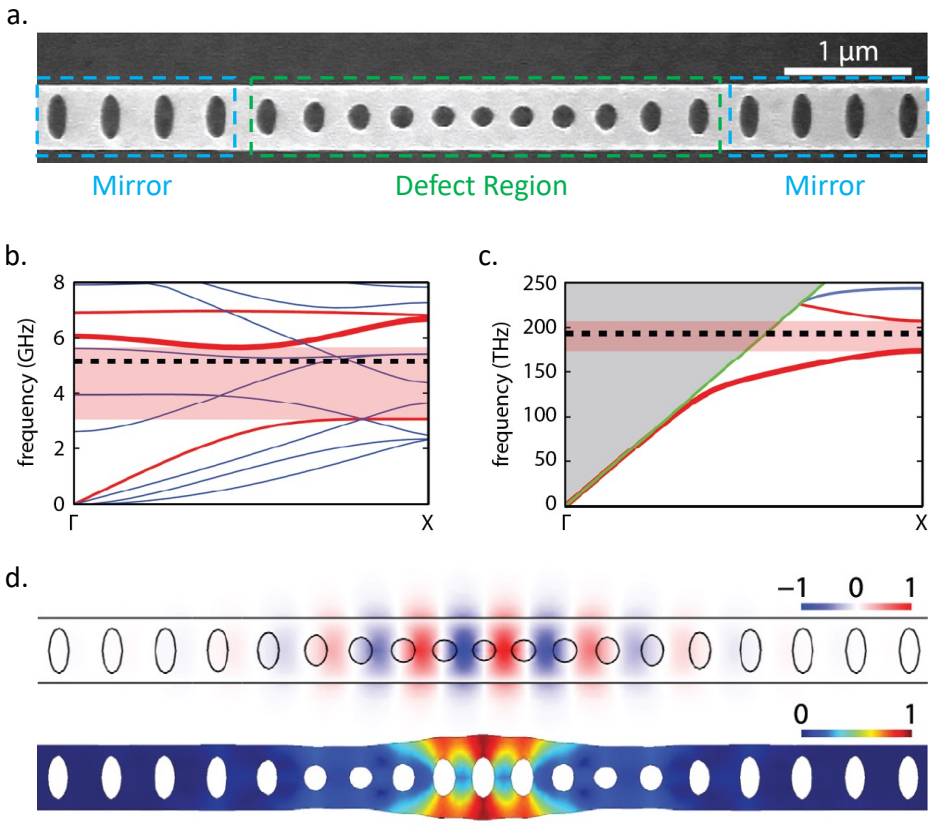

Figure 1.3: **1D optomechanical crystal. a.** Scanning electron microscope (SEM) image of a 1D optomechanical crystal cavity. **b.** mechanical and **c.** optical band structure for propagation along the x-axis in the nominal mirror unit cell, with quasi-bandgaps (red regions) and cavity mode frequencies (black dashed) indicated. In **b.**, modes that are y- and z-symmetric (red bands), and modes of other vector symmetries (blue bands) are indicated. In **c.**, the light line (green curve) divides the diagram into two regions: the gray shaded region above representing a continuum of radiation and leaky modes, and the white region below containing guided modes with y-symmetric (red bands) and y-antisymmetric (blue bands) vector symmetries. The bands from which the localized cavity modes are formed are shown as thicker curves. **d.** The normalized optical E_y field and the normalized mechanical displacement field **Q** of the localized optical and mechanical modes, respectively. Figure reproduced from [33]

as a photonic and phononic crystal and are designed to support a *simultaneous* optical bandgap centered around 194 THz and acoustic bandgap centered around 5GHz (Fig. 1.3 b,c). In the middle of the nano-beam, we have the 'defect region' where we break the translational symmetry of the mirror region by adiabatically tuning the dimensions of the holes. This 'defect region' supports both an optical mode at 194 THz inside the optical bandgap and an acoustic mode at 5 GHz inside the acoustic bandgap. Conceptually, by periodically patterning holes in the nano-beam,

we are modulating the effective refractive index thus creating a distributed Bragg mirror where we get constructive interference of multiple reflections which tightly confines the optical field to the defect region. Similarly, the array of holes is also periodically modulating the mass of the nano-beam giving us an effective 'acoustic Bragg mirror' which serves to tightly confine the acoustic field.

We can use finite element simulation methods to calculate the electric field profile $\mathbf{E}$ and the displacement profile $\mathbf{Q}$ of the 1D OMC. This allows us to calculate the single photon optomechanical coupling g_0 which has two contributions:

1. A moving boundary contribution ($g_{0,\mathrm{MB}}$) similar to the moving end mirror of a Fabry-Perot cavity which can be calculated as

$$g_{0,\mathrm{MB}} = -\frac{\omega_o}{2}\frac{\oint (\mathbf{Q}\cdot\hat{\mathbf{n}})(\Delta\epsilon\mathbf{E}_{\parallel}^2 - \Delta\epsilon^{-1}\mathbf{D}_{\perp}^2)dS}{\int \mathbf{D}\cdot\mathbf{E}}, \tag{1.13}$$

   where $\mathbf{Q}$ is the normalized displacement profile on the silicon surface, $\hat{\mathbf{n}}$ is the surface normal, $\mathbf{E}_{\parallel}$ is the electric field parallel to the surface, $\mathbf{D}_{\perp}$ is the electric displacement field perpendicular to the surface, $\Delta\epsilon = \epsilon_{\mathrm{Si}} - \epsilon_{\mathrm{Air}}$, and $\Delta\epsilon^{-1} = \epsilon_{\mathrm{Si}}^{-1} - \epsilon_{\mathrm{Air}}^{-1}$.

2. A photoelastic contribution ($g_{0,\mathrm{PE}}$), where the strain induced by the mechanical displacement causes a change in the refractive index. This contribution can be calculated as

$$g_{0,\mathrm{PE}} = \frac{\omega_o\epsilon_0 n^4}{2}\frac{\int_{\mathrm{Si}} \mathbf{E}^{\dagger}\cdot[\mathbf{pS}]\cdot\mathbf{E}\,dV}{\int \mathbf{D}\cdot\mathbf{E}\,dV}, \tag{1.14}$$

   where ω_o is the optical frequency, n is the refractive index, $\mathbf{E}$ is the electric field, $\mathbf{p}$ is the photoelastic tensor, and $\mathbf{S}$ is the strain tensor.

The total single photon optomechanical coupling rate is $g_0 = g_{0,\mathrm{MB}} + g_{0,\mathrm{PE}}$. The optical and mechanical mode shapes of a 1D OMC are plotted in Fig. 1.3 d. It is clear that both the optical and acoustic fields are co-localized and confined tightly to the defect region leading to a large overlap between these fields giving rise to a large single photon optomechanical coupling rate g_0. State of the art 1D OMC devices in silicon have been shown to achieve $g_0 \sim 1.1$MHz [33]. The carefully engineered acoustic and optical bandgaps surrounding our modes of interest help minimize radiation losses yielding high quality factors for the acoustic and optical

modes. The ease of fabrication and low material loss of silicon further helps to create modes with very low intrinsic loss. State of the art 1D OMC devices have demonstrated intrinsic optical linewidths $\kappa_{i,o} \sim 500$MHz and mechanical linewidths $\kappa_m \sim 4$kHz [43]. Large g_0 and small κ_o and κ_m are essential for maximizing the optomechanical cooperativity and hence the transduction efficiency as we will see in Chapter 2.

Chapter 2

WAVELENGTH-SCALE PIEZO-OPTOMECHANICAL TRANSDUCER

2.1 Introduction

A quantum transducer can be specified as a linear device with a certain conversion efficiency, added noise level, and repetition rate. Current approaches for microwave to optical quantum transduction rely on a strong optical pump to mediate the conversion process between single-photon-level signals at both frequencies. Increasing pump power allows for higher conversion efficiency, but due to parasitic effects of optical absorption in various components of the transducer and the vast difference in energy scales between optical and microwave frequencies, this often adds more noise to the conversion process. For applications in the quantum regime, the number of added noise photons per transduced photons should be less than 1. In several approaches, this trade-off between efficiency and noise has been a key obstacle to transduction of quantum signals [13, 21, 24, 25, 29, 30]. Recently a piezo-optomechanical approach has been used to demonstrate optical measurements of the quantum state of a superconducting transmon qubit with added noise levels below 1 photon [30]. In this thesis, we build on this piezo-optomechanical transduction approach with a design optimized for high efficiency and low noise. The goal of this design is to achieve performance improvements essential to detect quantum correlations in entabled microwave/optical photon pairs on reasonable timescales.

Fig. 2.1a illustrates the mode diagram of our transduction scheme. An intermediary mode $\hat{b}$ of a nanomechanical oscillator simultaneously couples to microwave photons from mode $\hat{c}$ of a microwave circuit, and to optical photons from mode $\hat{a}$ of an optical cavity. Microwave photons are converted to phonons via a resonant piezoelectric interaction, and these phonons are subsequently converted into optical photons via a parametric optomechanical interaction. The microwave photon-phonon conversion is realized by tuning the circuit frequency ω_c on resonance with the mechanical frequency ω_b. The phonon-optical photon conversion is realized by driving the optical cavity at frequency ω_d that is red-detuned by exactly the mechanical frequency s.t $\omega_d - \omega_a = -\omega_b$.

We realize the intermediary mechanical mode in the above schematic by connecting

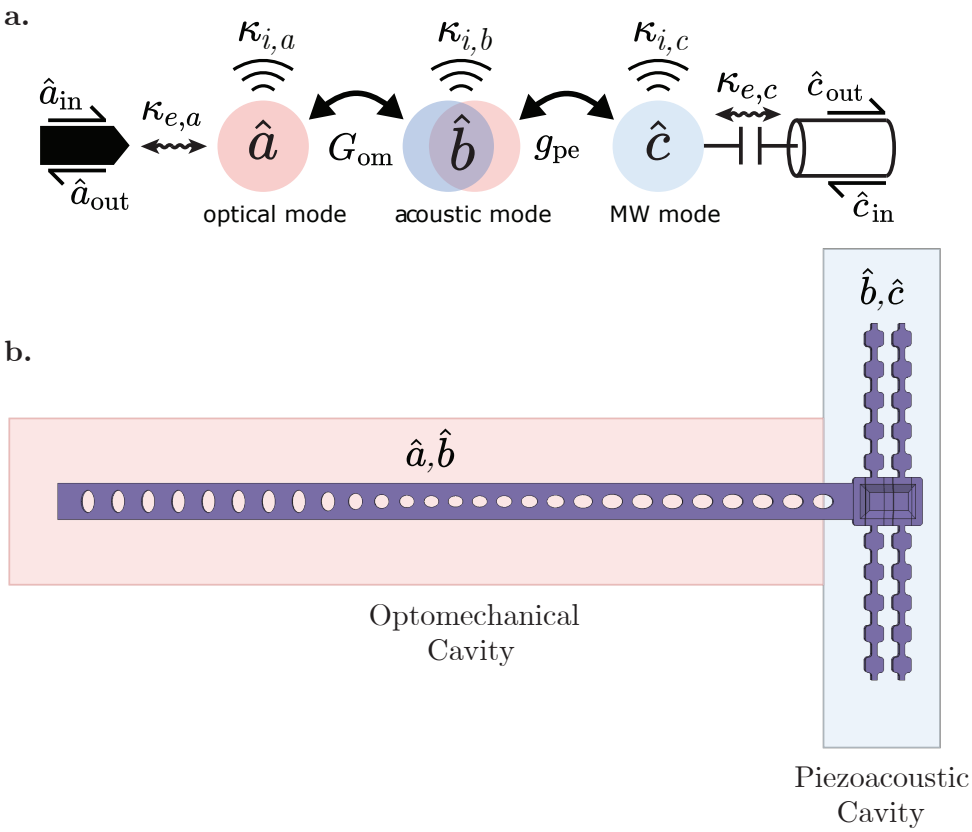

Figure 2.1: **Schematic of piezo-optomechanical transducer. a.** Mode schematic for piezo-optomechanical transduction. **b.** Device schematic for the transducer in this work. The device can be split into two regions, one which couples strongly to microwave electric fields and one which couples strongly to optical fields. Both are part of the same hybridized mechanical 'supermode' $\hat{b}_m$.

a wavelength-scale piezoacoustic cavity to an optomechanical crystal (OMC) cavity (see Fig. 2.1b). The acoustic modes of these components are strongly hybridized to form a mechanical 'supermode' whose mechanical displacement highly overlaps in one region with the field of a microwave circuit, and in another region with the field of an optical cavity. Using physically separate cavities allows us to independently optimize the piezoacoustic and optomechanical components of the transducer. Our design is formed from thin-film aluminum nitride (AlN) on the device layer of a silicon-on-insulator (SOI) substrate. We define the piezo-acoustic cavity in AlN, which has large piezoelectric coefficients. We define the OMC in silicon, since its large photoelastic coefficients [44] and refractive index [45] allow high optomechanical coupling. Well-established nanofabrication processes also allow high optical and mechanical quality factors for silicon OMCs [33, 43]. For the microwave circuit in this design, we develop a high impedance circuit with electrodes routed over the AlN region to allow for capacitive coupling to the piezoacoustic cavity.

Our design procedure begins with independently optimizing the piezoacoustic and OMC cavities for high g_{pe} and g_{om}, respectively. We design for closely matched acoustic modes at 5 GHz in both resonators, and for an optical mode at telecom wavelength (1550 nm). During the design process, it is crucial to maintain a low acoustic mode density such that the transduction schematic in Fig. 2.1 using a single acoustic mode remains valid. Further, since thin film AlN has higher microwave dielectric and acoustic loss than silicon, we aim to minimize the piezo volume in our device. The two independently optimized cavities are then physically connected, and the parameters of the resulting hybrid acoustic modes are analyzed. Using this approach, we design a transducer with expected conversion efficiency at the percent level while maintaining added noise photons <0.5.

2.2 Piezo Cavity Design

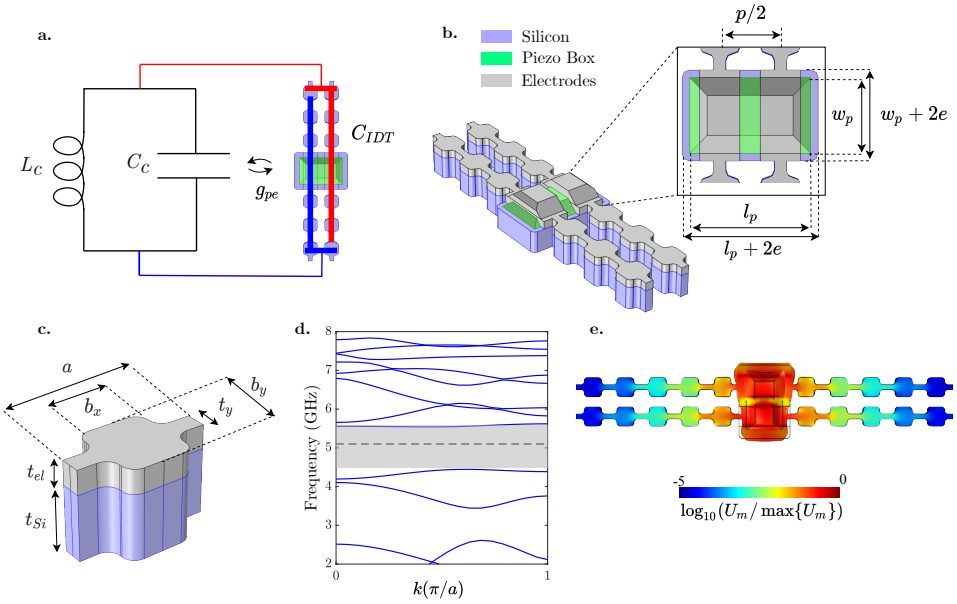

Figure 2.2: **Design of phononic shield. a.** Schematic illustrating the capacitive routing of the piezoacoustic cavity to a superconducting circuit. The circuit here can be replaced with any microwave resonator without loss of generality. **b.** Piezoacoustic cavity geometry, with relevant dimensions defined in blowout top view. **c.** Phononic shield unit cell, with relevant dimensions defined. **d.** Mechanical bandstructure of phononic shield unit cell in c), with (a, b_x, b_y, t_y) = (445, 225, 265, 70)nm. We observe a complete acoustic bandgap in excess of 1GHz around 5GHz. **e.** Log scale of mechanical energy U_m for piezoacoustic cavity mode at 5GHz, normalized to maximum value. We find >4 orders of magnitude suppression for 5 phononic shield periods.

The piezoacoustic cavity consists of a slab of aluminum nitride on top of a suspended silicon membrane patterned in the shape of a box. We work with 300nm thin-film c-axis aluminum nitride on top of a 220nm thick suspended silicon device layer. 100nm-thick Al electrodes run over the top of the slab and are routed in the form of

an interdigital transducer (IDT) which capacitively couples the cavity to a microwave circuit, as seen in Fig. 2.2a.

The box is surrounded by a periodically patterned phononic shield to mitigate acoustic radiation losses and to clamp the membrane to the surrounding substrate. The clamps are spaced periodically so that the IDT electrodes are routed over the top of each clamp, providing a means for electrical routing which is not acoustically lossy. The phononic shield uses an alternating block and tether pattern (see relevant dimensions in Fig. 2.2c) consisting of metal electrodes on top of a silicon base. By tuning the parameters a, b_x, b_y, and t_y, we achieve a >1GHz acoustic bandgap centered around 5GHz, the frequency of the mechanical mode of interest (Fig. 2.2d). This strongly suppresses clamping losses from the piezo region for sufficient number of shield periods, enabling high mechanical quality factors. By simulating the mechanical energy density across the entire cavity, we find that 5 shield periods provide >4 orders of magnitude suppression of acoustic radiation into the environment, as shown in Fig. 2.2e.

The dimensions of the piezo box (outlined in Fig. 2.2b) are designed to support a periodic mechanical mode whose periodicity matches that of the IDT fingers. This results in large overlap between the electric field from the IDT and the electric field induced by mechanical motion in the piezo box. This overlap gives a microwave photon-phonon piezoelectric coupling rate which is derived using first order perturbation theory:

$$g_{pe} = \frac{\omega_m}{4\sqrt{2U_m U_q}} \int_{\mathrm{LN}} \mathbf{D}_m \cdot \mathbf{E}_q \, dV. \tag{2.1}$$

Here the integral is taken over the entire AlN slab, $\mathbf{D}_m$ is the electric displacement field induced from mechanical motion in the piezo region, and $\mathbf{E}_q$ is the single-photon electric field generated by the microwave circuit across the IDT electrodes. The fields are normalized to their respective zero-point energies $\hbar\omega_m/2$, yielding the pre-factor in front of the integral in (1). U_m is the total cavity mechanical energy, and $U_c = \frac{1}{2}(C_c + C_{\mathrm{IDT}})V_0^2$ is the total IDT electrostatic energy. We note that the electrostatic energy is dependent on both the circuit capacitance C_c and IDT finger capacitance C_{IDT}, and therefore the coupling rate scales as $(C_c + C_{\mathrm{IDT}})^{-1/2}$. For our calculations in this work, we assume C_c = 7fF which is a typical value for a high impedance circuit [46]. C_{IDT} is calculated with finite-element electrostatic simulation and is typically on the order 0.1fF, a small contribution compared to circuit C_c.

The small value of C_{IDT} also minimizes the energy participation of the circuit electric field in the lossy piezo region, given by the ratio $\zeta_c = C_{\mathrm{IDT}}/C_c \sim 10^{-2}$. The contribution of AlN to the circuit loss rate $\kappa_{q,i}$ is then estimated as $\zeta_q \kappa_{q,\mathrm{AlN}}$. Using reported dielectric loss tangents in AlN $\tan\delta = 7 \times 10^{-3}$ [47] giving $\kappa_{q,\mathrm{AlN}}/2\pi = 25\mathrm{MHz}$, we estimate the AlN contribution to circuit loss to be $\zeta_q \kappa_{q,\mathrm{AlN}}/2\pi \sim 20\mathrm{kHz}$. This contribution is ~5x smaller than typical loss rates $\kappa_{q,\mathrm{SOI}}/2\pi \sim 500\mathrm{kHz}$ measured in high impedance circuits fabricated on SOI. As a result, the contribution of the piezo cavity to circuit loss is not a limiting factor, and justifies the on-chip coupling scheme outlined in Fig. 2.2a.

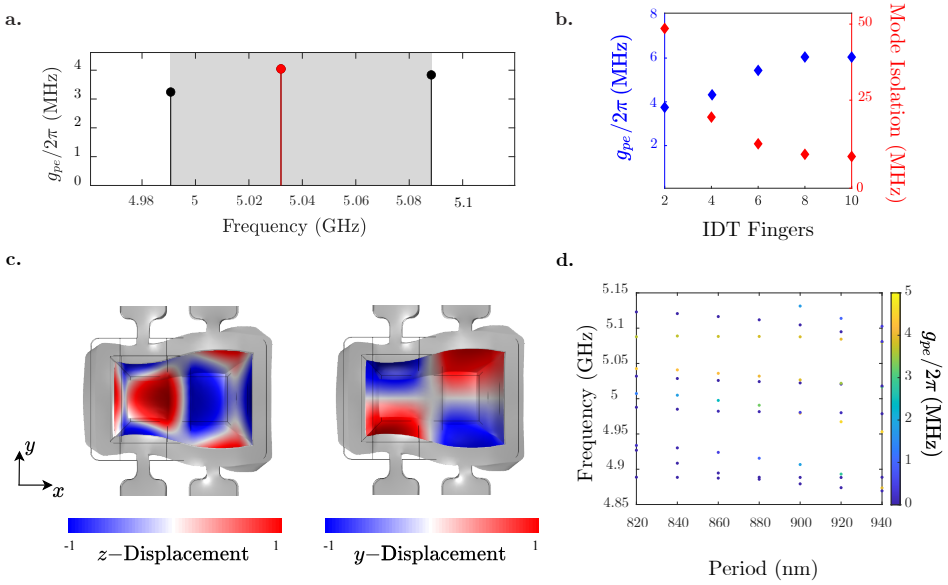

Figure 2.3: **Design of piezoacoustic cavity. a.** Mode structure for optimized piezoacoustic cavity design with $(p, w_p, e) = (783, 423, 118)$ nm. Mode of interest (red) achieves $g_{pe}/2\pi$ of 4MHz. Shaded grey region indicates the mode isolation window with the nearest mode >40MHz away. **b.** $g_{pe}/2\pi$ and mode isolation for optimized designs with differing number of IDT fingers. We observe g_{pe} saturating beyond $N = 4$ fingers, and mode isolation decreasing with increasing number of fingers. **c.** Mechanical mode shape of red mode in (a). Right shows the in-plane (breathing) and left shows the out-of-plane (Lamb-wave) components of the optimized mechanical mode. **d.** Mode structure and piezoelectric coupling vs. IDT period, with data points colored according to g_{pe}.

An important design consideration with this type of piezoacoustic cavity is the number of IDT fingers used. For N IDT fingers, the length l_p of the piezo region is given by $l_p = Np/2$, where p is the IDT period. As the number of fingers increases, the increased size of the piezo box results in a more crowded mode structure (Fig. 2.3b), and it is more difficult to isolate a single mechanical mode without coupling to parasitic modes in the vicinity of the mode of interest. This is important as these parasitic modes may not possess optimal symmetry and will not hybridize well with the OMC cavity, reducing overall transduction efficiency.

Reducing the size of the piezo region is also important to reduce microwave photon and phonon decoherence as AlN has high microwave dielectric and acoustic loss tangents compared to silicon (further discussion in Sec. 2.4). For these reasons, we choose a 2-finger design to minimize these effects. We emphasize the small dimensions of the piezoacoustic cavity in this design in contrast with previous work on piezo-optomechanical quantum transducers [48]. The benefits of this approach come at the cost of higher sensitivity of the piezo modes to changes in cavity dimensions. This can have large effects on hybridization with the OMC cavity and the performance of the final transducer device, which relies on resonant matching of acoustic modes in both regions. We show further in Sec. 2.4 that the achievable hybridization between piezo and OMC modes with this small piezo volume approach is large enough to protect the design against typical fabrication disorder.

The mechanical mode of interest is periodic with out-of-plane (Lamb-wave) and in-plane breathing components. The Lamb-wave component of the mode induces an electric field in the piezo region with high overlap with the IDT electric field, while the breathing component of the mode enables hybridization with the breathing mode of the optomechanical crystal to be attached in the full device (see Fig. 2.3c). The piezo mode can be tuned with three parameters p, w_p, and e. p is the periodicity of the IDT fingers and is used to parameterize the piezo box length, given by $l_p = Np/2$ as described earlier. p is used to tune the frequency of the mode of interest (Fig. 2.3d) while maintaining appropriate phase-matching of the mode periodicity with the IDT fingers. w_p is the piezo box width, which can be increased to increase g_{pe} via larger mode volumes or decreased to reduce the mode crowding that results from larger box size. Finally, we define a silicon-piezo buffer parameter e, which extends the supporting silicon box length/width by an amount e compared to the piezo box. This buffer is needed to protect against silicon/piezo box misalignment in the fabrication process, and acts as an added degree of freedom for tuning frequency, g_{pe}, and mode isolation. We use numerical optimization to tune parameters (p, w_p, e) to arrive at a design with high piezoelectric coupling and mode isolation. We employ a Nelder-Mead simplex optimization [49, 50] similar to that described in [33]. After optimization, we obtain a single mechanical mode with $g_{pe}/2\pi$ = 4MHz, which is isolated by >40MHz from other mechanical modes (Fig. 2.3a). We will use this single mode to strongly couple to the modes of an optomechanical crystal cavity to create the mechanical supermode of Fig. 2.1a.

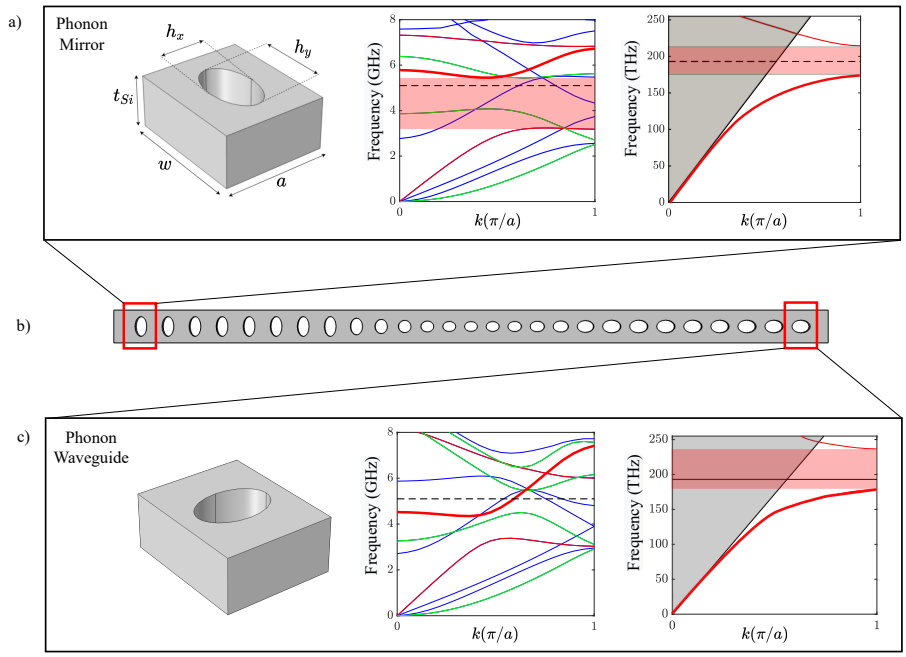

Figure 2.4: **Design of the optomechanical cavity. a.** Unit cell geometry, mechanical, and optical bandstructure of phonon mirror region with (a, w, h_x, h_y) = (436, 529, 189, 320)nm. Mechanical bands are color-coded by symmetry, with red (green) corresponding to breathing (Lamb-wave) mode symmetry classes. Blue bands represent all other symmetries. Mechanical bandgap for breathing modes and optical bandgap are both highlighted in red. **b.** Full OMC geometry, with phonon mirror and phonon waveguide unit cells highlighted. **c.** Unit cell geometry, mechanical, and optical bandstructure of phonon waveguide region with (a, w, h_x, h_y) = (436, 529, 295, 205)nm. Mechanical bands color-coded as in (a). Breathing mode crosses 5.1GHz resulting in waveguide-like behavior at the mechanical frequency. The optical bandgap is maintained.

2.3 Optomechanics Design

The optomechanical crystal cavity is designed in a similar fashion to previous work [33], with the crucial change of a modified unit cell design on one side of the cavity to enable strong mechanical hybridization with the piezo cavity. This separates the OMC into three distinct regions: a phonon mirror, defect region, and phonon waveguide (see Fig. 2.4 for details). The phonon mirror unit cell (Fig. 2.4a) is designed to have a simultaneous mechanical and optical bandgap for modes of certain symmetry classes. In the defect region, the phonon mirror unit cell transitions to a defect cell designed to co-localize a 5.1GHz mechanical breathing mode and a 194THz (λ_0 = 1550nm) optical mode. The phonon waveguide unit cell (Fig. 2.4c) is mechanically transparent to breathing mode phonons at 5.1GHz, while maintaining a large bandgap for optical modes. This is achieved by modifying the ellipticity of the phonon mirror unit cell. We see in Fig. 2.4b that the resulting mechanical mode is permitted to leak out into the phonon waveguide region, while the optical mode remains highly localized within the defect region.

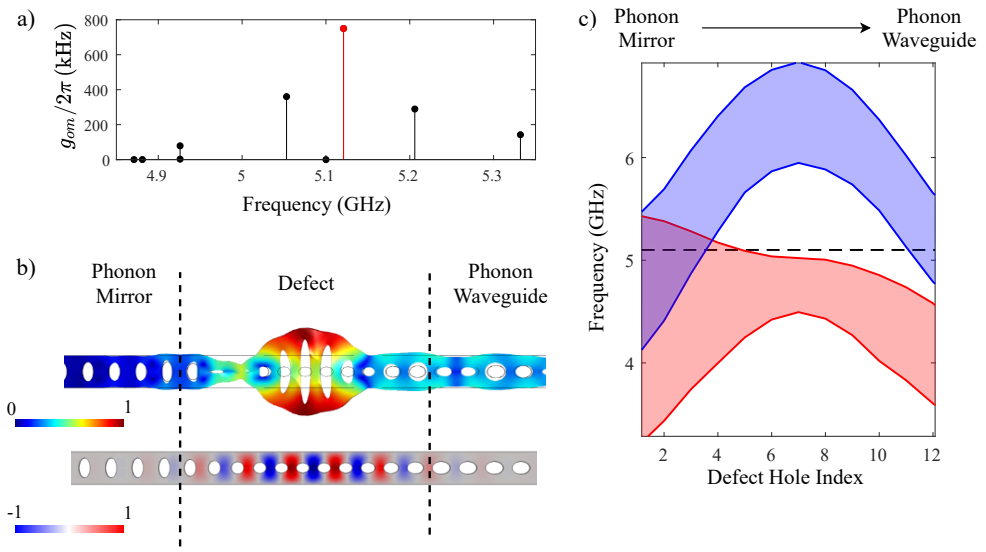

Figure 2.5: **Optomechanical cavity mode structure. a.** Resultant mode structure of optimized OMC design. Highest g_{om} mode (highlighted in red) gives 750kHz optomechanical coupling. **b.** OMC mechanical and optical mode shapes, along with unit cell length at each hole in the defect region. Phonon mirror, phonon waveguide, and defect region are labeled and outlined. **c.** Bandgap of different symmetries as a function of hole index along the defect region. Red shaded region represents the bandgap for breathing mode symmetries, and blue shaded region represents the bandgap for Lamb-wave mode symmetries.

The optomechanical coupling rate is calculated from the optical frequency shift arising due to the photoelastic effect [51] and moving dielectric boundaries [52], giving $g_{om} = g_{om,\mathrm{PE}} + g_{om,\mathrm{MB}}$. For a detailed derivation of both contributions to g_{om}, see [53]. The photoelastic contribution is derived from 1st order perturbation theory as

$$g_{om,\mathrm{PE}} = \frac{\omega_o \epsilon_0 n^4}{2} \frac{\int_{\mathrm{Si}} \mathbf{E}^\dagger \cdot [\mathbf{pS}] \cdot \mathbf{E}\, dV}{\int \mathbf{D} \cdot \mathbf{E}\, dV}, \tag{2.2}$$

where ω_o is the optical frequency, n is the refractive index, $\mathbf{E}$ is the electric field, $\mathbf{p}$ is the photoelastic tensor, and $\mathbf{S}$ is the strain tensor.

The moving boundaries component is derived similarly as

$$g_{om,\mathrm{MB}} = -\frac{\omega_o}{2} \frac{\oint (\mathbf{Q} \cdot \hat{\mathbf{n}})(\Delta\epsilon \mathbf{E}_\parallel^2 - \Delta\epsilon^{-1} \mathbf{D}_\perp^2) dS}{\int \mathbf{D} \cdot \mathbf{E}\, dV}, \tag{2.3}$$

where $\mathbf{Q}$ is the normalized mechanical displacement field, $\hat{\mathbf{n}}$ is the surface normal, $\mathbf{E}_\parallel$ is the electric field parallel to the surface, $\mathbf{D}_\perp$ is the electric displacement field perpendicular to the surface, $\Delta\epsilon = \epsilon_{\mathrm{Si}} - \epsilon_{\mathrm{Air}}$, and $\Delta\epsilon^{-1} = \epsilon_{\mathrm{Si}}^{-1} - \epsilon_{\mathrm{Air}}^{-1}$.

One may expect the coupling rates in this design to suffer due to the delocalization of the mechanical mode. However, we find that after a Nelder-Mead simplex

optimization of various OMC dimensions similar to [33], the resulting design gives multiple modes with high values of $g_{om}/2\pi$, with the maximum coupling rate exceeding 750kHz (Fig. 2.5a). This is comparable to state-of-the-art OMC designs in silicon which achieve $g_{om}/2\pi$ up to ~1MHz [43].

The radiation-limited optical quality factor Q_o can be simulated and is found to be in excess of 10^6, corresponding to an intrinsic optical loss rate $\kappa_{o,i}/2\pi \sim 200$MHz. However, Q_o is usually practically limited to ~ 500,000 ($\kappa_{o,i}/2\pi \sim 400$MHz) [43] due to optical scattering from surface defects introduced in the fabrication process. To ensure this limit is reached, we configure the optimization such that g_{om} is maximized while maintaining Q_o above ~ 10^6, well above the realistic Q_o limit.

The total optical loss rate is given by $\kappa_o = \kappa_{o,i} + \kappa_{o,e}$, where $\kappa_{o,e}$ is the decay rate associated with input coupling. $\kappa_{o,e}$ is controlled with a coupling waveguide and is typically designed so that $\kappa_{o,e} = \kappa_{o,i}$. The total optical loss rate is then $\kappa_o \approx 2\kappa_{o,i}/2\pi = 800$MHz.

When hybridizing the modes of the piezoacoustic and OMC cavities, we must consider the relative motional symmetry of the two cavity modes. Our OMC design contains only breathing motion, whereas the piezo cavity design contains both breathing and Lamb-wave components. If the OMC bandstructure permits propagation of 5GHz phonons with Lamb-wave symmetry, then the OMC breathing mode will hybridize with leaky, delocalized modes of Lamb-wave symmetry. This can reduce optomechanical coupling and contribute significantly to mechanical losses in the device. For this reason, the phonon mirror and waveguide dimensions are chosen such that their bandstructure exhibits a bandgap for modes of Lamb-wave-like symmetries. This is seen in the mechanics band diagrams of Fig. 2.4, where we see a bandgap for Lamb-wave-like modes (colored in green) in both the phonon mirror and waveguide region.

Fig. 2.5c further illustrates this idea by showing the mechanical bandgap of unit cells across the defect region for both breathing and Lamb-wave-like modes, shaded in red and blue, respectively. At the phonon waveguide side, the breathing mode bandgap falls below 5GHz, permitting the breathing motion of the piezo mode to couple strongly to the defect region. However, 5GHz lies inside the Lamb-wave bandgap, so that Lamb-wave motion from the piezo cavity decays in the phonon waveguide and does not interact with the defect region.

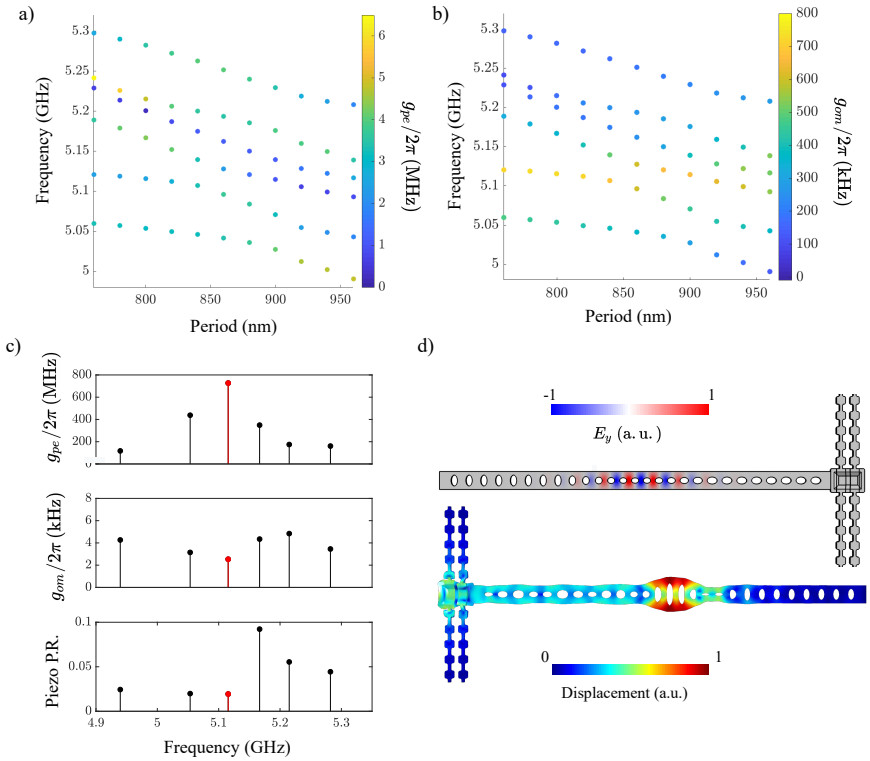

Figure 2.6: **Full piezo-optomechnaical transducer design. a.** Full transducer piezoelectric coupling and mode structure vs. IDT period. Shown are all modes which have either high piezoelectric or high optomechanical coupling. Data points are colored according to g_{pe} value. **b.** Full transducer optomechanical coupling and mode structure vs. IDT period. Shown are the same modes as in (a), only colored according to optomechanical coupling. **c.** Mode structure at various periods, showing g_{pe}, g_{om}, and energy participation ratio in the piezoelectric region. **d.** Mechanical mode profile of the 880nm mode.

2.4 Full Device Design

After independently designing the piezoacoustic and optomechanical cavities, we connect the two as shown in Fig. 2.6d and simulate the resulting hybridized mode structure. To observe the hybridization of the piezo and optomechanical modes, we sweep the IDT period in the piezo region to tune the piezo mode through the multiple optomechanical resonances. We find that over a frequency window >250MHz, there is a large number of mechanical modes with simultaneous high piezoelectric and optomechanical coupling rates. The phonon waveguide allows for strong enough mode hybridization that the piezoelectric coupling is distributed across a large number of modes. As shown in Fig. 2.6c, the mechanical energy participation in the piezo region ζ_m is in the range 1-10%. We find that across the entire hybridization window, at least one mode can be identified with $g_{om}/2\pi > 500$kHz, $g_{pe}/2\pi > 1$MHz, and $\zeta_m < 5\%$. In Fig. 2.6c, this mode is highlighted in red

with $g_{om}/2\pi = 725\text{kHz}$, $g_{pe}/2\pi = 2.5\text{MHz}$, and $\zeta_m < 2\%$. We will use the values from this mode to quantify further calculations in this work. In practice, the frequencies and couplings of these mechanical modes are subject to change due to multiple sources of fabrication disorder. The multi-mode structure and relatively large hybridization ensure that the full device is robust to these shifts. While the exact frequencies and couplings may shift, Fig. 2.6a and 2.6b illustrate that the qualitative nature of the mode structure remains unchanged for a large range of frequency shifts. Additionally, the modes are separated far enough in frequency that their parasitic effect on each other's transduction efficiencies is minimal.

We may use the simulated piezo participation ratio and radiation loss to estimate the mechanical decoherence rate κ_m of our device. There are two dominant contributions to decoherence in our design. The first is acoustic radiation loss into the surrounding substrate. This can be simulated and is found to be in the range $\kappa_{\text{rad}}/2\pi \sim 1-10\text{kHz}$ for all modes in Fig. 2.6, with $\kappa_{\text{rad}}/2\pi = 2.3\text{kHz}$ for the mode highlighted in Fig. 2.6c. The second is coupling to two-level systems (TLS), which in both lithium niobate [54] and silicon [43] has been shown to be the dominant decoherence mechanism for GHz-frequency acoustic cavities at single phonon level powers and milliKelvin temperatures. For mechanical piezo participation ratio ζ_m, the TLS induced decoherence rate can be estimated by $\kappa_{\text{TLS}} = \zeta_m \kappa_{\text{LN}} + (1-\zeta_m)\kappa_{\text{Si}}$. Using reported TLS-limited linewidths $\kappa_{\text{LN}}/2\pi \sim 100-300\text{kHz}$ in lithium niobate [26, 54] and $\kappa_{\text{Si}}/2\pi \sim 5\text{kHz}$ in silicon [43], and taking $\zeta_m = 2\%$, we estimate a TLS induced decoherence rate of $\kappa_{\text{TLS}}/2\pi \sim 10$ kHz. The total mechanical decoherence rate is then estimated to be in the range $\kappa_m/2\pi \sim 10-20\text{kHz}$.

2.5 Efficiency and Added Noise

To analyze the efficiency and noise of our design, we consider a pulsed scheme for microwave to optical state transfer on a transmon qubit connected to the transducer [30]. The qubit is first tuned on resonance with the mechanical mode for a time $t = \pi/g_{pe}$ to complete a microwave photon-phonon swap operation, and subsequently detuned far off-resonance. A red-detuned ($\omega_d - \omega_o = -\omega_m$) laser pulse is then used to upconvert this phonon into an optical photon. The intrinsic efficiency of such a pulsed scheme is simply given by $\eta_i = \eta_{pe}\eta_{om}$, where η_{pe} is the piezoelectric photon-phonon swap efficiency, η_{om} is the optomechanical phonon-photon conversion efficiency.

η_{pe} can be calculated from a master equation simulation of the qubit-mechanics

system. Using $g_{pe}/2\pi$ = 2.5MHz, estimated $\kappa_q/2\pi$ = 60kHz from Section 2.2, estimated mechanics decoherence rate $\kappa_m/2\pi$ = 20kHz from Section 2.4, we find η_{pe} = 0.95. The optomechanical readout step determines both η_{om} and the dominant noise contribution to the transducer, which arises from optical absorption heating of the mechanical mode. For a laser pulse duration τ, η_{om} is given by [30]

$$\eta_{\mathrm{om}}(\tau) = \frac{\gamma_{om}}{\gamma_{om} + \kappa_m}(1 - e^{-(\gamma_{om}+\kappa_m)\tau}), \tag{2.4}$$

where $\gamma_{om} = 4g_{om}^2 n_o/\kappa_o$ is the optomechanical scattering rate, and n_o is the number of intracavity optical photons corresponding to peak power of the optical pulse. In principle, this efficiency may be unity in the limit $\tau \gg 1/(\gamma_{om} + \kappa_m)$ and $\gamma_{om} \gg \kappa_m$. However, optically-induced heating of the mechanical mode severely limits τ in order to maintain <1 added noise photon. This leads to a fundamental tradeoff between efficiency and added noise resulting from heating dynamics in optomechanical systems. Maximizing efficiency for a given level of added noise requires careful choice of pulse duration τ and optical power n_o.

The added noise phonons $n_m(\tau)$ during optical readout are thought to originate from optical excitation of material defect states which undergo phonon-assisted relaxation via the mechanical mode of interest [35, 55, 56]. The timescale τ_h for n_m to exceed 1 noise phonon depends strongly on n_o and is found to vary greatly in different devices. Experiments in low-loss ($\kappa_m \lesssim$ 10kHz) pure silicon OMC devices report $\tau_h \sim 1\mu$s [37, 43], whereas silicon OMCs integrated in a piezo-optomechanical transducer with κ_m = 1MHz report much shorter $\tau_h \sim$ 100ns [30]. This suggests the presence of additional sources of optically induced heating and mechanical damping in piezo-optomechanical transducers that are potentially correlated. Possible sources are optical absorption by the IDT electrodes, TLS-limited loss in the piezo region, and surface defects in the OMC region from additional steps in the transducer fabrication process. While the dynamics of optically induced heating in piezo-optomechanical devices is a subject of future studies, it is clear that a transducer design aimed at improving optomechanical readout efficiency and noise should make the acoustic mode involved in the transduction process as silicon-like as possible.

In the design presented above, we minimize the dimensions of the piezo cavity so that most of the energy in the mechanical mode lives in the OMC region. The estimated mechanical damping rates based on participation ratios of various regions and calculated optomechanical coupling rates are comparable to those realized in pure

silicon OMCs. Therefore, we may approximate the heating dynamics of our design as similar to that reported in previous silicon OMC work [37]. Using this heating model, we estimate ~0.5 added noise photons for a pulse with $n_o = 45$ and $\tau = 500$ns. Using the previously estimated values $\kappa_m/2\pi = 10$kHz, $\kappa_o/2\pi = 800$MHz, and $g_{om}/2\pi = 725$kHz (s.t. $\gamma_{om}/2\pi = 120$kHz), we estimate a pulse with $n_o = 45$ and $\tau = 500$ns can achieve $\eta_{om} \sim 30\%$. Combined with $\eta_{pe} = 0.95$, we achieve an estimated intrinsic efficiency $\eta_i \sim 29\%$.

There are additional noise sources which we have not considered here such as photodetector dark counts and residual photons from the optical pump pulse. However, given the measured photon count rates for these noise sources in previous milliKelvin optomechanics experiments in our group, these noise sources are negligible compared to those from optical absorption heating discussed above.

The total efficiency of our device is given by $\eta = \eta_i \eta_k \eta_{ext}$, where $\eta_k = (\kappa_{o,e}/\kappa_o)$ determines the fraction of optical photons emitted into the coupling waveguide, and η_{ext} is the external photon collection efficiency. For $\kappa_{o,e} \approx \kappa_{o,i}$ (critical coupling) we have $(\kappa_{o,e}/\kappa_o) \approx 0.5$. In typical optomechanics experiments, η_{ext} is mainly determined by the fiber-to-device coupling efficiency, insertion loss of the optical pump filtering setup, and quantum efficiency of single photon detectors. In our typical experimental setup we estimate these factors are 0.6, 0.2, and 0.9, respectively and lead to $\eta_{ext} \sim 0.1$. The product of all three efficiency estimates above yields a total transducer efficiency $\eta \sim 1.5$ %.

Finally, we consider the expected repetition rate for the transduction sequence in the pulsed scheme described above. In previous work, this was limited to 100Hz by the ~10-ms timescale for quasiparticle (QP) relaxation in the aluminum transmon coupled to the transducer [30]. We expect that using niobium nitired with QP relaxation timescale in the ~ns range [57, 58] will allow for repetition rates in the 10 kHz range (more on this in Chapter 4). At this repetition rate and estimated total efficiency η ~1.5%, we expect a single photon count rate of ~ 150Hz and a photon coincidence rate of order 1Hz. The latter, which is the key figure of merit for second order intensity correlation measurements as well as heralded remote entanglement generation, indicates reasonable measurement times in the range of an hour for these experiments.

2.6 Conclusion

We have presented an optimized design for a wavelength scale piezo-optomechanical transducer suitable for off-chip coupling to a transmon qubit. We have independently simulated and optimized the design of a piezoacoustic cavity and an optomechanical crystal cavity then hybridized their acoustic mode structure in a way which is highly robust to fabrication disorder. We emphasize that our choice of material platform and minimized piezoacoustic cavity dimensions allows us to design for high piezoelectric swap efficiency without significantly compromising on-chip superconducting circuit Q-factor, and with optomechanical readout efficiencies comparable to state-of-the-art 1D OMC devices. With the expected performance from this transducer design, experiments measuring quantum correlations in photons generated by the transducer as well as a demonstration of heralded remote entanglement between two transducer devices should be feasible on reasonable measurement timescales. Finally, we note that the efficiency, noise, and repetition rate of the above transducer design are expected to be limited by optomechanical heating rates. Future design improvements can be made by employing 2D optomechanical crystal cavities, which through better thermal conductivity to the substrate, have achieved higher optomechanical co-operativities with lower added noise [59].

Chapter 3

DESIGN OF LIGHT-ROBUST NBN CIRCUITS

In Chapter 2, we discussed the design of our piezo-optomechanical transducer and the expected conversion efficiency and added noise of our device. Another important figure of merit of the transducer is its repetition rate. Since our transducer operates in pulsed mode (ultimately limited by OMC heating), the repetition rate is simply the rate at which we can repeat the transduction pulse sequence. A representative transduction pulse sequence is shown in Fig. 3.1a. It begins with a microwave pulse to excite the on-chip superconducting circuit. Next the microwave excitation in the circuit is exchanged for a phonon in the mechanical mode. Next a red-detuned optical pump pulse converts the phonon into and optical photon which is subsequently detected on a photodetector. This optical pulse consists of $\sim$ 200THz frequency optical photons which have energy larger than the superconducting gap of typical superconducting materials. Since our superconducting circuit is in close proximity to our piezo-optomechaical transducer, absorption of these highly energetic optical photons can break Cooper pairs in the superconductor creating excess quasiparticles (QPs). Theses excess QPs creates loss in the circuit [60] leading to a transducer dead time until the excess QPs relax. This quasiparticle relaxation time in general is a material and substrate dependent property. For the all-aluminum (Al) qubits on a silicon-on-insulator substrate used in the transducer device demonstrated in [30], the circuit recovery time after the optical generation of quasiparticles was on the order of $\sim$10ms (see Fig. 3.1)b. Other measurements of quasiparticle relaxation in Al based superconducting circuits have also indicated relaxation times on the order of $\sim$ ms [61, 62]. Niobium nitride (NbN) is a superconducting material with much shorter measured quasiparticle relaxation times ($\sim$ns) [63]. In this chapter, we focus on the design of NbN-based superconducting circuits. Rapid recovery following illumination, tunability and high impedance are the key aspects which enable the measurements shown later in this thesis and will be discussed in detail in this chapter. At the end of this chapter we will consider two possible designs for achieving a light-robust tunable circuit.

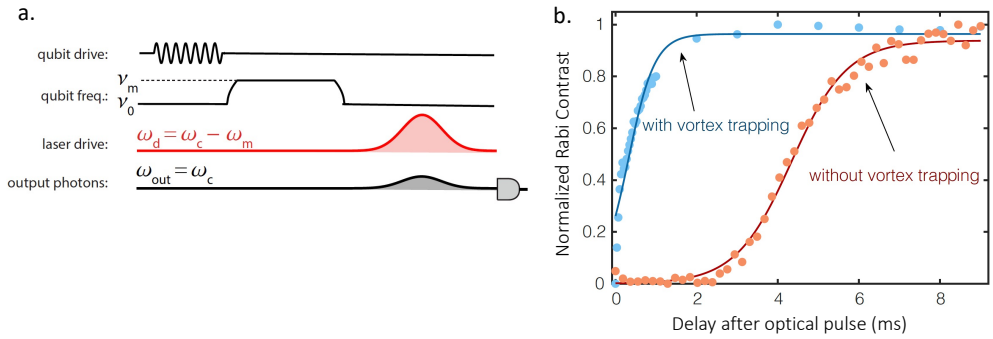

Figure 3.1: **Pulse sequence and laser induced quasiparticle recovery for a quantum transducer device. a.** Pulse sequence and **b.** Laser induced quasiparticle recovery for a quantum transducer device. Figure reprinted by permission from Springer Nature Customer Service Center GmbH: Springer Nature, *Nature*, Ref. [30], ©2020

.

3.1 Quasiparticle Dynamics

When a superconductor is subjected to a ilumination by above-bandgap electromagnetic radiation, excess quasiparticles (QPs) are created. Relaxation QPs is a process where the excess population recombines to form Cooper pairs with the emission of a phonons or via an electron-phonon scattering processes [64]. Depending on the material properties of the chosen superconductor, characteristic timescale of relaxation varies from milliseconds to nanoseconds. In contrast to the illumination of a superconducting aluminum, fast QP relaxation superconductors (like NbN) respond to pair-breaking illumination less dramatically. Because of faster relaxation rate the average QP density is also expected to be significantly lower with equivalent illumination power. In addition to extra loss, excess QP population in superconductors is expected to modify the surface impedance of the superconductor according to: $\delta Z_s = \delta n_{qp} \partial Z_s / \partial \delta n_{qp}$ where the derivative depends on ω, T, and material parameters, and may be calculated using the Mattis–Bardeen theory [65]. In the case of a resonator, this change in impedance will shift the resonance frequency according to the excited QP population. Optical illumination is not the only method of exciting QPs in a superconductor, we can also modify QP population thermally and electrically. However, at temperatures below the superconducting transition temperature QPs are exponentially suppressed.

3.2 Kinetic Inductance

In a normal conductor, the inductance arises primarily from the magnetic field generated by the moving electrons. However, in a superconductor, the flow of electric current is carried by the coherent motion of Cooper pairs, and the behavior

of this current is quite different. When an electric current flows through it, the Cooper pairs move without scattering or dissipating energy due to the absence of electrical resistance. As a result, the Cooper pairs have a finite mass and momentum associated with their motion. When an external magnetic field is applied to the superconductor, it induces a change in the momentum of the Cooper pairs. This change in momentum causes the Cooper pairs to experience an effective inertia, which is similar to the concept of mass in classical mechanics. This effective inertia gives rise to an inductance, known as the kinetic inductance, in addition to the geometric inductance that all conductors possess.

The kinetic inductance is proportional to the square of the resistance-free current flowing through the superconductor and inversely proportional to the critical current, which is the maximum current a superconductor can carry before it transitions into a normal conducting state. The kinetic inductance also depends on the dimensions and shape of the superconductor. We can derive these properties from BCS theory in the low frequency limit ($\hbar\omega \ll 2\Delta$), where $\sigma_2/\sigma_n = \frac{\pi\Delta}{\hbar\omega}\tanh(\frac{\Delta}{2kT})$ which in the case of $T \ll T_c$ we can simplify to $L_k = \frac{l}{w}\frac{\hbar R_{sq}}{\pi\Delta}$, where l and w refer to the geometry of the superconductor, R_{sq} is the normal sheet resistance and $\Delta \approx 1.76kT_c$ [66]. Kinetic inductance has a nonlinear response to current which can by $L_k(I) \approx L_k(0)[1 + I^2/{I_*}^2]$, where I_* is on the order of the critical current.

3.3 Galvanic DC Injection Design

Our transducer design relies on resonant piezo-electric interaction to achieve maximal coupling. The fabrication-induced frequency disorder of both the piezo and electrical resonators makes frequency alignment practically challenging. This problem is addressed in our design by adding a frequency tunable component. The nonlinearity of kinetic inductance allows for in situ tuning of the resonator via injection of direct current (DC). The path of injection has two primary approaches: galvanic and inductive. To achieve high Q-factor devices we would like to sufficiently isolate our microwave circuits from the rest of the measurement apparatus. When considering this design we would like to maintain high quality factor while allowing for a galvanic path for DC injection. With this consideration in mind our galvanic DC injection design utilizes RF chokes to feed DC to the kinetic inductance circuit while maintaining RF isolation similar to the design shown in [67]. The Q-factor of the circuit is determined by the values of L_c, C_c in Fig. 3.2. In our experiments we found this design difficult to work with with large disrder causing a wide spread of both frequency and Q-factor.

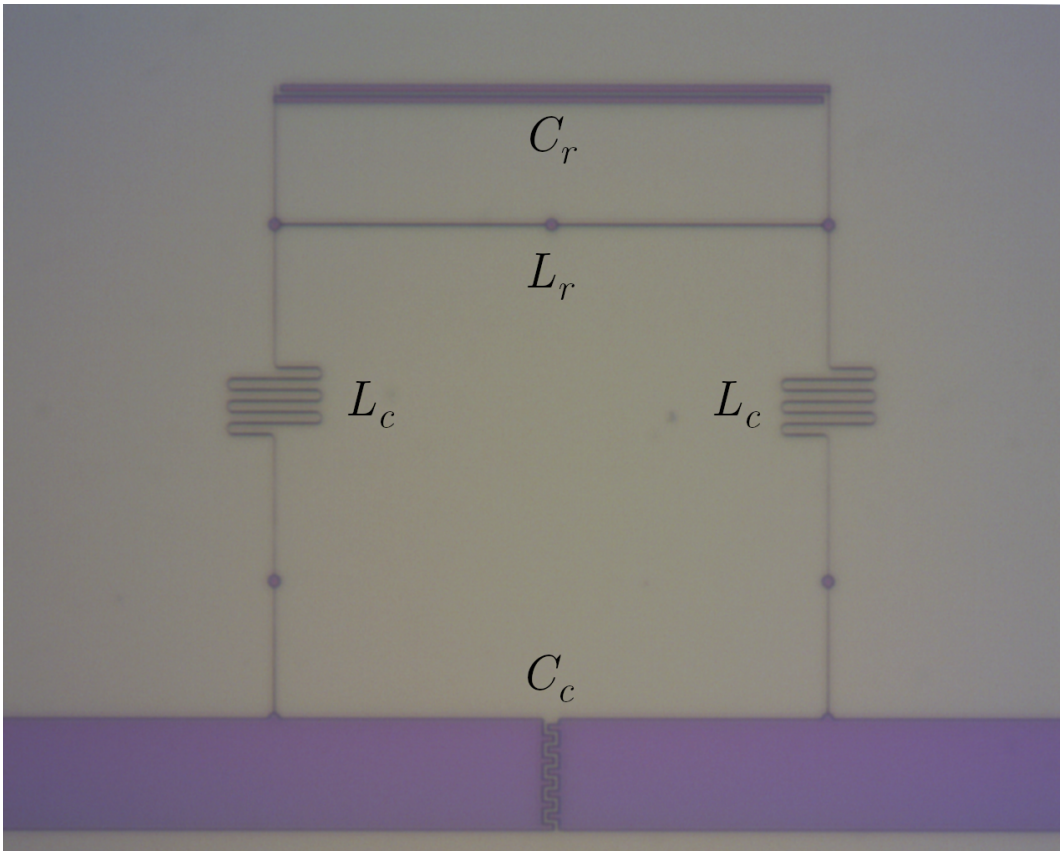

Figure 3.2: **Optical image of galvanic tunable resonator. a.** Optical image of a fabricated galvanic tunable resonator on silicon consisting of C_r, L_r referring to explicit resonator values primarily setting the frequency whereas L_c, C_c set the waveguide coupling rate. Purple areas are superconductor. Grey areas are silicon.

3.4 Wireless DC Injection Design

As the name implies this design relies on wireless inductive paths to inject DC. In this case our circuit design incorporates a closed loop similar to designs developed in [68]. When a magnetic field is applied perpendicular to the loop a proportional supercurrent will be induced in the closed loop demonstrate in Fig. 3.3. This design simplifies the circuit layout and results in higher Q-factor, however the loop structure will also result in a larger circuit footprint. An optical image of our niobium nitride (NbN) circuit on a silicon substrate is depicted in Fig. 3.4.

3.5 Electromagnetic Simulations

Our circuit designs are fine tuned in finite element method software to refine with frequency, waveguide coupling and approximate the design impedance. We use Sonnet for our designs which easily handles high kinetic inductance materials with an option to include a value for sheet inductance. In addition to the single-resonator

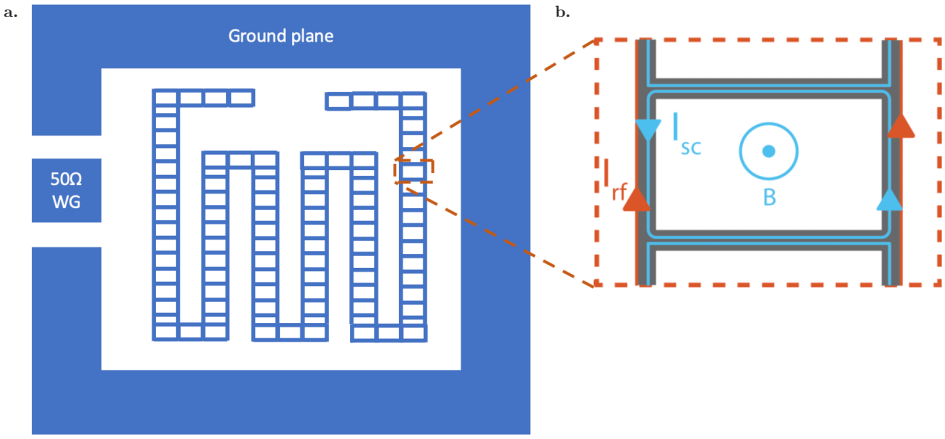

Figure 3.3: **Schematic of wireless tunable resonator. a.** Cartoon schematic of wireless tunable resonator. Blue area indicates superconductor. A 50Ω waveguide to feed and readout the circuit is shown on the left side of the image. **b.** An inset shows a unit cell which comprises the circuit and allows for improved inductive coupling. The red lines indicate the RF path which represents the microwave frequency mode. Applied magnetic field induces the circulating DC shown in blue

simulations we also run multi-resonator simulations to approximate cross-coupling between adjacent resonators.

3.6 Integration with Piezo-optomechanics

One final note regarding the design of these circuits is the integration with piezo-optomechanics which will impact our final design. There exist several approaches to this challenge including on-chip integration [30], flip-chip bonding [13] and more exotic techniques [69]. There are two main advantages of composite, multi-chip designs: one, the physical separation between the piezo-optomechanical and microwave chips substantially reduces the optical power scattered onto the superconductor, and two, separate chips allows for simplified fabrication process. However the challenges of this approach is coupling the two systems efficiently. The physical separation necessitates a cross-chip microwave interface between the piezomechanics and the microwave circuit which will inevitably reduce the piezoelectric coupling of the system. On the other hand, an integrated design with microwave circuit and piezo-optomechanics on the same chip we swap the advantages and challenges of the composite approach. As shown in [30] the scattered light from the piezo-optomechanics will disrupt the operation of the superconductor. In our design we plan to leverage the properties of NbN outlined in this chapter to develop a

light-robust transducer integrated with on-chip NbN circuits such that we gain the benefits of an integrated chip with superior optical power-handling capabilities. To this end, we will modifiy the circuit deisng to improve the integrated performance. To improve further improve the power-handling we will add long and wide terminals to the circuit to physically distance the narrow, light-sensitive portion from the piezo-optomechanics.

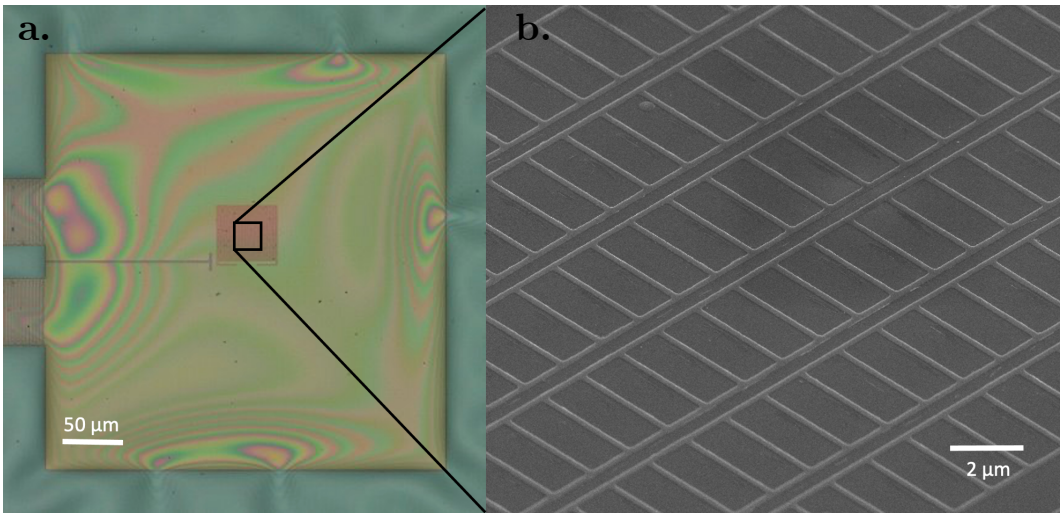

Figure 3.4: **Optical and SEM Image of NbN circuit.** **a.** Optical image of a fabricated NbN device on a suspended silicon membrane. **b.** Zoomed-in SEM image of the wireless tuning loops comprising the circuit.

Chapter 4

DEVELOPMENT AND CHARACTERIZATION OF LIGHT-ROBUST NBN CIRCUITS

In this chapter we will discuss in detail the development and characterization of the NbN circuits discussed in Chapter 3. This chapter will begin with a discussion of the nanofabrication and initial characterization of the circuits and finish with early measurements demonstrating the optical power-handling characteristics of our design.

4.1 Device Fabrication

This section lists the fabrication steps for realizing a NbN based circuits on a 1 $\times$ 1cm silicon-on-insulator (SOI) chip. The process is split into 3 layers.

Layer 1: This layer defines the Nb markers for lithographic alignment. The steps for this layer are detailed below:

1. Chip Cleaning
    - Acetone 5min sonication
    - IPA 5min sonication
    - N_2 blow dry
    - O_2 plasma clean at 150W, 12sccm O_2 flow for 2min
    - 15s dip in 10:1 Buffered HF followed by 2x 10s DI H_20 rinse
2. Spin/Bake
    - Pre-bake at 180°C for 3min
    - Spin ZEP 520a at 3000 rpm for 1 min
    - Post-bake at 180°C for 3min
3. E-Beam Lithography
    - Beam current 50nA
    - Fracturing resolution 20nm

- Dose 230 $\mu C/cm^2$

4. Development
    - ZED N50 for 2.5min
    - MIBK for 30s
    - N_2 blow dry
    - O_2 plasma ash at 150W, 12sccm O_2 flow for 2min
5. E-beam Evaporation of Nb
    - 15s BOE dip just before loading in evaporator to strip native oxide
    - Evaporate 150nm thick Nb at 0.4nm/s
6. Lift-off
    - NMP at 150°C for 2hr
    - Acetone 5min sonication
    - IPA 5min sonication
    - N_2 blow dry
    - O_2 plasma ash at 150W, 12sccm O_2 flow for 2min

At this stage, we have used e-beam lithography, e-beam evaporation, and metal lift-off to define our Nb markers which forms layer 1.
Layer 2: In the second layer we will define our NbN circuits. The steps are:

1. Bias Sputtering of NbN
    - 15s BOE dip just before loading in sputterer to strip native oxide
    - 50W RF bias sputter Nb with 5 sccm N_2
2. Spin/Bake
    - Pre-bake at 180°C for 3min
    - Spin ZEP 520a at 8000 rpm for 1 min
    - Post-bake at 180°C for 3min
3. E-Beam Lithography

- Beam current 1nA
- Fracturing resolution 2nm
- Base Dose 220 $\mu C/cm^2$

4. Development
    - ZED N50 for 2.5min
    - MIBK for 30s
    - N_2 blow dry
5. NbN Etching
    - SF_6/Ar reactive ion etch (RIE) 300W ICP (inductively coupled plasma) 30W RF
    - NMP at 150°C for 2hr
    - Acetone 5min sonication
    - IPA 5min sonication
    - N_2 blow dry
    - O_2 plasma ash at 150W, 12sccm O_2 flow for 2min

Layer 3: The final layer is layer 3 where we etch small holes through the silicon membrane to allow for etching of the sacrificial oxide layer. The steps are:

1. Spin/Bake
    - Pre-bake at 180°C for 3min
    - Spin ZEP 520a at 8000 rpm for 1 min
    - Post-bake at 180°C for 3min
2. E-Beam Lithography
    - Beam current 150pA
    - Fracturing resolution 1nm
    - Dose 220 $\mu C/cm^2$
3. Development
    - ZED N50 for 2.5min

- MIBK for 30s
- N_2 blow dry
- O_2 plasma ash at 150W, 12sccm O_2 flow for 2min

4. Si Etching
   - SF_6/C_4F_8 RIE 600W ICP, 18W RF
   - NMP at 150°C for 2hr
   - Acetone 5min sonication
   - IPA 5min sonication
   - N_2 blow dry
   - O_2 plasma ash at 150W, 12sccm O_2 flow for 2min
5. Membrane Release
   - SPTS uEtch vapor HF for 2 hours

4.2 Resistance and T_C Measurements

The first measurements to assess the properties of our NbN films are a room temperature measurement of sheet resistance and a measurement of the superconducting transition temperature (T_C). These two values will provide an estimate of the kinetic inductance of the film. The sheet resistance is measured with a 4-point probe and the measurements of T_C is performed in a 2K cryogen-free cryostat (Quantum Design PPMS). We then calculate the kinetic inductance of these films with $L_{sq} = \frac{\hbar R_{sq}}{1.76\pi k_b T_C}$.

4.3 Cryogenic Measurements of Frequency and Tuning

With the initial measurements of sheet resistance and T_C we can use the calculated L_{sq} to design wireless-tunable circuits with resonance frequency $f_0 \approx 5$GHz. These measurements are performed in a dilution refrigerator at a base temperature of T = 10 mK. The chip is wirebonded to a printed circuit board (PCB) with multiple 50 Ω co-planar waveguides. Each co-planar waveguide on the PCB is wirebonded to a corresponding co-planar waveguide on chip which is used to both excite and readout the circuit. Microwave connectors soldered to one side of the PCB allow for connection to cables leading out of the cryostat. Above the sample is a coil composed of thousands of loops of superconducting NbTi wire. With this coil we can apply several hundred mT magnetic field to the sample for in situ frequency

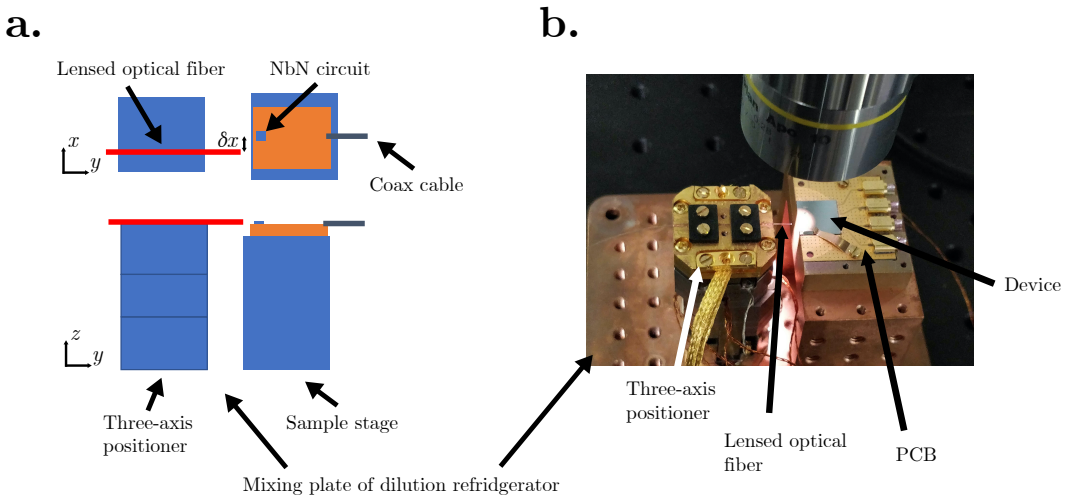

Figure 4.1: **Experimental setup for optical tests on NbN circuits. a.** Top and side vide schematics and **b.** Photograph of the experimental setup on the mixing plate of a dilution refrigerator

tuning. We begin by locating the resonators by performing a reflection measurement using a vector network analyzer (VNA). Once we have located the resonators, we tune the frequency by driving a current through the tuning coil.

4.4 Frequency Tuning Behavior

The frequency tuning is approximately quadratic with applied magnetic field. However when tuning slowly we see behavior deviating from this. In Fig. 4.2b we can see deviation from the expected quadratic tuning. We can measure the period of these oscillations and find they are exactly equal to the flux quantum for this geometry. This behavior is a result of flux quantization in the superconducting loops comprising our circuits. Another behavior measured on our devices is related

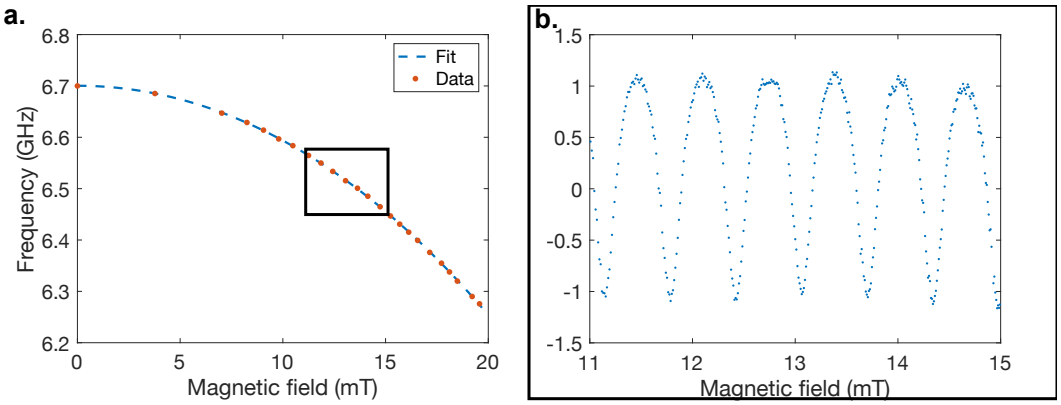

Figure 4.2: **Flux quantization through superconducting loops.** Fundamental frequency tuning via external magnetic field. **a.** Full tuning range where the magnetic field is ramped up as a function of the square root of the scan index. **b.** Zoom of the first plot. Frequency deviation from expected quadratic tuning background showing the period of the oscillations.

to the cricial current of the superconductor. When the induced current approaches critical current the resonator frequency no longer tunes quadratically. What we found in our experiments is that the behavior of the resonators becomes hysteretic in this regime. The signature of this is the 'turn-around current' where above a given current (approximately the critical current) the circuits become lossier and follows a different tuning trajectory which no longer corresponds to the original. This regime of operation is avoided if at all possible.

Chapter 5

NBN CIRCUIT RESPONSE TO OPTICAL ILLUMINATION

As discussed in the previous chapter, a key performance metric of the piezo-optomechanical transducer is the repetition rate. In the previous transducer with an integrated aluminum transmon qubit the repetition rate was limited by the quasiparticle (QP) relaxation rate of aluminum [48]. With the introduction of niobium nitride circuits we have circumvented the primary limitation of the previous transducer. However, QP relaxation time does not tell the whole story. To fully characterize the performance of the transducer under typical operating conditions the light-robust circuits need rigorous testing under similar conditions. To this end this chapter will be focused on characterizing these circuits under optical illumination to understand how they will impact performance in a full transducer as well as influence iteration on the design to further improve optical robustness. We will perform several experiments through this chapter to extract the information we are looking for. Starting with an experiment to determine the spatial character of the scattered light impinging on the superconductor. And later in the chapter we will move on to characterize the temporal performance of the circuits.

5.1 Geometry of Scattered Light

In this section we will focus on the spatial nature of light scattered during transduction. This information is key to informing and improving the design of the light robust circuits. To begin this section we can examine the geometry of the transducer to understand the sources of scattered light.

This experiment is set up such that the opposite side of the PCB is cut right to the edge of the chip to allow for a lensed optical fiber to be placed in close proximity to the chip. A 3-axis positioner is used to precisely position the optical fiber at various positions to qualify the various sources of scatter light (Fig. 4.1). The two main sources of scattered light we suspect are: one, light scattered from the edge of the chip, and two, light scattered from the OMC. Due to the limited coupling efficiency of this scheme about 60% of the light sent to the chip is not coupled into the waveguide. Most of this scattered light will not impinge on the superconductor, but a small fraction will. The high Q-factor of silicon OMCs implies the light scattering from this region is extremely small, however the close proximity to the

superconductor (relative to other sources) could make this a non-negligible source. The main goal of these experiments is to determine the relative magnitude of these sources and test methods to mitigate the total optical power impinging on the superconductor. In addition to these two modes of scattering we can also test the far-field scattering.

In the first experiment we parked the lensed optical fiber 2mm away from the optical coupler which leads to superconductor. This geometry is intended to test the far-field scattering from the lensed fiber. A 1550nm laser is used to illuminate the chip. We perform microwave spectroscopy on the NbN circuits as we apply 2μW of continuous wave (CW) optical power. At this distance we detected a 100 kHz frequency shift from the 5 GHz microwave mode. Now we will couple to the waveguide with maximal efficiency (30%). At this position we expect most of the illumination to originate from OMC scattering near the superconductor. Next we move the fiber 5 μm away from the coupler. In this position the scattering from the fiber should be identical to the maximally-coupled case, but now there is virtually no power reaching the OMC. In the coupled case we see a shift of 20MHz, and 1MHz in the uncoupled case. This result indicates both sources substantially effect the circuits, but the local scattering from the OMC represents a larger proportion of the impinging power on the superconductor. However, both sources have an effect on the circuits and should be mitigated as far as is possible.

Distance from coupler	**MW frequency shift**
2 mm	0.1 MHz
5 μm	1 MHz
0 μm	20 MHz

Table 5.1: Optically induced MW frequency shift

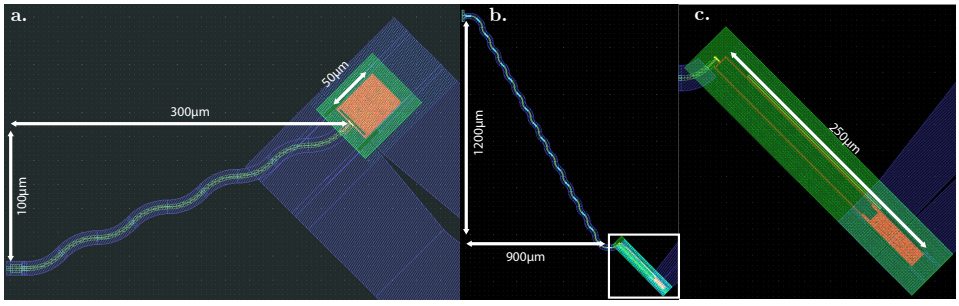

Figure 5.1: **Design changes for improved optical robustness. a.** Previous device design with dimensions indictating distance of fiber coupler to superconductor. **b.** Improved design showing increased distance from fiber coupler to superconductor**c.** Zoom in showing the changes to the superconducting circuit.

In the next series of experiments we modified the design to reduce the scattered light impinging on the circuits. The first change was to add long and wide superconducting terminals to spatially separate the narrow wire segments from the OMC. The second change is to increase the length of the on-chip waveguide to spatially separate the lensed fiber from the circuit. With these design changes we measured the effects of CW on the circuit and found we reduced the susceptibility by a 100X as seen in Fig. 5.2. Further, we can calculate the added noise photons in the MW circuit and find we add less than 0.5 noise quanta at 20 μW which is an order of magnitude higher power than typically used for OMC readout. With this data we can show our implementation of NbN circuits is, from an added noise perspective, very promising for quantum microwave to optical transduction.

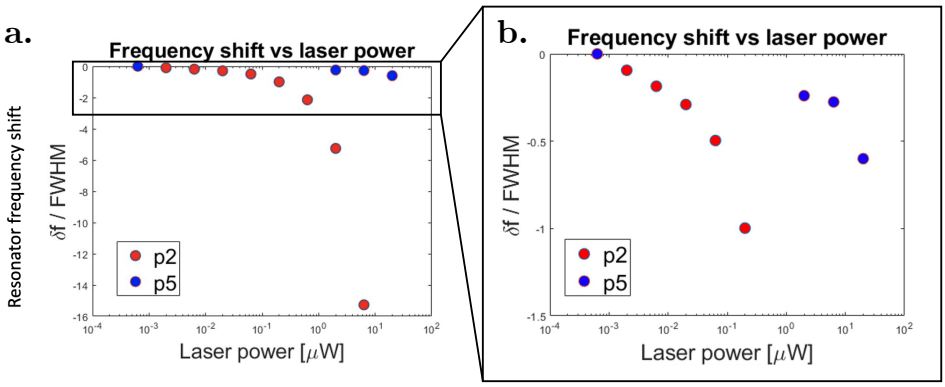

Figure 5.2: **MW frequency shift of improved device. a.** MW frequency shift under optical illumination of two devices. p2 represents the previous design and p5 is the improved design. **b.** Zoom in showing the improved performance.

5.2 Time Dynamics

Now we can move on to the time domain and start pulsed experiments to extract the time dynamics of the NbN circuits. The time dynamics of the optical response of NbN circuits is a key parameter in the performance of the transducer as it will set the rate at which we can effectively operate. An acousto-optic modulator (AOM) allows pulsing of the laser and is used to control both the duration and repetition rate of the pulse. A digital delay generator is used to maintain synchronization between the optical and microwave pulses used for readout. From these experiments we are able to extract a MW recovery time of 1.5μs. This observed recovery time is likely limited by the bandwidth of the circuit which is set by the total designed MW linewidth of 500MHz. This recovery time would allow for a transducer repetition rate 10,000X faster than the transducer with an aluminum circuit. In Fig. 5.3 We highlight two seperate effects with different timescales. First, we observe the fast

recovery which occurs within several μs which is attributed to the relaxation of QP in the superconductor. Second, is the slow-timescale heating of the circuit which takes several hundered μs to recover.

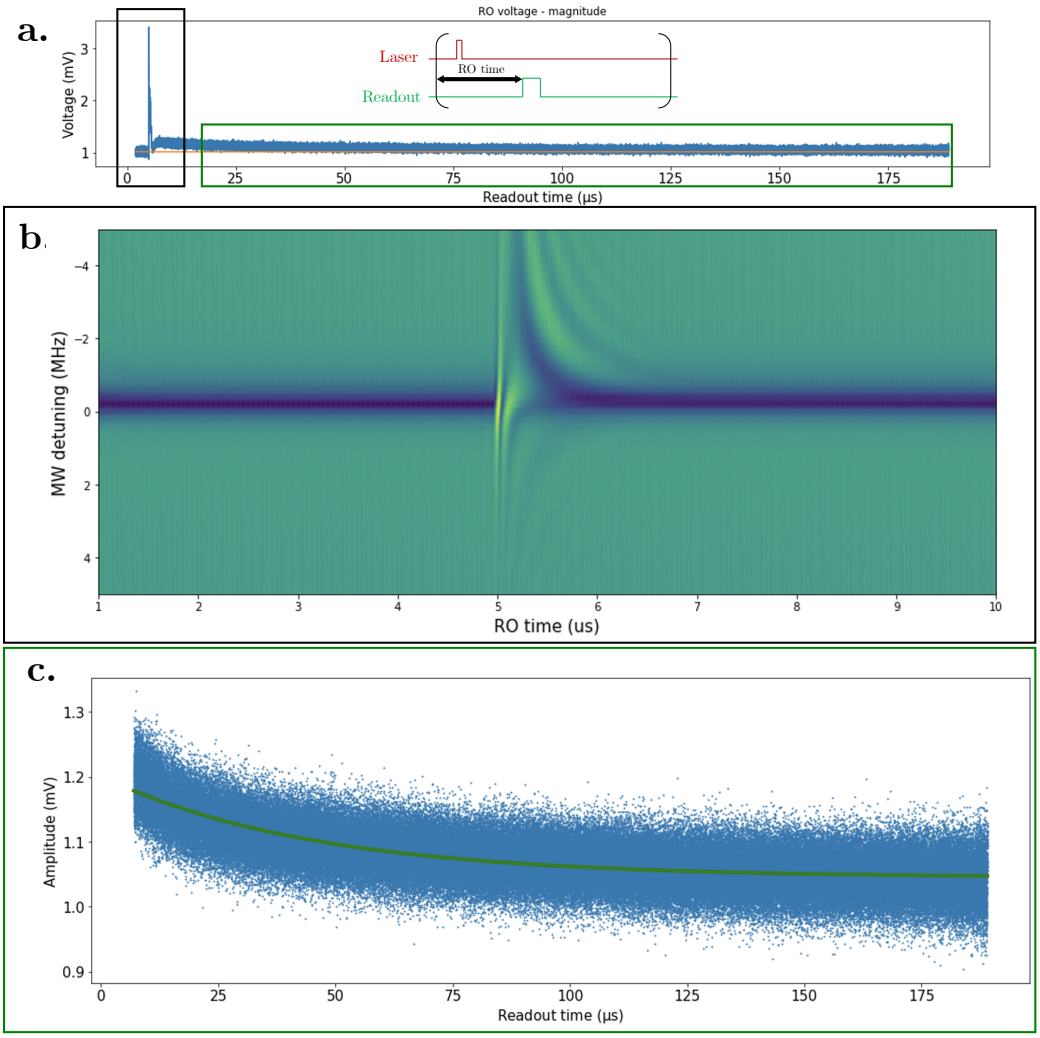

Figure 5.3: **Recovery of NbN circuit after laser illumination. a.** MW readout voltage following laser illumination with an inset showing the laser pulse sequence **b.** Zoom in showing fast recovery of NbN circuit within 2 μs. **c.** Zoom in showing slow recovery rate with timescale of 40 μs. Pump laser locked to 5GHz detuning from optical cavity. Pulse parameters: 100ns duration, 2mW peak power

5.3 MW Tuning with Optical Illumination

A successful transduction experiment requires simultaneous magnetic field for frequency tuning as well as optical illumination. To determine if these effects interact we performed a series of tuning experiments with a range of laser illumination powers. We found even very low optical powers similar to that used during previous transduction experiments was enought to reduce our total tuning range from about

10% to 3%. This is imporant to the device as fabrication-induced frequency disorder is large with these circuits and a reduced tuning range will reduce the total number of devices which land within the limited tuning range of the piezomechanics.

5.4 Conclusion

In conclusion, our measurements of the geometric and time dynamics response of a NbN circuit with optical illumination indicate that these circuits have an initial fast ($\sim 10\mu s$) recovery time when exposed to optical illumination. We also find evidence of a slower heating process that creates excess population 100 μs time scale. Power-dependent measurements indicate this slower process is likely thermal in origin. Given that the transducer device in [30] operates at 2 μW power with <100 ns pulse lengths, our measurements indicate that a repetition rate of 10 kHz would be achievable by replacing the all Al qubits in the device in [30] with NbN circuits. This would be a 1000x improvement over the repetition rate of 100 Hz reported in [30].

Chapter 6

PIEZO-OPTOMECHANICAL TRANSDUCER MODES OF OPERATION

In this chapter we will briefly discuss the different methods of operating a quantum microwave to optical transducer. In a classical transducer there is only one option, direct transduction and in the quantum device the method is very similar, albeit with smaller signals. However operating in the quantum regime provides an additional channel for communication based on quantum entanglement. In the next few sections we will discuss the different methods and the rationale for selection.

6.1 Direct Transduction

Direct quantum transduction is analogous to the classical case. By engineering a system with a beam-splitter type Hamiltonian we can directly convert between photons with disparate frequencies. In this case the channel for communication is clear, signals from microwave quantum devices are upconverted to optical photons then travel along a length of fiber, and finally, are downconverted back to microwave photons to interact with a distant microwave quantum device.

6.2 Entanglement Generation

Quantum entanglement is the unique feature of quantum physics that occurs when a group of particles can not be described independently (even when spatially separated) following the act of generation or interaction. A device capable of simultaneously generating photons of disparate frequency can be thought of a resource for entanglement. In other words, the photons generated by such a device would be entangled and can be used as a channel of communication over long distances.

6.3 Considerations for Selecting Mode

The main disadvantages of direct transduction are the stringent requirements of efficiency and added noise. A direct photon converter is capable of transferring quantum states only if the conversion efficiency $\eta < 1/2$ and small added noise [70]. With state of the art devices these figures are not realistic. However, by adding a classical two-way classical communication channel which heralds successful entanglement generation then completes quantum state transfer via teleportation we can avoid

these requirements. With this method, useful measurements of transduction are possible with state of the art devices.

Chapter 7

INTEGRATED LIGHT-ROBUST TRANSDUCER FABRICATION

In Chapter 4, we studied the optical response of niobium nitride (NbN) based circuits fabricated on a silicon-on-insulator (SOI) substrate. Our results showed a favorable quasiparticle recovery time for these NbN circuits compared to the all aluminum transmon qubits used in [30]. However, as discussed in Chapter 2, our transducer device is designed to be integrated on the same chip. To integrate our NbN circuits with our piezo-optomechanical transducer device, we need to develop a fabrication process for realizing this integrated platform. In this chapter we discuss some of the challenges associated with fabricating these light-robust NbN/AlN piezo-optomechanical transducers. A summary of the NbN/AlN transducer process is show here:

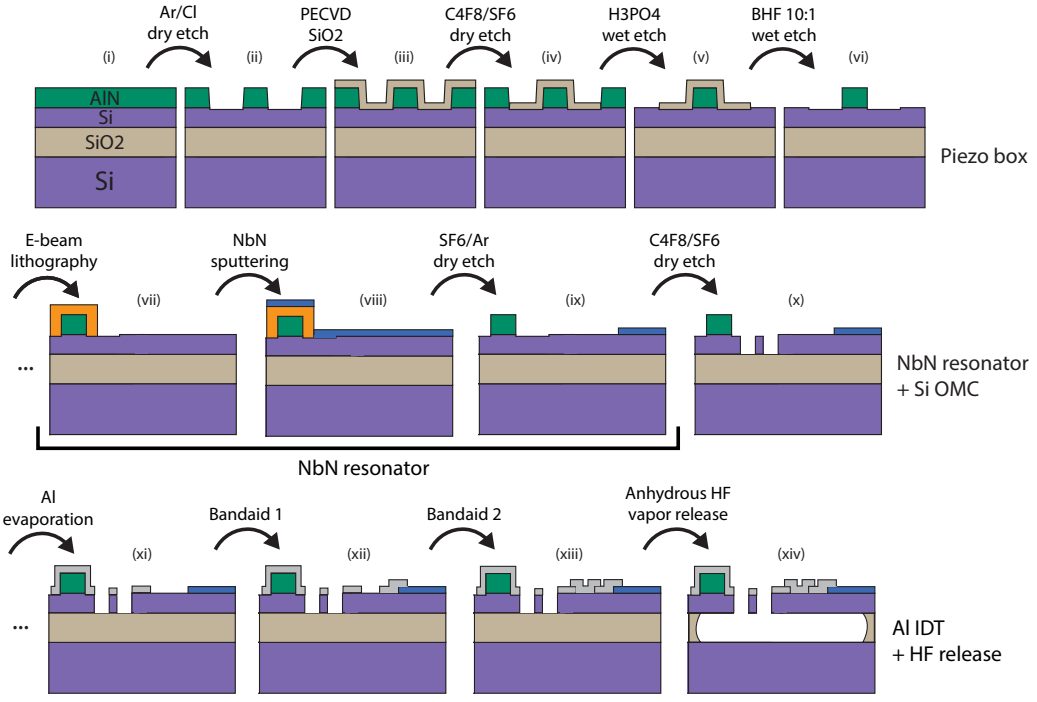

Figure 7.1: **Fabrication process for NbN/AlN transducer.**

7.1 Protection of Si Surface from NbN Etch

The first challenge we encountered in efforts to integrate our circuit fabrication with piezo-optomechanics is the effect of the NbN dry etch on the silicon undertheath. Optomechanical crystals (OMCs) are known to be sensitive to the surface roughness and thickness of the silicon layer they are patterned in. The etch chemistry used to etch the circuit geometry is not selective for NbN and in fact etches Si more quickly. This is problematic because the quality factor and wavelength of the OMCs varies dramatically based on the timing of the circuit etch. The primary issue is that our efficiency is reliant on a high Q OMC with a mechanical frequency which hybridizes well with the piezo-acoustic mode. Overetching of the silicon devices layer presented a large yield issue for our fabrication process.

Two potential solutions to the overetching are to use a liftoff process instead of etching the circuits or finding a more selective dry etch chemistry. Liftoff was not feasible due to the sputtering process we use to deposit NbN. Experiments with different etch chemistry did not find a better chemistry. Instead we took a middle ground approach where instead of lift-off across the entire circuit we placed a small patch of resist protecting the OMC region from the dry etch. The main downside for this approach (the reason we cannot do liftoff across the whole circuit) is that the sputtering process is conformal which makes liftoff difficult and can cause flagging to occur at the edges of the resist pattern as seen in Fig. 7.2.

Parameter	**Value**
ICP Power	300 W
RF Power	30 W
SF_6 Flow	20 sccm
Ar Flow	10 sccm
Temperature	15 C
Process Pressure	8 mTorr
Helium Backing Pressure	4 torr

Table 7.1: NbN etching parameters

Material	**Etch Rate**
NbN	10 nm/min
Silicon	60nm/min
AlN	2nm/min

Table 7.2: Etch rates of various materials in the NbN etch

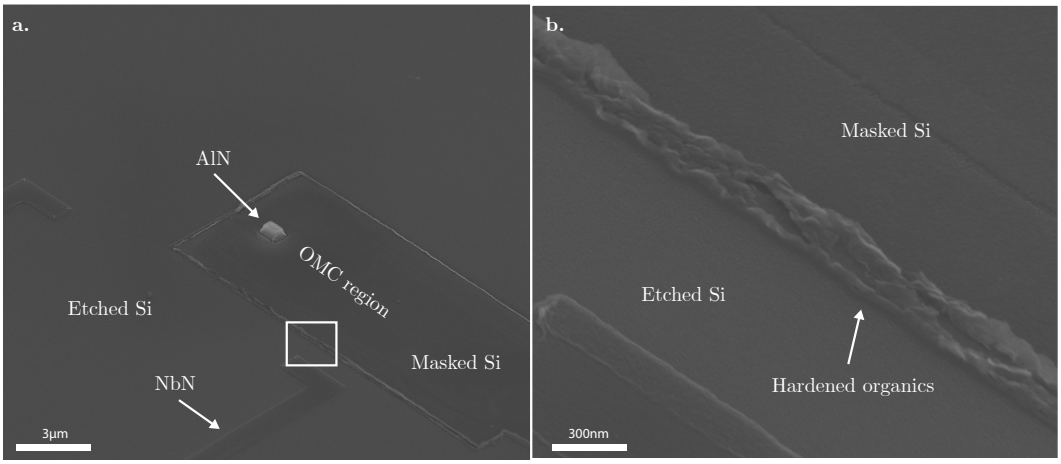

Figure 7.2: **SEM image of NbN etch with OMC protection region. a.** Image showing the device following the NbN etch with resist protection region for the OMC **b.** Zoom in of **a.** showing the hardened organics which form as a result of the protection region.

7.2 Large Suspended Membrane for NbN Circuit

To mitigate mechanical loss through the substrate the piezo-optomechanical transducer is fabricated on a silicon-on-insulator (SOI) substrate. This allows the selective removal of sacrificial silicon dioxide layer releasing a portion of the silicon device layer leaving a suspended membrane with an air gap between the patterned device and the substrate. The challenge related to this is that the sacrificial oxide layer is uniform across the entire substrate and is has large dielectric loss tangent compared to silicon. To mitigate dielectric loss the oxide layer must be removed which releases the entire area the circuit takes up. The relatively large footprint of the circuit ($25{,}000\mu m^2$) introduces a few challenges into the fabrication process. The first challenge is the stability of the membrane itself. Our SOI substrates have a silicon device layer which is under compressive stress such that when the membranes are released they tend to buckle down towards the substrate. The concern is that if the circuit do not buckle the same way there will be some uncertainty in the frequency of the circuits due to the changing dielectric environment as there is a large difference in the dielectric constant between silicon and vacuum. To mitigate this issue we sacrificed the Q-factor of the circuits to bring the edge of the released membrane as close to the circuits as possible. This brings the lossy oxide close to the circuits in exchange for a smaller, more stable released structure. Another challenge of this large buckling is the effect on the piezo-optomechanics. The circuit and mechanics are in close proximity to eachother and were originally released on the same mebrane. We found this caused extra displacement in the piezo-optomechanics shifting frequencies and Q-factors. To mitigate this issue we added an unreleased island of

oxide as a support mechanism between the circuit and piezo-optomechanics.

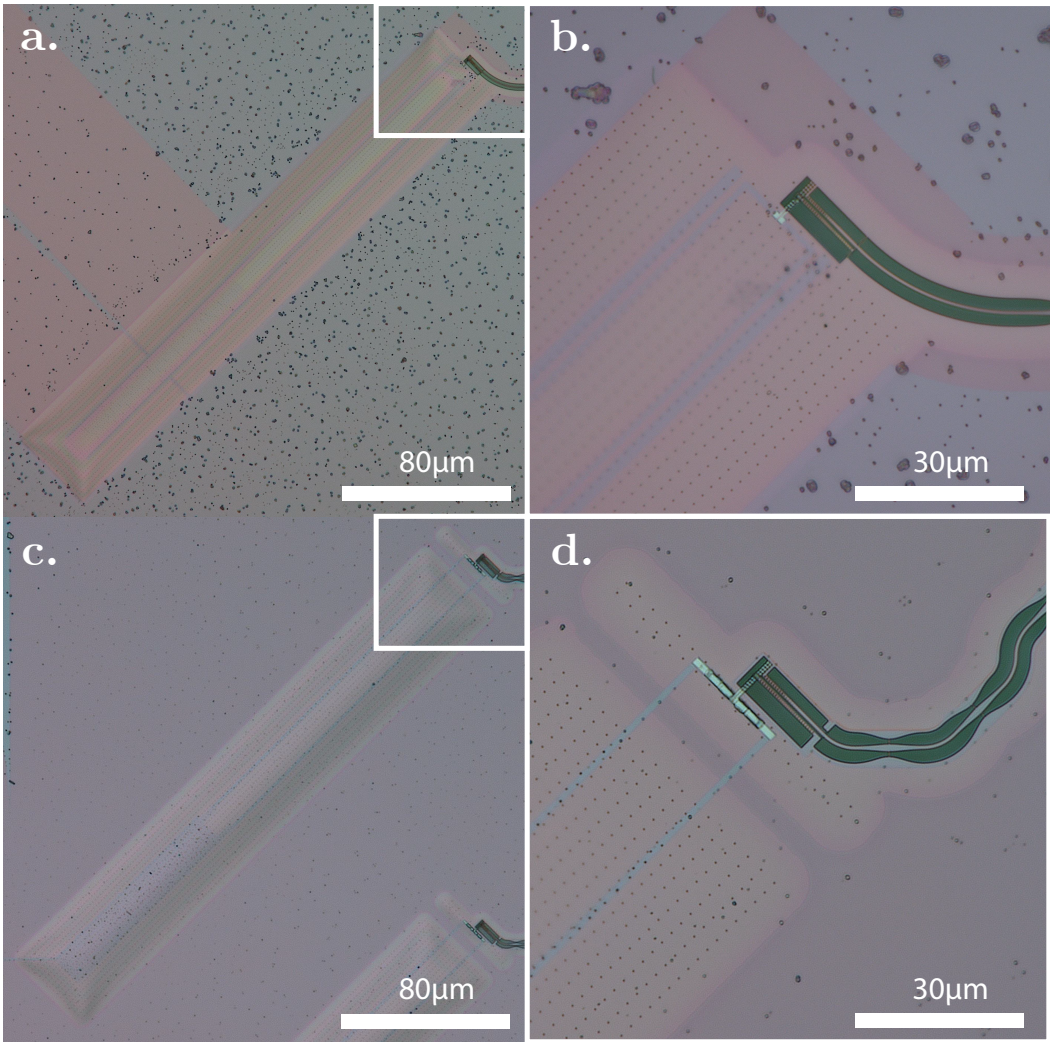

Figure 7.3: **Optical images of stress reduction design. a.** Image showing the device following VHF release without stress reduction design. **b.** Zoom in of **a. c.** Image showing device with stress reduction bridge between the NbN circuit and the piezomechanics. **d.** Zoom in of **c.**

7.3 NbN Fabrication-induced Frequency Disorder

A key component of our system to achieve maximal efficiency is resonant frequency alignment. Given the variety of materials and small feature sizes of our device precise and accurate alignment of the modes can be very challenging. One of the more sensitive components to fabrication-induced frequency disorder is the NbN circuit. Because our superconductor films are so thin to maintain a large fraction of kinetic inductance they are susceptible to small changes in the thickness. The kinetic inductance of these films is superlinear with film thickness because not only does the geometry effect the kinetic inductance, but so do the material properties of

the film. As films grow thicker the lattice constant mismatch between the substrate and deposited film lessens and the film becomes more ordered. In the regime where this effect plays an important role (<100nm for NbN) thinning the film will linearly increase the current density in the film for a given current and this will be compounded with the change in the material properties due to the more disorder in thinner films. The order of this superlinear relation is not clear and is very sensitive to the material properties and growth of the superconductor. This indicates that a 10% change in the thickness of these films could induce a 3-5% change in circuit frequency. For the 10nm thick films we have discussed in previous chapters this would require a 1nm unintended change in thickness. With the complicated fabrication procedure outlined at the beginning of this chapter it is possible to do much worse than 1nm uncertainty and this is the primary concern of this section.

Most metal thin films are known to develop a native passivation layer on the surface following deposition. This layer typically converts the top few nanometers of the film to a more atmosphere-stable compound (Al_2O_3 for aluminum for example). For most traditional superconducting films like aluminum or niobium the native oxide layer is grown within seconds or hours following exposure to atmosphere. However, NbN is known to have a long passivation period (up to a few weeks) and if not accounted for carefully can cause apparent disorder in the circuit frequencies [71]. The fabrication processing time can vary greatly from 2 weeks to more than a month so it is vital to control this variability. One approach to remove this uncertainty is to wait a set time following film deposition for the passivation process to complete before measuring the circuits. Another aspect to this disorder is the additional processing which the NbN is exposed to during the steps required to complete the transducer. The main culprit for modifying the film properties during the extra steps is the substrate cleaning we perform in between lithography. This step involves a gentle oxygen plasma cleaning, but it is possible this process is damaging our superconductor film. These cleaning steps however are required so the best we can do is ensure consistency such that the films are uniformly effected by the cleaning. This can be challenging to changing chamber conditions in the plasma cleaner which may effect the plasma density and intensity. The minimum benchmark to clear is our frequency disorder must be less than our in situ frequency tuning range of about 10%.

In addition to disorder of the film thickness we also have disorder of the nanowire width. The widths of the wires depend on the lateral etch rate of the dry etch as well

as the resist erosion during the etch. Both of these factors can vary significantly run-to-run, but also vary across the chip. For instance, we have found a ± 10nm difference in lateral nanowire dimensions which will not impact the circuit frequency as strongly as thickness, but will add more disorder.

7.4 Optical Waveguide Buckling

Similar to the mechanical stability issues we encountered with the large released membranes supporting the NbN circuits we encounter similar challenges with the optical waveguide used to feed and readout the optomechanics (OMC). As discussed in Chapter 2 we have extended the length of the on-chip optical waveguide to reduce the scattered light impinging on the superconductor. We found the increase in length greatly improved the optical power handling capabilities of the device, but instability and buckling were common issues with the first devices.

The primary failure mode was the suspended waveguide would buckle and collapse into the underlying substrate following vapor HF (VHF) release. Once collapsed the waveguide could not be recovered and the loss of the waveguide became too large for productive measurements of the OMC. The coupling rate between the waveguide and OMC is set by the distance separating the two features. Due to the large stress and deflection from the buckling the distance between the coupler and OMC were highly disordered causing some devices to be suboptimally undercoupled and some overcoupled. Both situations result in an impracticle device. In the undercoupled case it is challenging to measure due to low signal levels and in the overcoupled case the OMC Q-factor becomes limited by the coupler and suffers a substantial reduction in Q-factor, reducing the conversion efficiency of the devices.

As discussed in Chapter 2 the efficiency of a transducer is set not only by the transducer itself, but the chain of readout as well. By adding loss channels to the optical waveguide we would be effectively reducing the efficiency of the system. To avoid this we suspend the optical waveguide with the fewest number of supporting tether structures as possible, but the fewer the number, the lower the mechanical stability. This issue is further emphasized with a waveguide which extends for more than 1mm, typically having hundreds of tethers. The scattering of each tether points and the waveguide becomes not only very lossy, but also develops a background with large ripple, further reducing the readout efficiency of the device.

Our approach to mitigate this issue was to design tether with lower loss and better mechanical stability. Typically the size of the tether is proportional to the magnitude

of loss, but by designing a waveguide which varies adiabatically with the period of tethers we plan to mitigate these losses. Simulations performed in lumerical show a reduction of blank to the loss of the tethers. Additionally, the adiabatic variation reduces the length of the individual tethers reducing the torsional flexibilty, adding further resistance to buckling. With these adiabatic tethers we found our devices more reliably released without collapsing and our waveguide background ripple improved substantially. In addition to the design changes of the optical waveguide the addition of the unreleased bridge demonstrated in Fig. 7.3. This unreleased region mitigates the stress from the large MW membrane being transfered to the fragile optical waveguide.

Parameter	**Value**
ICP Power	1200 W
RF Power	23 W
SF_6 Flow	16 sccm
C_4F_8 Flow	40 sccm
Temperature	15 C
Process Pressure	10 mTorr
Helium Backing Pressure	4 torr

Table 7.3: VHF release holes etching parameters

7.5 Dicing Saw for Endfire Coupler

The typical method for exposing the optical waveguide for lensed fiber endfire-coupling is deep reactive ion etching (DRIE). In this proceedure we etch a deep trench through the silicon substrate to expose the end of the chip and allow space for the fiber to approach the on-chip waveguide without bumping into the substrate underneath. This requires deep etching into the silicon substrate (300um) and the process generates signifcant heating in the resist used to protect the device during this process. This step occasionally burns the resist making it difficult to remove following DRIE. To improve the cleanliness of this process we explored alternate methods to expose the endfire coupler.

The primary method explored in our work utilizes a dicing saw to expose the coupler. Dicing saws are typically used to separate a processed wafer into many individual dies. In our case, we will use the saw to cut very close to the edge of the coupler. The alignment of the saw with the coupler was challenging because cutting the waveguide would ruin the coupler, but cutting too far from the coupler would make it so the lensed fiber would bump into the substrate when attempting to couple.

However, the optical microscope built into the saw worked well enough. We found after several successful dicings that the coupling efficiency of endfire coupling with this method was not comparable to DRIE. Our hypothesis is that the dicing saw may add some residual stress to the waveguide as it travels close by. The added stress may cause buckling in the coupler which rotates its axis out of plane. The rotational alignment of the coupler with the lensed optical fiber has a large effect on coupling efficiency and is not easily adjusted for. Following these initial experiments we decided to return to the DRIE process.

7.6 Fabrication Procedure

Layer 1: Cr/Au Markers:

1. Chip Cleaning
    - Acetone 5min sonication
    - IPA 5min sonication
    - N_2 blow dry
    - Plasma ash at 150W, 12 sccm O_2 flow for 2min
2. Spin/Bake ZEP 520a
    - Pre-bake at 180°C for 3min
    - Spin ZEP 520a at 3000 rpm for 1 min
    - Post-bake at 180°C for 3min
3. E-Beam Lithography
    - Beam current 1nA
    - Fracturing resolution 2nm
    - Dose 250 $\mu C/cm^2$
4. Development
    - ZED N50 for 2.5min
    - MIBK for 30s
    - N_2 blow dry
    - Plasma ash at 150W, 12 sccm O_2 flow for 2 min

5. Cr/Au Deposition

    - 15s dip in 10:1 Buffered HF followed by 2x 10s DI H20 rinse—this step etches away the native silicon-oxide on the surface of the substrate and is done right before loading the chip in the evaporator for a clean oxide-free Cr-Si interface
    - Evaportate 15 nm Cr at 0.05 nm/s and 100nm Au 0.1 nm/s

6. Cr/Au Liftoff

    - NMP heated to 150°C for 2 hours
    - Acetone 5min sonication
    - IPA 5min sonication
    - Plasma ash at 150W, 12 sccm O_2 flow for 5min

Layer 2: AlN Trench Etch:

1. Spin/Bake

    - Pre-bake at 180°C for 3min
    - Spin ZEP 520a at 3000 rpm for 1min
    - Post-bake at 180°C for 3min
    - Spin ZEP 520a at 3000 rpm for 1min
    - Post-bake at 180°C for 3min

2. E-Beam Lithography

    - Beam current 1nA
    - Fracturing resolution 2nm
    - Dose 290 $\mu C/cm^2$

3. Development

    - ZED N50 for 2.5min
    - MIBK for 30s
    - N_2 blow dry
    - Plasma ash at 150W, 12 sccm O_2 flow for 2 min

4. ICP-RIE Etching of AlN
    - 3min Ar:Cl_2 10:20sccm, 300W ICP, 30W RF 10 mTorr
5. Resist strip
    - NMP heated to 150°C for 2 hours
    - Acetone 5min sonication
    - IPA 5min sonication
    - Plasma ash at 150W, 12 sccm O_2 flow for 5min

Layer 3: AlN Wet Etch

1. PECVD Oxide Growth
    - 4min SiH_4:N_2O 42:838 sccm, 20W HF, 1000 mTorr, 350°C
2. Spin/Bake
    - Pre-bake at 180°C for 3min
    - Spin ZEP 520a at 3000 rpm for 1min
    - Post-bake at 180°C for 3min
3. E-Beam Lithography
    - Beam current 1/100nA
    - Fracturing resolution 2/25nm
    - Dose 250 $\mu C/cm^2$
4. Development
    - ZED N50 for 2.5min
    - MIBK for 30s
    - N_2 blow dry
    - Plasma ash at 150W, 12 sccm O_2 flow for 2 min
5. ICP-RIE Etching of Oxide Mask
    - 6min C_4F_8:O_2 40:3sccm, 1300W ICP, 33W RF 10 mTorr

6. Resist strip
    - NMP heated to 150°C for 2 hours
    - Acetone 5min sonication
    - IPA 5min sonication
    - Plasma ash at 150W, 12 sccm O_2 flow for 5min
7. Wet Etch of AlN
    - 12min 85% phosphoric acid heated to 80°C
8. Oxide Mask Strip
    - 3.5min 1:10 buffered HF

Layer 4: OMC Protection Mask

1. Spin/Bake
    - Pre-bake at 180°C for 3min
    - Spin ZEP 520a at 3000 rpm for 1min
    - Post-bake at 180°C for 3min
2. E-Beam Lithography
    - Beam current 100nA
    - Fracturing resolution 25nm
    - Dose 250 $\mu C/cm^2$

Layer 5: NbN Resonators

1. NbN Sputtering
    - 10nm 50W RF bias
2. Spin/Bake
    - Pre-bake at 180°C for 3min
    - Spin ZEP 520a at 8000 rpm for 1min

- Post-bake at 180°C for 3min

3. E-Beam Lithography
   - Beam current 1nA
   - Fracturing resolution 2nm
   - Dose 250 $\mu C/cm^2$
4. ICP-RIE Etching of NbN
   - 1min SF_6:Ar 20:10sccm, 300W ICP, 30W RF, 10mTorr
5. Resist strip
   - NMP heated to 150°C for 2 hours
   - Acetone 5min sonication
   - IPA 5min sonication
   - Plasma ash at 150W, 12 sccm O_2 flow for 5min

Layer 5: NbN Resonators

1. NbN Sputtering
   - 10nm 50W RF bias
2. Spin/Bake
   - Pre-bake at 180°C for 3min
   - Spin ZEP 520a at 8000 rpm for 1min
   - Post-bake at 180°C for 3min
3. E-Beam Lithography
   - Beam current 1nA
   - Fracturing resolution 2nm
   - Dose 250 $\mu C/cm^2$
4. ICP-RIE Etching of NbN
   - 1min SF_6:Ar 20:10sccm, 300W ICP, 30W RF, 10mTorr

5. Resist strip
    - NMP heated to 150°C for 2 hours
    - Acetone 5min sonication
    - IPA 5min sonication
    - Plasma ash at 150W, 12 sccm O_2 flow for 5min

Layer 6: OMCs

1. Spin/Bake
    - Pre-bake at 180°C for 3min
    - Spin ZEP 520a at 8000 rpm for 1min
    - Post-bake at 180°C for 3min
2. E-Beam Lithography
    - Beam current 150pA
    - Fracturing resolution 2nm
    - Dose 220 $\mu C/cm^2$
3. ICP-RIE Etching of Si
    - 4min SF_6:C_4F_8 72:30sccm, 600W ICP, 18W RF, 10mTorr
4. Resist strip
    - NMP heated to 150°C for 2 hours
    - Acetone 5min sonication
    - IPA 5min sonication
    - Plasma ash at 150W, 12 sccm O_2 flow for 5min

Layer 7: Al Terminals

1. Spin/Bake
    - Pre-bake at 180°C for 3min
    - Spin ZEP 520a at 3000 rpm for 1min

- Post-bake at 180°C for 3min

2. E-Beam Lithography
    - Beam current 1nA
    - Fracturing resolution 3nm
    - Dose 250 $\mu C/cm^2$
3. Aluminum Evaporation
    - 100nm angled evaporation of Al, +-15°
4. Lift-off
    - NMP heated to 150°C for 2 hours
    - Acetone 5min sonication
    - IPA 5min sonication
    - Plasma ash at 150W, 12 sccm O_2 flow for 5min

Layer 8: Bandaid 1

1. Spin/Bake
    - Pre-bake at 180°C for 3min
    - Spin ZEP 520a at 3000 rpm for 1min
    - Post-bake at 180°C for 3min
2. E-Beam Lithography
    - Beam current 1nA
    - Fracturing resolution 3nm
    - Dose 250 $\mu C/cm^2$
3. Aluminum Evaporation
    - 2min Ar mill 400V, 20mA
    - 60nm evaporation of Al
4. Lift-off

- NMP heated to 150°C for 2 hours
- Acetone 5min sonication
- IPA 5min sonication
- Plasma ash at 150W, 12 sccm O_2 flow for 5min

Layer 9: Bandaid 2

1. Spin/Bake
   - Pre-bake at 180°C for 3min
   - Spin ZEP 520a at 3000 rpm for 1min
   - Post-bake at 180°C for 3min
2. E-Beam Lithography
   - Beam current 1nA
   - Fracturing resolution 3nm
   - Dose 250 $\mu C/cm^2$
3. Aluminum Evaporation
   - 6min Ar mill 400V, 20mA
   - 60nm evaporation of Al
4. Lift-off
   - NMP heated to 150°C for 2 hours
   - Acetone 5min sonication
   - IPA 5min sonication
   - Plasma ash at 150W, 12 sccm O_2 flow for 5min

Layer 9: Mechanical Release

1. VHF
   - 2.5hrs of VHF

Chapter 8

INTEGRATED LIGHT-ROBUST TRANSDUCER CHARACTERIZATION

In this chapter we will characterize the transducer devices we have developed during my time at Caltech. We will start with preliminary optical and microwave spectroscopy to characterize the basic features of the device like microwave/optical Q-factors, frequencies and mode-couplings. Following spectroscopy we will introduce and perform our experiment for generating entangle photon pairs via spontaneous parameteric down conversion (SPDC). We will then discuss the results and analysis of the photon pairs. Finally we will discuss ongoing measurements to show our device violates the CHSH inequality as as further proof of entanglement.

8.1 Transducer Device Summary

Fig. 8.1a shows a conceptual schematic highlighting the resonator modes involved in our transduction experiment. Interaction between an optical mode, $\hat{a}$ and a microwave-frequency acoustic mode, $\hat{b}$ is mediated by a pump laser driving an optomechanical cavity in the resolved sideband regime. Simultaneously, the acoustic mode is resonantly coupled to a microwave-frequency electrical mode, $\hat{c}$ via the piezoelectric effect. We can write the Hamiltonian for this system as

$$\hat{H}/\hbar = -\Delta_a \hat{a}^\dagger \hat{a} + \omega_b \hat{b}^\dagger \hat{b} + \omega_c \hat{c}^\dagger \hat{c} + \hat{H}_{\mathrm{om}}/\hbar + \hat{H}_{\mathrm{pe}}/\hbar. \tag{8.1}$$

Here ω_b, ω_c are the frequencies of the modes $\hat{b}, \hat{c}$, respectively, and $\hat{H}_{\mathrm{om}}, \hat{H}_{\mathrm{pe}}$ are the optomechanical and piezoelectric interaction Hamiltonians described in more detail below. $\Delta_a = \omega_{\mathrm{p}} - \omega_a$ is the difference between the frequency of the optical pump, ω_{p} and that of the optical mode, ω_a. Setting the frequency of the pump laser to be red ($\Delta_a < 0$) or blue detuned ($\Delta_a > 0$) with respect to the optical cavity resonance allows us to select either beam-splitter or two-mode squeezing interactions, respectively [31]. The first setting can be used to transfer states between the acoustic mode and the optical mode when the transducer is operated as a frequency converter [48, 72, 73]. In this work, we use the latter setting to generate non-classical pairs of optical photons and acoustic phonons in an SPDC process. This choice is motivated by recent proposals for heralded remote entanglement generation which indicate that operation in SPDC mode relaxes the efficiency requirements for piezo-optomechanical

transducers [74–76]. In this setting, we have $\hat{H}_{\rm om}/\hbar = -G_{\rm om}(t)(\hat{a}^\dagger\hat{b}^\dagger + \hat{a}\hat{b})$. The time-dependent optomechanical coupling rate $G_{\rm om}(t) = \sqrt{n_a(t)}g_{\rm om}$ is controlled parametrically via the intra-cavity photon population $n_a(t)$ due to the detuned pump laser. Here $g_{\rm om}$ denotes the optomechanical coupling rate at the single optical photon and acoustic phonon level. The piezoelectric interaction is described by the beam-splitter Hamiltonian $\hat{H}_{\rm pe}/\hbar = -g_{\rm pe}(\hat{b}^\dagger\hat{c} + \hat{b}\hat{c}^\dagger)$. Here $g_{\rm pe}$ denotes the piezoelectric coupling rate at the single microwave photon and acoustic phonon level. This interaction can be used to map the acoustic component of the optomechanical two-mode squeezed state onto the microwave electrical mode. In the absence of any added noise, the joint state of the modes, $\hat{a}, \hat{c}$ can be described in the photon number basis by the wavefunction $|\psi\rangle = |00\rangle + \sqrt{p}\,|11\rangle + p\,|22\rangle + O(p^{3/2})$. For a weak pump field, the higher order terms with more than one excitation may be neglected. Detection of a single optical photon with probability, $p \ll 1$ can then be used to discard the vacuum component of this state, and show that single optical and microwave photons are produced strictly in pairs. Further, the optical measurement heralds a single microwave photon, a non-Gaussian state with a vanishing $g^{(2)}$.

Figure 8.1b shows the physical schematic of our chip-scale device, which consists of a half-wavelength superconducting kinetic inductance resonator [77] coupled to a piezo-optomechanical transducer. The transducer itself comprises a half-wavelength aluminum nitride (AlN) piezo-acoustic cavity attached to a silicon optomechanical crystal (OMC) resonator via an acoustic waveguide [48]. We achieve piezoelectric coupling in our system by using the two end terminals of the microwave resonator as electrical leads over the AlN section of the transducer. The microwave resonator is patterned in a disordered, thin film of NbN in a meandering ladder geometry. The inclusion of closed loops in the thin superconducting film, as shown in Fig. 8.1c, allows for tuning of kinetic inductance, and hence tuning of the frequency of the microwave resonator via an external magnetic field [78]. Using narrow superconducting wires in a meandering geometry results in high impedance, which helps us achieve strong piezoelectric coupling, $g_{\rm pe}$ with a small acoustic mode volume [79]. This design strategy is followed to maximize the fraction of acoustic energy in silicon, which has the lowest acoustic loss in our material stack. The NbN resonator is capacitively coupled to a 50Ω transmission line (not shown in schematic) to facilitate microwave spectroscopy of the transducer. Likewise, the optical cavity is coupled to a waveguide, which terminates in a tapered coupler at the edge of the chip allowing for efficient coupling to a lensed optical fiber. The layout of our device is chosen to reduce optical flux from stray pump light at the microwave resonator. We

use an ∼1 mm long optical waveguide to physically separate the circuit section of the transducer from the optical coupler, where there is significant scattering of pump light. Adiabatically tapered tethers, designed for low scattering loss, are used to anchor this suspended waveguide to the bulk of the device layer [79]. Additionally, we use extended electrical terminals to physically separate the optically sensitive current anti-node of the kinetic inductance resonator from the OMC, and reduce the impact of local pump scattering.

8.2 Measurement Setup

The measurement setup used in this work is detailed in Fig. 8.2. For SPDC experiments, trigger signals from a master digital delay generator are used to synchronize optical pump pulses with the timing window used for optical and microwave readout. Optical pump pulses with > 120 dB extinction are generated using two analog acousto-optic modulators (G&H Photonics) and are routed via a circulator into the 'Optics in/out' path towards the device in the dilution fridge as shown in Fig.8.2a. The optical emission from the device passes through the same circulator and is directed to a pump filtering setup prior to single photon detection (SPD) along the 'SPD in' path in Fig. 8.2a. The filtering setup comprises two tunable Fabry–Perot filter cavities (Stable Laser Systems) in series and provides 104 dB extinction for a pump detuning of 5 GHz along with a transmission bandwidth of 2.7 MHz. This transmission bandwidth naturally excludes emission due to optomechanical scattering by other transducer modes besides the two hybridized electromechanical modes of interest, $\hat{c}_{\pm}$. During the experiment, transmission through the filters is checked every four minutes and a lock sequence is initiated if the transmission drops below a set threshold. At the beginning of the transmission check, the optical path is set to bypass the fridge via a MEMS switch. An electro-optic phase modulator (ϕ-m in Fig. 8.2a) is used to generate a sideband on the pump tone at the target frequency to which the filters are locked. In our SPDC experiments, this target frequency corresponds to a pump detuning, $\Delta_a = (\omega_+ + \omega_-)/2$. If required, the locking algorithm adjusts the filter cavities to maximize transmission at the target frequency by monitoring the output of each cavity on a separate photodetector. Additionally, during long measurements, we periodically monitor the polarization of the pump light sent to the device and compensate for long term polarization drifts along the excitation path. Active polarization control is preformed by using an electronic polarization controller (Phoenix Photonics) and maximizing the optical pump power reflected by the device.

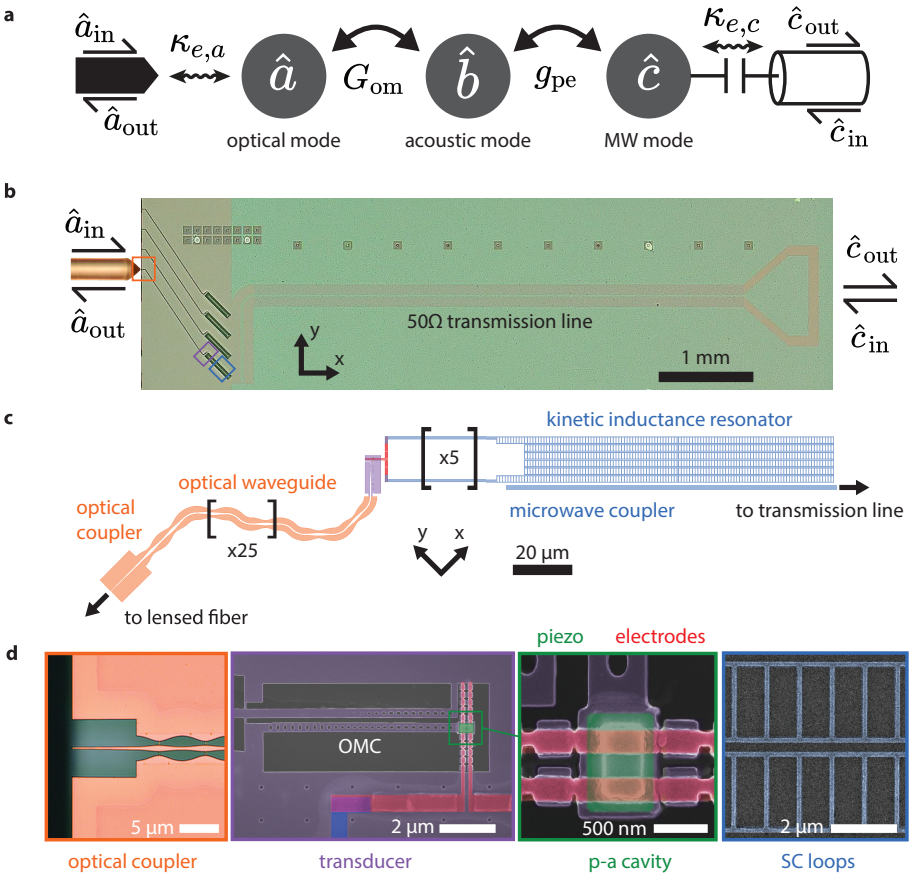

Figure 8.1: **Quantum transducer summary. a.** Transducer mode schematic indicating optical ($\hat{a}$), acoustic ($\hat{b}$) and microwave ($\hat{c}$) modes along with interaction rates for optomechanical coupling (G_{om}) and piezoelectric coupling (g_{pe}), respectively. The optical and microwave modes are coupled to waveguides with external coupling rates, $\kappa_{e,a}$ and $\kappa_{e,c}$, respectively. The input and output modes in the optical and microwave waveguides are denoted by $\hat{a}_{\mathrm{in}}, \hat{a}_{\mathrm{out}}, \hat{c}_{\mathrm{in}}, \hat{c}_{\mathrm{out}}$, respectively. **b.** Micrograph of transducer device showing optical access via lensed fiber on the left and microwave access via 50Ω transmission line on the right. **c.** Device schematic. From left to right, suspended optical waveguide (orange) leading to the piezo-optomechanical transducer (purple) whose electrical terminals (red) are connected to a microwave kinetic inductance resonator (blue). **d.** Micrographs of various components of the transducer. From left to right: optical micrograph of the coupler section at the end of the optical waveguide; scanning electron micrograph of the transducer indicating the silicon optomechanical crystal (OMC) cavity in purple; close-up of the piezo-acoustic (p-a) cavity highlighting the piezoelectric material in green and electrodes in red; scanning electron micrograph of the superconducting (SC) loops in the meandering ladder trace of the kinetic inductance resonator.

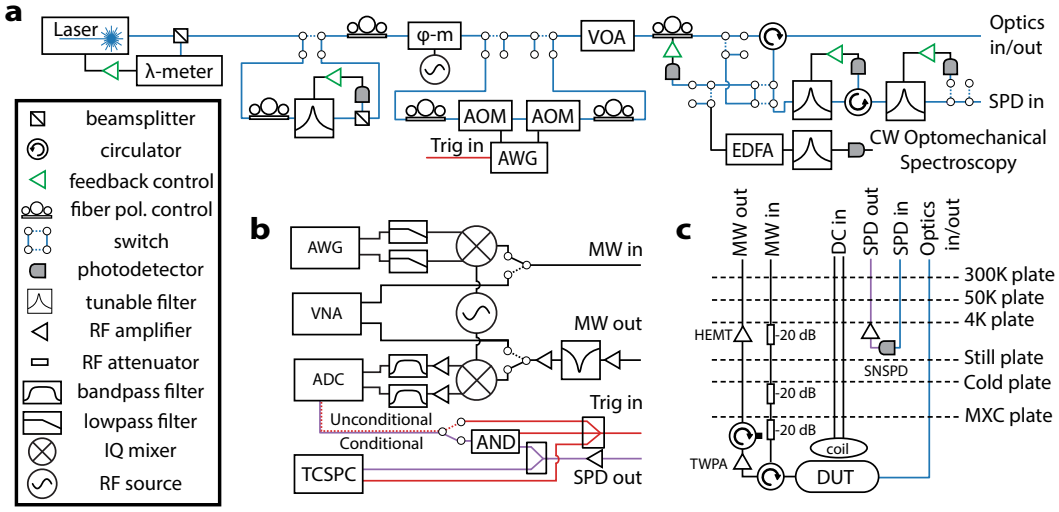

Figure 8.2: **Experimental setup. a.** Optical pulse synthesis and detection. An external cavity diode laser is wavelength locked to a wavemeter, and a 50 MHz tunable narrowband filter is used to remove spontaneous emission noise. ϕ-m denotes an electro-optic phase modulator, which is used during the locking sequence for the pump filter bank in the detection path. Optical pulse shaping is achieved by modulating the laser with two acousto-optic modulators (AOMs) connected in series. The envelope for the optical pulses is generated by an arbitrary waveform generator (AWG). A variable optical attenuator (VOA) is used to adjust the optical power level sent to the device. Excitation of the device is performed via an optical circulator through which the device reflection and emission can be routed to two separate paths to perform either continuous wave (CW) spectroscopy or pulsed single photon counting. For CW spectroscopy, the reflected optical pump along with the optomechanically transduced signal is amplified with an erbium doped fiber amplifier (EDFA) and detected on a high-speed photodetector. On the single photon counting path, pump light is filtered using two tunable Fabry–Perot filter cavities (Stable Laser Systems, CW transmission loss of 3dB, bandwidth of 2.7MHz for the cascaded system) before directing the optical signal to the single photon detector (SPD) in the dilution fridge. **b.** Microwave pulse synthesis and detection. For measurements that require electrical excitation of the transducer, pulsed input signals to the fridge are generated at the intermediate frequency (IF) by an arbitrary waveform generator (AWG) and subsequently upconverted to ~5GHz on an IQ mixer. Likewise, for CW microwave spectroscopy, a vector network analyzer (VNA) may be switched into the setup. The microwave output from the fridge passes though a tunable bandstop filter to remove the TWPA pump tone, and is down-converted, amplified and filtered before acquisition on an analog to digital converter (ADC). For unconditional microwave readout, the master delay generator for the experiment generates the trigger signal for the ADC. For microwave readout conditioned on an optical click generated from SPDC, the trigger signal for the ADC is generated by performing a logical AND operation with a microwave switch between optical click events from the SPD and a trigger bit from the master delay generator spanning the gating window for collection of the optical signal. **c.** Dilution refrigerator configuration. The microwave (MW) input line contains attenuators on the 4K, cold, and mixing chamber plates for thermalization of the coaxial cables. The MW output line passes through an amplification chain consisting of a Traveling-Wave Parametric Amplifier (TWPA) mounted on the mixing plate and a High Electron Mobility Transistor (HEMT) amplifier mounted on the 4K plate. The TWPA is driven by a strong pump tone sent along a separate line and inserted via a directional coupler placed before the amplifier input (not shown). The superconducting nanowire single photon detector (SNSPD) is mounted to the still plate and the electrical output signal is amplified on the 4K plate before being sent to room temperature electronics.

Optical photon counting is achieved using a tungsten silicide (WSi) superconducting nanowire single photon detector (SNSPD) mounted on the still plate of the dilution refrigerator (BlueFors LD-250) maintained at a temperature of 770 mK. As shown in Fig. 8.2b, electrical pulses from the SNSPD generated by single optical photon detection events are amplified and split into two separate paths to record the detection time on a time correlated single photon counter (TCSPC) and to trigger microwave readout conditioned on an optical click. For conditional microwave readout, we first generate a logical bit for every optical click by performing a logic level translation of the SNSPD electrical pulse to a TTL signal. Using a microwave switch (Minicircuits ZASWA-2-50DRA+), we then perform a logical AND operation between this 'optical click bit' and a trigger bit provided by the master delay generator defining the duration of the optical gating window. On the other hand, unconditional microwave readout is triggered directly by the master delay generator. An RF switch (MiniCircuits ZASWA-2-50DRA+) is used to switch between unconditional and conditional readout of the microwave output signal.

The microwave output chain shown along the 'MW out' path in Fig. 8.2c begins with a Josephson traveling-wave parametric amplifier (TWPA, MIT Lincoln Labs) [80] mounted on the mixing plate as the first amplification stage. For TWPA operation, we use a CW pump tone at a frequency of ~6.07 GHz added to the amplifier input using a 20 dB directional coupler (not shown in the figure). A dual junction circulator with 40 dB isolation is placed between the directional coupler and the sample to shield the transducer from back-reflected pump. The TWPA is followed by a high mobility electron transistor (HEMT, Low Noise Factory LNF-LNC4_8C) amplifier mounted on the 4K plate. In the setup outside the fridge as shown in Fig. 8.2b, we perform additional amplification of the signal and filtering of the TWPA pump tone using a tunable notch filter (Micro Lambda Wireless MLBFR-0212). The microwave signal is then down-converted to an intermediate frequency (IF) of ~100 MHz after mixing with a local oscillator on an IQ mixer (Marki IQ-4509). The I and Q outputs of the mixer are subsequently bandpass-filtered, amplified and recorded independently on two channels of an analog to digital converter (ADC, Alazartech ATS 9360). These two digitized voltage signals correspond to measurement of the real and imaginary quadratures of the output mode of the amplification chain, $\hat{s}_{\text{out}}$. Based on the calibrated gain of our amplification chain, we measured that our heterodyne detection setup has an added noise of ~2.5 quanta referred to the output of the transducer at a signal frequency of ~5.0 GHz. This near-quantum-limited heterodyne readout enabled by the TWPA is a key enabler for measurements of

microwave-optical correlations from our transducer on a reasonable experimental timescale. The setup shown in Fig. 8.2b additionally allows for pulsed microwave excitation of the transducer as well as spectroscopy with a vector network analyzer (VNA).

The transducer sample is wire-bonded to a printed circuit board (PCB) with coaxial connectors and is housed in an oxygen-free high thermal conductivity (OFHC) copper package. The microwave resonance frequency of the NbN resonators can be tuned by an external magnetic field generated from an Nb-Ti coil mounted over the sample package. Individual devices on the chip are optically addressed using a lensed fiber (OZ Optics) affixed to the top of a three-axis piezo stepper stack (Attocube Systems) placed in line with the on-chip tapered optical couplers. The entire assembly is enclosed in a cylindrical magnetic shield and is mounted to the mixing plate of the dilution refrigerator cooled to a base temperature $T_{\mathrm{f}} \approx 20$ mK.

8.3 Optical and Microwave Spectroscopy

Our experiments are carried out by mounting the transducer chip on the mixing plate of a dilution refrigerator. We initially perform optical and microwave spectroscopy to identify the frequencies of the internal transducer modes as well as the optomechanical and piezoelectric coupling rates. For the device used in the experiments that follow, we found an optical resonance at a wavelength $\lambda = 1561.3$ nm with critical coupling to the external waveguide, $\kappa_{e,a}/2\pi = \kappa_{i,a}/2\pi = 650$ MHz. The subscripts i, e refer to linewidths due to coupling to internal and external baths, respectively. We identify the hybridized microwave-frequency electrical and acoustic modes supported by the integrated transducer-resonator system in Fig. 8.3a. In this measurement, we use a vector network analyzer (VNA) to electrically excite the microwave resonator via the microwave input port while optically pumping the optomechanical cavity of the transducer with a laser tuned to the blue side of the optical resonance. The optical pump reflected from the OMC and an optical sideband generated due to transduction of the input microwave signal are together sent to a high-speed photodetector whose output is connected to the detection port of the VNA. The magnitude of signal generated in this VNA spectrum by each of the hybridized microwave-frequency modes of the transducer-resonator system is proportional to the transduction efficiency of the corresponding mode. For the mode at a frequency of 5.001 GHz with the highest transduction efficiency and narrowest linewidth, we perform pump power dependent optomechanical spectroscopy and measure an optomechanical coupling rate, $g_{\mathrm{om}}/2\pi = 270$ kHz. We then in-

vestigate this mode and its closest neighboring resonance at 5.011 GHz with the second highest transduction efficiency. Over the frequency range shown by the gray shaded window in Fig. 8.3a, we perform microwave reflection spectroscopy of the transducer-resonator system as we sweep a magnetic field applied perpendicular to the sample. Fig. 8.3b shows the measurement result with an anti-crossing between the high transduction efficiency mode and its closest neighboring resonance, which we identify as the microwave electrical resonator mode through its characteristic quadratic tuning response in a magnetic field. The minimum frequency splitting between these two modes allows us to estimate the piezoelectric coupling rate, $g_{\mathrm{pe}}/2\pi$ = 800 kHz. The independent linewidths of the modes are measured far from the anti-crossing and are found to be $\kappa_{i,b}/2\pi$ = 150 kHz for the microwave acoustic mode and $\kappa_{e,c}/2\pi$ = 1.2 MHz, $\kappa_{i,c}/2\pi$ = 550 kHz for the microwave electrical resonator mode. For the experiments that follow, we set the external magnetic field at the value corresponding to the minimum mode splitting of $2g_{\mathrm{pe}}/2\pi$ = 1.6 MHz where both modes are maximally hybridized. This corresponds to the condition, $\omega_b = \omega_c$ in Eq. (8.1). In this setting, we define the hybridized electromechanical modes, $\hat{c}_{\pm} = (\hat{b} \pm \hat{c})/\sqrt{2}$ with frequencies, $\omega_{\pm} = \omega_c \pm g_{\mathrm{pe}}$, respectively. Even though the transducer supports other microwave-frequency acoustic modes as shown in Fig. 8.3a, these are far detuned from the modes of interest, $\hat{c}_{\pm}$, relative to the coupling rates, g_{pe} and G_{om}. As a result, we expect the Hamiltonian in Eq. (8.1) to provide a sufficiently accurate description of our system. Based on a master equation simulation of our system with the coupling rates measured above, we expect a microwave conversion efficiency, $\eta_{\mathrm{mw}} = 0.56$ into the microwave output port for a single phonon created by an SPDC event.

8.4 Spontaneous Parametric Down Conversion

We operate the transducer in SPDC mode by exciting it with optical pump pulses at the blue optomechanical sideband of the optical cavity ($\Delta_{\mathrm{a}} = (\omega_+ + \omega_-)/2$). Each pulse represents an experimental trial with a finite probability of generating a microwave-optical photon pair. In order to determine pump conditions suitable for non-classical pair generation, we performed a detailed investigation of pump-induced noise in the transducer. Our system allows for efficient microwave detection of transducer noise at levels well below a single quantum due to high microwave conversion efficiency, and the use of a near-quantum-limited Josephson traveling wave parametric amplifier (TWPA) in the readout chain. Fig. 8.5a shows a schematic of this measurement wherein microwave emission from the transducer in the output

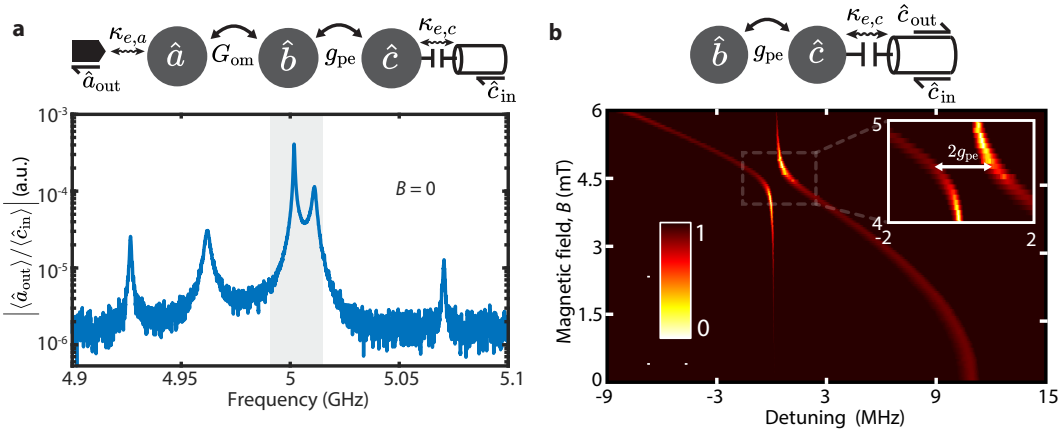

Figure 8.3: **Optical and microwave spectroscopy. a.** Continuous wave transduction spectrum measured using a vector network analyzer (VNA) at zero magnetic field. The microwave resonator is excited via the input mode, $\hat{c}_{\text{in}}$, and the optical output mode, $\hat{a}_{\text{out}}$ is electrically detected via its microwave frequency beat note with the optical pump on a high speed photodetector. Two modes of interest in the hybridized transducer-resonator system are highlighted in the gray shaded window. **b.** Microwave reflection spectrum of the highlighted modes in panel a probed as a function of external magnetic field. The horizontal axis refers to detuning from the acoustic mode at zero magnetic field. Inset shows a close-up of the anti-crossing between the tunable microwave-frequency electrical and stationary acoustic modes revealing a minimum mode splitting, $2g_{\text{pe}}/2\pi = 1.6$ MHz.

mode, $\hat{c}_{\text{out}}$ is sent to a heterodyne detection setup. Using the input-output formalism for a phase-insensitive amplifier [81, 82] in the limit $G \gg 1$, we write the output of this setup as $\hat{s}_{\text{out}} \approx \sqrt{G}(\hat{c}_{\text{out}} + \hat{h}^\dagger)$, where $\hat{h}^\dagger$ is the noise mode added by the amplifier. Emission from the transducer modes $\hat{c}_\pm$ is concentrated in a small bandwidth about the frequencies $\omega_\pm$ within $\hat{s}_{\text{out}}$. We isolate this signal by integrating the recorded heterodyne voltage signal with a matched emission envelope function $f(t)$ as detailed in Section 8.7. This corresponds to a measurement of the quadratures of the temporal mode $\hat{S}(t) := \int \hat{s}_{\text{out}}(t+t')f^*(t')dt'$ at the output of the heterodyne detection setup. Similarly, we define $\hat{C}(t) := \int \hat{c}_{\text{out}}(t+t')f^*(t')dt'$ and $\hat{H}(t) := \int \hat{h}(t+t')f^*(t')dt'$ to be temporal modes corresponding to emission referred to the output port of the transducer device and amplifier noise. The envelope function, $f(t)$ is constructed to capture emission from both hybridized modes $\hat{c}_\pm$, and consequently the temporal mode, $\hat{C}(t)$ has large spectral overlap with both of them. By measuring the heterodyne voltage signal in the presence (absence) of optical pump pulses, we collect complex-valued voltage samples of $\hat{S}$ ($\hat{H}^\dagger$). These voltage samples are then used to calculate the moments of the microwave field, $\bar{C}_{mn} = \langle \hat{C}^{\dagger m}\hat{C}^n \rangle$ by taking an ensemble average over the experimental trials and inverting the amplifier input-output relations (Section 8.6 and Ref. [83]).

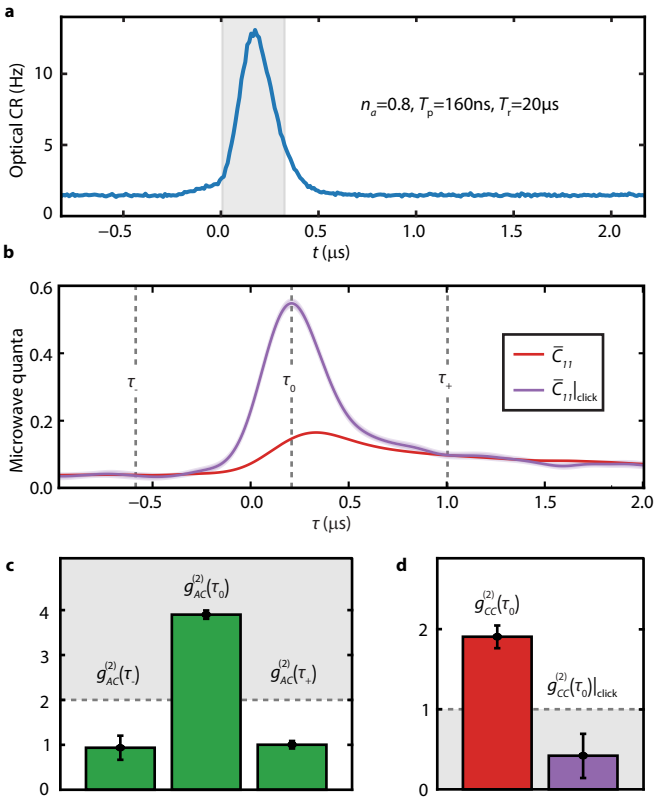

Figure 8.4: **Microwave-optical cross-correlations. a.** Time-binned histogram of optical detection events shown in the form of a time trace of optical photon count rate (CR) registered on the SPD. Shaded vertical window indicates the gating window used for heralding. Parameters for pulsed optical pumping are also indicated on the plot. **b.** Microwave quanta in the temporal mode, $\hat{C}$ at the transducer output port as a function of delay, τ the from the center of the optical gating window. Red trace corresponds to unconditional microwave readout and purple trace corresponds to microwave readout conditioned on an optical click. Shaded region about the trace indicates a confidence interval spanning two standard deviations about the mean. The conditional trace is an average over 9.1×10^4 heralding events. The unconditional trace, acquired in an interleaved manner with the conditional data, is an average over 1.4×10^7 optical pulse repetition periods. **c.** Normalized microwave-optical intensity cross-correlation function, $g^{(2)}_{AC}$ at delays τ_0, $\tau_\pm$ indicated in panel b. Height of colored bars on the plot indicates mean value and error bars on the data points indicate +/- one standard deviation determined via a bootstrapping procedure (Section8.12). These values are obtained from 9.1×10^4 conditional microwave voltage samples and 1.4×10^7 unconditional microwave voltage samples. Dashed line indicates expected classical upper bound for thermal states. **d.** Normalized second order intensity correlation function of the unconditional microwave state (red) and the microwave state conditioned an optical click (purple). Height of colored bars on the plot indicates mean value and error bars on the data points indicate +/- one standard deviation determined via a bootstrapping procedure (Section8.12). Dashed line indicates classical lower bound. These values are obtained from 9.1×10^4 conditional microwave voltage samples and 3.2×10^7 unconditional microwave voltage samples.

For $m = n = 1$, this procedure amounts to subtraction of amplifier-added noise of ~2.5 quanta, primarily determined by the TWPA, to obtain the transducer microwave output intensity. Fig. 8.5b shows an experimentally measured time trace of $\bar{C}_{11}$ versus delay, τ from the peak of the optical pump pulse. For this measurement, we used Gaussian pump pulses of two sigma duration, $T_\mathrm{p} = 160$ ns, peak power of 83 nW corresponding to peak intra-cavity optical photon occupation, $n_a = 0.8$, and a repetition rate of 50 kHz. Under these pump conditions, the SPDC scattering probability, $p = \int 4g_\mathrm{om}^2 n_a(t)dt/\kappa_a = 1.8 \times 10^{-4}$, is far below unity. As a result, the microwave output intensity recorded is nearly entirely due to pump-induced noise in the transducer. We complement this microwave measurement of pump-induced noise with an optomechanical sideband asymmetry measurement [84], which reveals an average acoustic mode occupation of 0.097 ± 0.012 over the duration of the pump pulse. Both noise measurements are found to be consistent with a heating model incorporating two pump-induced hot baths coupled to the acoustic mode, $\hat{b}$ and the electrical circuit mode, $\hat{c}$, respectively (Section 8.12). Our model indicates that the temporal shape of the noise in Fig. 8.5b is primarily determined by delayed heating of the acoustic bath after the optical pump pulse [85, 86]. By varying pump power as shown in Fig. 8.5c, we identify an operating regime where the maximum noise added by the transducer is well below the signal expected from a single phonon created by noiseless SPDC. This ideal signal level is set by the microwave conversion efficiency, shown by the gray horizontal line. From a power law fit, we find that the scaling of noise with pump power is sub-linear with an exponent of 0.58 ± 0.03. Further, from Fig. 8.5b, we observe that while most of the noise decays on the timescale of a few microseconds, a small component persists as steady state heating and contributes to finite noise level prior to the arrival of the pump pulse. We characterize this slow noise component by varying the repetition rate of the optical pulses. The data in Fig. 8.5d confirms decay of this slow component with an exponential timescale, $T_\mathrm{slow} = 33 \pm 6$ µs.

For the pump conditions in Fig. 8.5b chosen hereafter for low noise operation, optical emission in the mode, $\hat{a}_\mathrm{out}$, of the transducer is directed to a superconducting nanowire single photon detector (SNSPD) after passing through a Fabry-Perot filter setup to suppress the pump pulses reflected by the transducer. In Fig. 8.4a, we show the optical photon flux at the SNSPD obtained by histogramming detection times of single photon 'clicks' over multiple trials of the experiment. Gating optical clicks received in a time window of duration, $2T_\mathrm{p} = 320$ ns shown by the gray shaded region, we obtain a heralding probability, $p_\mathrm{click} = 2.7 \times 10^{-6}$, which

leads to an optical heralding rate, $R_{\text{click}} = 0.14\ \text{s}^{-1}$. The heralding probability is in reasonable agreement with the product of the SPDC scattering probability, $p = 1.8 \times 10^{-4}$ and the independently calibrated collection efficiency of our optical setup, $\eta_{\text{opt}} = 1.7 \times 10^{-2}$. Contributions of various components in the optical path to η_{opt} are tabulated in SI Table S4, and of finite stray counts to p_{click} are tabulated in SI Table S5. To measure microwave-optical cross-correlations, we perform conditional microwave readout by triggering the heterodyne measurement based on the occurrence of an optical click in an experimental trial. Following the same inversion process used for the unconditional microwave field in our noise spectroscopy measurements, we can obtain the moments of the microwave field conditioned on optical detection, $\bar{C}_{mn}|_{\text{click}} = \langle \hat{A}^\dagger \hat{C}^{\dagger m} \hat{C}^n \hat{A} \rangle / \langle \hat{A}^\dagger \hat{A} \rangle$. Here, $\hat{A}$ refers to the temporal mode defined by gating the optical waveguide mode, $\hat{a}_{\text{out}}$ in the time window indicated by the gray shaded region in Fig. 8.4a. The result for $m = n = 1$ is shown by the purple time trace in Fig. 8.4b. We observe that detection of an optical photon is correlated with substantially higher microwave intensity than that of the unconditional state, shown by the red trace in the same plot. The conditional signal is in good agreement with the result of a numerical simulation of our system (Section8.12). Dividing the conditional and unconditional microwave intensity traces recorded in Fig. 8.4a, we obtain the normalized microwave-optical intensity cross-correlation function,

$$g^{(2)}_{AC}(\tau) = \frac{\langle \hat{A}^\dagger \hat{C}^\dagger(\tau) \hat{C}(\tau) \hat{A} \rangle}{\langle \hat{A}^\dagger \hat{A} \rangle \langle \hat{C}^\dagger(\tau) \hat{C}(\tau) \rangle}. \tag{8.2}$$

In Fig. 8.4b, we plot this function sampled at three representative time delays as indicated by vertical dashed lines in Fig. 8.4a. τ_{o} is the delay corresponding to the maximum conditional microwave intensity, $\bar{C}_{11}|_{\text{click}}$, and $\tau_\pm = \tau_{\text{o}} \pm 800$ ns are offset from τ_{o} in opposite directions by five times the FWHM duration of the optical pump pulse. We measure $g^{(2)}_{AC}(\tau_o) = 3.90^{+0.093}_{-0.093}$, indicating strongly correlated microwave and optical emission at this time delay. The error bars for this observation and subsequent correlation functions referred to in the text are determined via a bootstrapping procedure over the dataset of heterodyne voltage samples (Section 8.12), and represent a confidence interval spanning two standard deviations about the mean. We observe that the microwave-optical correlations disappear at times well before and after the optical pump pulse as evinced by the near-unity values of $g^{(2)}_{AC}(\tau_+) = 1.00^{+0.08}_{-0.08}$ and $g^{(2)}_{AC}(\tau_-) = 0.94^{+0.27}_{-0.27}$.

The optical heralding events in our SPDC experiments have a finite noise contribution from pump-induced heating of the hybridized electromechanical modes as

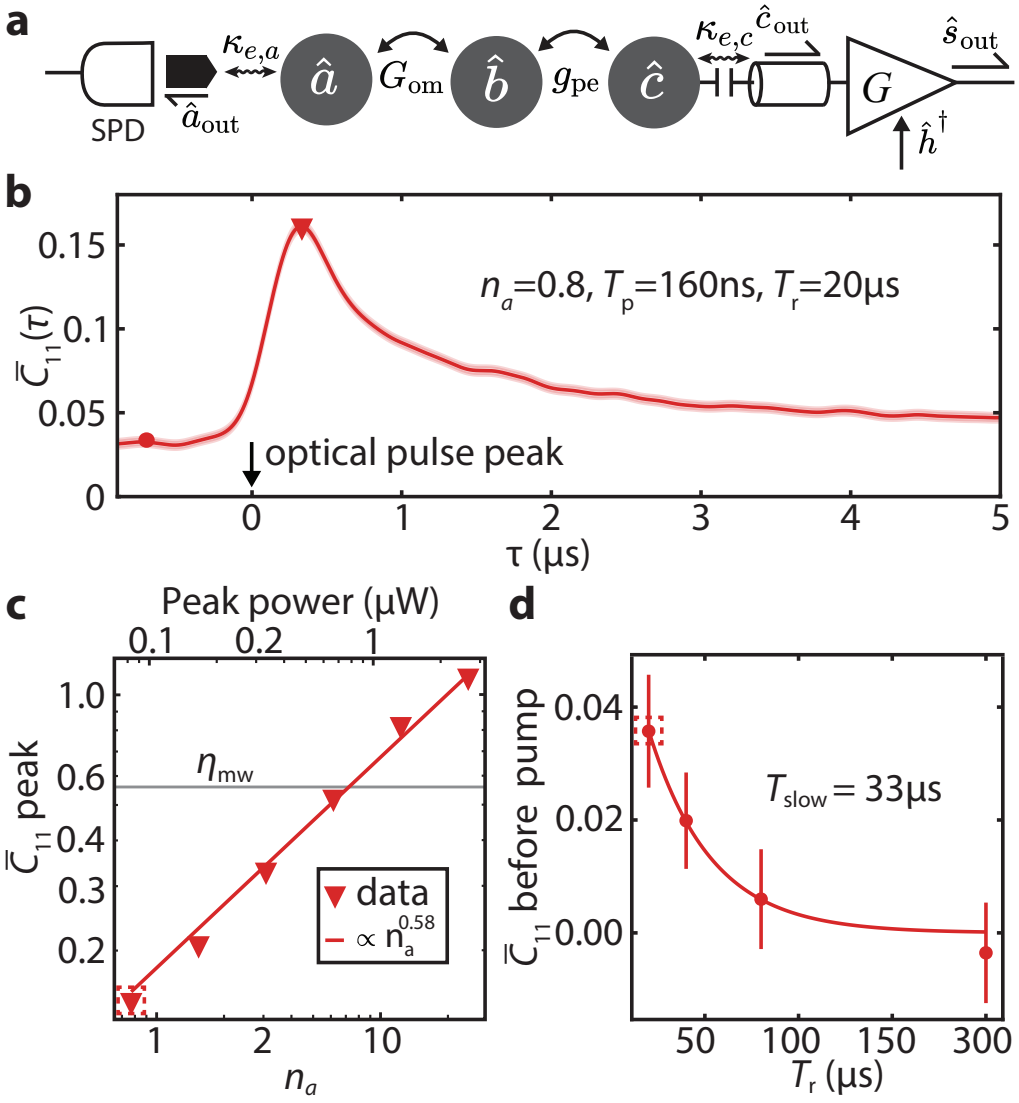

Figure 8.5: **Transducer noise characterization. a.** Mode schematic for measurements of pump-induced transducer noise. Optical emission is directed to a single photon detector (SPD) and microwave emission is directed to a heterodyne setup with gain, G and added noise, $\hat{h}^{\dagger}$. **b.** Time trace of transducer microwave output noise quanta, $\bar{C}_{11}$ under pulsed optical pumping with pump conditions indicated on the plot. Shaded region about the trace indicates a confidence interval spanning two standard deviations about the mean. Triangle marker denotes peak noise quanta, and circle marker denotes noise quanta prior to the optical pump pulse. **c.** Peak microwave output noise quanta versus peak optical power (top axis), also shown in units of peak intra-cavity optical photon occupation, n_a (bottom axis). Solid line is a power law fit revealing an exponent, 0.58 ± 0.03. Gray horizontal line indicates $\eta_{\text{mw}} = 0.56$, the microwave output quanta expected from a single phonon created by noiseless SPDC. Dashed red box shows the power used for the data in panel b. **d.** Microwave output noise quanta prior to the pump pulse versus repetition period, T_r of the pulse sequence. Error bars indicate +/- one standard deviation determined from 2×10^6 (2×10^5) voltage samples of the modes $\hat{S}$ ($\hat{H}$) as defined in the previous chapters. Solid line is an exponential fit revealing a decay time, $T_{\text{slow}} = 33 \pm 6$ µs. Dashed red box shows the repetition period used for the data in panel b.

Source of a photon click	Fraction of clicks
SPDC signal	0.727
Thermal	0.069
DCR	0.171
Pump leakage	0.033

Table 8.1: Contributions to the optical photon count rate.

well as technical sources in our experimental setup, namely detector dark counts and pump laser leakage. In Fig. 8.4a, we plot the optical photon count rate due to these noise sources as determined from independent measurements. The blue trace corresponds to the total optical signal as shown in Fig. 8.4a. Dashed lines bound the gating duration used to select photon clicks that trigger conditional microwave readout. The dark count rate (DCR) of the SNSPD in our experiment is 1.5 Hz and is limited by black-body radiation at wavelengths outside the telecom band guided through the optical fiber. Stray photon flux from laser leakage through the pump filtering setup as indicated by the purple trace in Fig. 8.4b is determined by detuning the filter cavity by 100 MHz from the acoustic mode used in the transduction experiment. To determine the noise contribution from the thermal occupation of the acoustic mode, we perform a measurement of optomechanical sideband asymmetry [84]. We excite the transducer with the same pump pulse sequence used in the SPDC experiment but with the pump laser tuned to the red mechanical sideband of the optical cavity ($\Delta_a = -(\omega_+ + \omega_-)/2$). The resultant photon flux from this measurement is shown by the red trace in Fig. 8.4a. Integrating the photon counts from these independent measurements over the gating window, we obtain the contributions of each noise source to the total probability of a heralding event, $p_{\text{click}} = 2.7 \times 10^{-6}$ as shown in Fig. 8.4b. The corresponding fractional contributions are enumerated in Tab. 8.1. Further, the difference between the count rate under red and blue detuned laser excitation allows us to infer an average thermal occupation of 0.097 ± 0.019 for the acoustic mode over the duration of the optical gating window.

8.5 Microwave-optical Cross-correlations

Following the same inversion process used for the unconditional microwave field, we can obtain the moments of the microwave field conditioned on optical detection, $\bar{C}_{mn}|_{\text{click}} = \langle \hat{A}^\dagger \hat{C}^{\dagger m} \hat{C}^n \hat{A} \rangle / \langle \hat{A}^\dagger \hat{A} \rangle$. Here, $\hat{A}$ refers to the temporal mode defined by gating the optical waveguide mode, $\hat{a}_{\text{out}}$ in the time window indicated by the gray shaded region in Fig. 8.4b. The result for $m = n = 1$ is shown by the purple time trace in Fig. 8.4c. We observe that detection of an optical photon is correlated with

substantially higher microwave intensity than that of the unconditional state. The temporal shape of the conditional signal is in good agreement with the result of a numerical simulation of our system [79].

Dividing the conditional and unconditional microwave intensity traces recorded in Fig. 8.4c, we obtain the normalized microwave-optical intensity cross-correlation function,

$$g^{(2)}_{AC}(\tau) = \frac{\langle \hat{A}^\dagger \hat{C}^\dagger(\tau)\hat{C}(\tau)\hat{A}\rangle}{\langle \hat{A}^\dagger\hat{A}\rangle\langle \hat{C}^\dagger(\tau)\hat{C}(\tau)\rangle}. \tag{8.3}$$

In Fig. 8.4d, we plot this function sampled at three representative time delays as indicated by vertical dashed lines in Fig. 8.4c. τ_o is the delay corresponding to the maximum conditional microwave intensity, $\bar{C}_{11}|_{\text{click}}$, and $\tau_\pm = \tau_o \pm 800$ ns are offset from τ_o in opposite directions by five times the FWHM duration of the optical pump pulse. We measure $g^{(2)}_{AC}(\tau_o) = 3.90^{+0.093}_{-0.093}$, indicating strongly correlated microwave and optical emission at this time delay. The error bars for this observation and subsequent correlation functions referred to in the text are determined via a bootstrapping procedure over the dataset of heterodyne voltage samples [79], and represent a confidence interval spanning two standard deviations about the mean. We observe that the microwave-optical correlations disappear at times well before and after the optical pump pulse as evinced by the near-unity values of $g^{(2)}_{AC}(\tau_+) = 1.00^{+0.08}_{-0.08}$ and $g^{(2)}_{AC}(\tau_-) = 0.94^{+0.27}_{-0.27}$.

For classical microwave-optical states, $g^{(2)}_{AC}$ is bounded by a Cauchy-Schwarz inequality, $g^{(2)}_{AC} \leq \sqrt{g^{(2)}_{AA} g^{(2)}_{CC}}$ [85, 87, 88]. Here, $g^{(2)}_{AA}$ and $g^{(2)}_{CC}$ are the normalized intensity autocorrelation functions of the unconditional optical and microwave temporal modes, $\hat{A}$ and $\hat{C}$, respectively, and are defined in a manner similar to Eq. (8.3). Using the moment inversion procedure with the unconditional microwave voltage samples, we have measured $g^{(2)}_{CC} = \bar{C}_{22}/(\bar{C}_{11})^2 = 1.91^{+0.14}_{-0.14}$ at $\tau = \tau_o$. This is consistent with the theoretically expected value of 2 for a thermal state. An explicit measurement of $g^{(2)}_{AA}$ with our current device is impractical given the low coincidence rate expected in a Hanbury-Brown-Twiss measurement. In principle, since optomechanical scattering from an acoustic mode in a thermal state is expected to produce $g^{(2)}_{AA} = 2$, we expect the classical upper bound, $g^{(2)}_{AC} \leq 2$. Our observation that $g^{(2)}_{AC}(\tau_o)$ exceeds this classical bound for thermal states by over twenty standard deviations serves as a promising signature of non-classical statistics of the microwave-optical states. In our experiment, the extent of violation of the Cauchy-Schwarz bound is primarily limited by pump-induced noise. By performing the cross-correlation experiment with increasing pump power, which is accompanied

by increasing noise, we observe that $g^{(2)}_{AC}(\tau_o)$ monotonically decreases towards the classical bound seen in Fig. 8.12.

As further evidence for the non-classical nature of the microwave-optical photon pairs, we measure the conditional microwave $g^{(2)}$ in trials with an optical click, $g^{(2)}_{CC}|_{\text{click}} = \bar{C}_{22}|_{\text{click}}/(\bar{C}_{11}|_{\text{click}})^2$. For noiseless SPDC, at low scattering probability, we expect $g^{(2)}_{CC}|_{\text{click}} = 0$ with the detection of an optical photon heralding a pure single photon in the microwave mode. In our experiment, while the value of $g^{(2)}_{CC}|_{\text{click}}$ will be higher due to pump-induced noise, a violation of the inequality, $g^{(2)}_{CC}|_{\text{click}} \geq 1$, marks a clear threshold for a non-Gaussian conditional microwave state. This violation can also be seen as a consequence of a non-classical phase space distribution for microwave and optical fields. With the conditional heterodyne voltage samples collected in our experiment, we observe $g^{(2)}_{CC}(\tau_o)|_{\text{click}} = 0.42^{+0.27}_{-0.28}$. As shown in Fig. 8.4c, this observation is below the classical bound of unity by 2.1 standard deviations. This corresponds to a probability of 1.7% for the null hypothesis of conditional preparation of a classical microwave state. The p-value is primarily limited by the sample size of our dataset with 9.1×10^4 heralding events acquired over one month. Further details of the dataset and the posterior probability distribution of $g^{(2)}_{CC}(\tau_o)|_{\text{click}}$ are provided in Section 8.12. With feasible improvements to transducer performance, which we discuss further below, more precise measurements of the conditional $g^{(2)}$ are within reach. In summary, the violation of the Cauchy-Schwarz bound by the cross-correlation function together with the observation of a non-Gaussian conditional microwave state constitute strong evidence for non-classical microwave-optical photon pairs.

8.6 Microwave Moment Inversion

To measure the statistical moments of the microwave emission from the transducer, we adopt the method originally demonstrated in Ref. [83], which has been widely applied to perform tomography of non-classical microwave radiation emitted by superconducting qubits [89–91]. The microwave signal emitted from the device undergoes a series of amplification steps before a record is captured as a digitized, complex-valued voltage signal on the heterodyne setup. This phase-insensitive amplification chain inevitably adds noise and is modelled as [82, 92],

$$\hat{s}_{\text{out}} = \sqrt{G}\hat{c}_{\text{out}} + \sqrt{G-1}\hat{h}^\dagger, \tag{8.4}$$

where $\hat{c}_{\text{out}}$, $\hat{s}_{\text{out}}$ and $\hat{h}^\dagger$ are the bosonic mode operators corresponding to the transducer output, the heterodyne setup output and added noise, respectively, with di-

mensions of $T^{-1/2}$. In the limit of large amplifier gain ($G \gg 1$), this relation may be approximated as

$$\hat{s}_{\text{out}} \approx \sqrt{G}\left(\hat{c}_{\text{out}} + \hat{h}^{\dagger}\right). \tag{8.5}$$

Once recorded, we take the inner product of the heterodyne traces with an emission envelope function, f in software. A particular choice of the envelope function corresponds to a measurement of the quadratures of the temporal mode $\hat{S}(t) := \int \hat{s}_{\text{out}}(t+t')f^*(t')dt'$. With this choice Eq. (8.5) becomes,

$$\hat{S} \approx \sqrt{G}\left(\hat{C} + \hat{H}^{\dagger}\right), \tag{8.6}$$

where $\hat{C}(t) := \int \hat{c}_{\text{out}}(t+t')f^*(t')dt'$ and $\hat{H}(t) := \int \hat{h}(t+t')f^*(t')dt'$. Note that $\hat{C}$ is a temporal mode in the output waveguide, not the internal microwave mode, $\hat{c}$ of the transducer. Thus from a sequence of N heterodyne measurements, a dataset of complex voltage samples $\{S_1, S_2, ...S_N\}$ is generated and the statistical moments are numerically calculated as [83, 92],

$$\bar{S}_{mn} := \langle \hat{S}^{\dagger m}\hat{S}^{n}\rangle = \frac{1}{N}\sum_{i=1}^{N}(S_i^*)^m(S_i)^n. \tag{8.7}$$

The results in the previous chapters require us to determine the statistical moments of $\hat{C}$, which we organize into a moments matrix with elements $\bar{C}_{mn} = \langle \hat{C}^{\dagger m}\hat{C}^{n}\rangle$. This is accomplished using additional reference measurements in which the transducer is not optically pumped so that the input to the amplifier is a vacuum state. This reference measurement directly gives the anti-normally ordered moments of the added noise as $\bar{H}_{mn} := \langle \hat{H}^{m}\hat{H}^{\dagger n}\rangle = \bar{S}_{mn}/G^{\frac{n+m}{2}}$.

We experimentally verified that $\bar{H}_{mn}$ is consistent with a thermal state for $m, n \leq 2$. Knowledge of the mean occupancy ($n_{\text{th},H}$) of the state constitutes full knowledge of the statistics for a thermal state. Accordingly, we extract $n_{\text{th},H}$ from the reference measurements and calculate $\bar{H}_{mn}$ as [93],

$$\bar{H}_{mn} = \begin{cases} m!(n_{\text{th},H}+1)^m & m = n, \\ 0 & \text{otherwise.} \end{cases} \tag{8.8}$$

Finally, under the assumption that there are no correlations between $\hat{C}$ and $\hat{H}$, Eq. (8.6) can be used to derive the following relation between the moment matrix elements [83],

$$\bar{S}_{ij} = \bar{T}_{ijmn}\bar{C}_{mn}, \tag{8.9}$$

where

$$\bar{T}_{ijmn} = \begin{cases} G^{\frac{i+j}{2}} \binom{i}{m} \binom{j}{n} \bar{H}_{i-m,j-n} & m \leq i, n \leq j, \\ 0 & \text{otherwise.} \end{cases} \tag{8.10}$$

By inverting Eq. (8.9), we recover $\bar{C}_{mn}$.

8.7 Microwave Emission Envelope Function

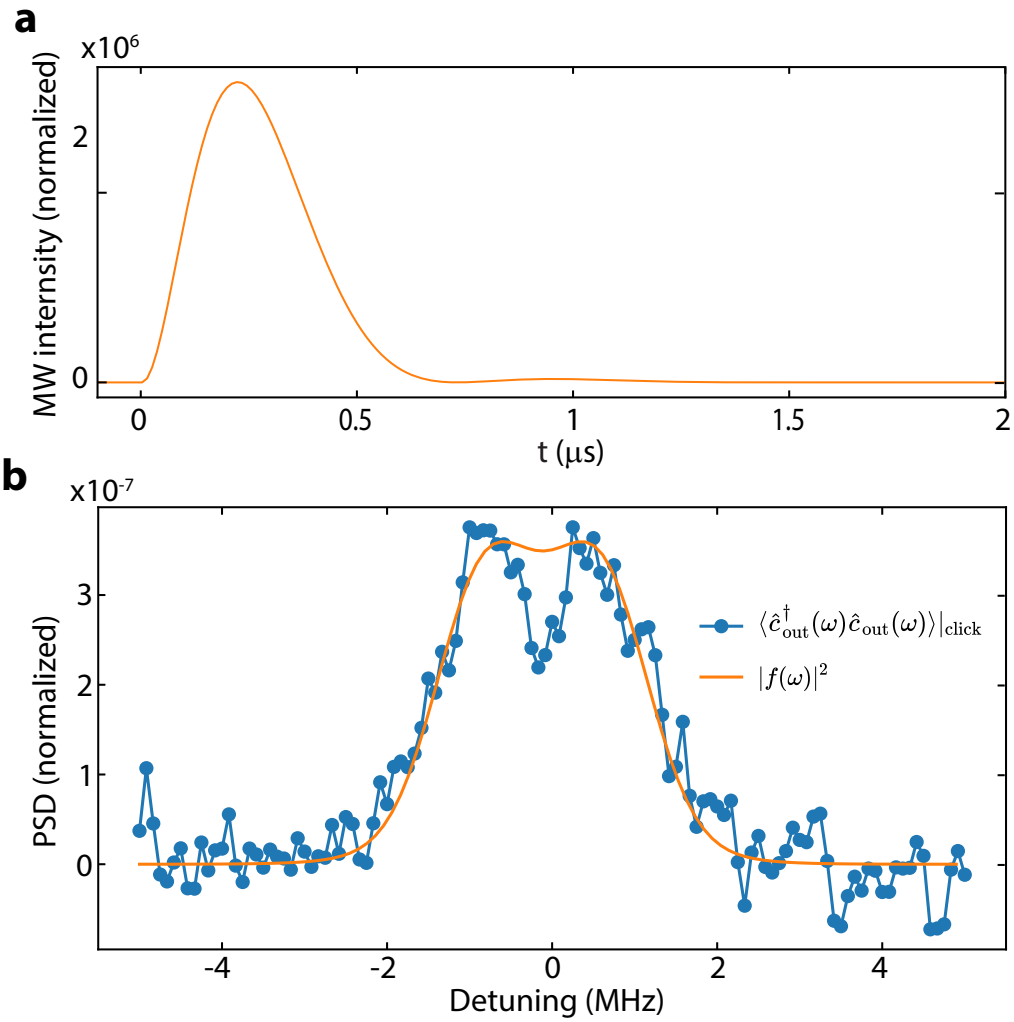

Figure 8.6: **Microwave emission envelope function. a.** Simulated temporal profile of microwave emission intensity from the transducer heralded by an optical detection event. **b.** Comparison of normalized power spectral density (PSD) of the emission envelope function, f (orange trace) and of the experimentally measured transducer microwave output conditioned on an optical click (blue data points). Detuning is defined with respect to the mean frequency of the hybridized electromechanical modes.

We define the two hybridized electro-mechanical modes in our experiment as

$$\hat{c}_{\pm} = \frac{1}{\sqrt{2}} \left(\hat{b} \pm \hat{c} \right), \tag{8.11}$$

with center frequencies $\omega_\pm = \omega_b \pm g_{\rm pe}$.

The ideal two-mode squeezed state generated under constant optical pumping on the blue optomechanical sideband ($\Delta = \omega_a - \omega_p = \omega_c$) can be written in the form [75],

$$|\psi\rangle = \left[1 + \sqrt{p}\left(\hat{a}_+^\dagger \hat{c}_+^\dagger + \hat{a}_-^\dagger \hat{c}_-^\dagger\right) + O(p)\right]|\text{vac}\rangle\,, \tag{8.12}$$

up to a normalization factor. Here p is the probability of an optomechanical scattering event, $\hat{a}_\pm$ are the optical modes which match the frequencies of the hybridized modes $\hat{c}_\pm$ as required by energy conservation. Performing single photon detection on the optical state coupled out of the cavity naturally allows us to discard the vacuum component of $|\psi\rangle$. Further, we can neglect higher order terms, $O(p)$ in the expansion since $p \ll 1$ for the optical pump power level used in our experiments. In our experiment, the SNSPD has nanosecond timing jitter, which is much smaller than the period of the beat note between the modes $\hat{a}_\pm$ given by $2\pi/2g_{\rm pe} = 625$ ns. As a result, detection of an SNSPD click in an experimental trial erases frequency information of the optical state. This measurement can be described as a projective measurement onto the state, $\left(e^{i\phi(t)/2}\hat{a}_+ + e^{-i\phi(t)/2}\hat{a}_-\right)|\text{vac}\rangle$, where the relative phase $\phi(t) = \phi_o + 2g_{\rm pe}t$ for an optical click received at time t. Here ϕ_o is the constant relative phase acquired between the two frequency bins along the optical path and t is the emission time of the photon pair defined relative to the beginning of the pump pulse. An optical click at time t can therefore be used to herald the microwave state $|\psi\rangle_{\rm click} = \left(e^{-i\phi(t)/2}\hat{c}_+^\dagger + e^{i\phi(t)/2}\hat{c}_-^\dagger\right)|\text{vac}\rangle$.

This picture becomes slightly more complicated when considering the pulsed optical drive used in this work as well as the parameters of the device. The large bandwidth of the pump pulse of 2.75 MHz in comparison to the mode splitting of 1.6 MHz means that the frequency bins cannot be individually well resolved in the optical emission. Further, given the splitting between the frequency bins versus their individual linewidths of 1.0 MHz, our device is not deep in the strong piezoelectric coupling regime. This is evinced by the two peaks with finite overlap in the experimentally measured power spectrum of the conditional microwave emission, $\langle\hat{c}_{\rm out}^\dagger(\omega)\hat{c}_{\rm out}(\omega)\rangle|_{\rm click}$ shown with the blue trace in Fig. 8.6b. However, the theoretical picture discussed above can guide the parametrization of the envelope function used for microwave readout. Accordingly, we define the microwave emission envelope function as a coherent superposition of two frequency bins centered at $\omega_\pm$,

$$f(t) = \frac{g(t)}{\sqrt{2}}\left(e^{-i(\omega_+ t + \phi_o/2)} + e^{-i(\omega_- t - \phi_o/2)}\right). \tag{8.13}$$

The relative phase, ϕ_o is assumed to be fixed since the optical pulse duration used in our experiment is short compared to the beat period between the frequency bins. The function, $g(t)$ accounts for the finite linewidth of the frequency bins and is obtained by numerically solving the master equation for our system using the QuTiP software package [94]. For this calculation, we use the Hamiltonian in 8.1 along with experimentally determined coupling and decay rates for the transducer modes. The resulting MW emission intensity is shown in Fig. 8.6a. $g(t)$ is parameterized as a skewed Gaussian to capture the faster timescale of the rising edge relative to the decay. The corresponding voltage envelope is given by the square root of a skewed Gaussian and is written as

$$g(t) = \frac{1}{\sqrt[4]{2\pi T_{\mathrm{g}}^2}} \exp\left(-\frac{t^2}{4T_{\mathrm{g}}^2}\right)\left[1 + \mathrm{erf}\left(\frac{\alpha t}{\sqrt{2}T_{\mathrm{g}}}\right)\right]^{1/2}, \tag{8.14}$$

up to a normalization factor involving the gain of the microwave amplification chain. Here the Gaussian standard deviation, $T_{\mathrm{g}} = 230$ ns and skew factor, $\alpha = 2.0$ are obtained from fitting to the simulated result. We note that for a microwave photon instantaneously loaded into the resonator, $g(t)$ is expected to follow an exponential decay. However, in our transducer, due to the finite conversion rate of the phonon from SPDC into a microwave photon, $g(t)$ has a finite rise time. As a result, we find that choosing the skewed Gaussian parametrization instead of an exponential decay provides $\sim 4\%$ higher overlap between the emission envelope function and the simulated wavepacket as quantified by their normalized inner product. The power spectrum of the resultant envelope function, $|f(\omega)|^2$ is shown as the orange trace in Fig. 8.6b. This is observed to be well-matched to the power spectrum of the conditional microwave emission from the transducer obtained from experimentally recorded heterodyne voltage traces.

8.8 Microwave Gain Calibration

We calibrate the gain of our microwave heterodyne detection setup by operating the transducer as a frequency converter with the optical pump laser on the red mechanical sideband. The calibration procedure is performed at zero magnetic field, when the acoustic and microwave modes, $\hat{b}, \hat{c}$ are detuned by a frequency separation, $\omega_b - \omega_c = 2\pi \times 12$ MHz $\gg 2g_{\mathrm{pe}}$ and are weakly hybridized. An independent measurement of optomechanical sideband asymmetry provides a meter for phonon occupation in the acoustic mode, $\hat{b}$ via the single phonon count rate, R_o [84]. We then resonantly excite the acoustic mode via the microwave port and

measure the transduced optical photon count rate, R. Simultaneously, we record the reflected microwave signal from the transducer, which produces an output power, P_{det} at the output of the heterodyne setup. The gain, G of the amplification chain can be determined using the series of equations below.

$$R = n_{b,\mathrm{sig}} R_o, \tag{8.15}$$

$$n_{b,\mathrm{sig}} \hbar \omega_b = P_{\mathrm{in}} \frac{4\kappa_{e,b}}{\kappa_{i,b}^2}, \tag{8.16}$$

$$P_{\mathrm{det}} = G \left(\frac{\kappa_{e,b} - \kappa_{i,b}}{\kappa_{e,b} + \kappa_{i,b}} \right)^2 P_{\mathrm{in}}. \tag{8.17}$$

Here, $n_{b,\mathrm{sig}}$ is the occupation of the acoustic mode due to the microwave drive obtained after subtracting the thermal component of the transduced signal. P_{in} is the input microwave power to the transducer. $\kappa_{b,\mathrm{e}}$ is the coupling rate of the acoustic mode to the microwave waveguide due to weak hybridization with the microwave resonator and $\kappa_{b,\mathrm{i}}$ is the intrinsic linewidth of the acoustic mode. Both rates are determined via a VNA measurement of the acoustic mode in the presence of the optical pump pulses. Following this procedure, we estimate gain, $G = 103$ dB between the microwave output port of the transducer and the output of the heterodyne setup. While knowledge of the gain allows us to estimate the microwave intensity at the transducer output, we note that the values of the normalized correlation functions measured in our experiment are independent of the absolute accuracy of this calibration.

8.9 TWPA Optimization

The operating point of the TWPA was optimized prior to data acquisition. In order to ensure fast acquisition and unbiased statistics, our operational criterion were (1) maximize the gain and (2) ensure linearity in the response. In our optimization procedure, the frequency and power of the pump tone driving the TWPA were swept, and coherent pulses with amplitude matched to the conditional microwave signal in our experiment were sent to the transducer input port. The result of the heterodyne measurement of the reflected signal from the transducer was used to compute $g_{CC}^{(2)}$. To ensure linearity, we chose a region in the TWPA pump frequency and power space where $g_{CC}^{(2)} = 1$ to within one standard deviation. The final operating point was then chosen as the one with maximum gain from this cohort. Over the course of the experiment, linearity of the TWPA was periodically verified by measuring $g_{CC}^{(2)}$

for a weak coherent input. In case of a deviation of $g^{(2)}_{CC}$ from unity by one standard deviation, the experiment was halted and the pump optimization routine was re-run.

8.10 Transducer Heating Dynamics

To investigate the heating dynamics of the transducer, we performed a series of microwave measurements under pulsed optical excitation. In Fig. 8.7a, we show the time-resolved power spectrum of the unconditional microwave emission at the transducer output port. For this measurement, we use the optical pulse sequence (T_p = 160 ns, 50 kHz repetition rate) used in the SPDC experiments in the previous chapters albeit at a higher pump power, n_a = 12, which generates higher thermal noise. We observe that majority of the heating occurs in the emission bandwidth of the hybridized electro-mechanical modes. The peak of this thermal emission is noticeably delayed from the optical pump pulse. Additionally, we observe a small but non-zero noise contribution far from the transducer resonances, which we attribute to heating of the microwave waveguide. These resonator and waveguide contributions to the added noise are separated by fitting the power spectrum at each delay to a double Lorentzian function with a constant floor. The fit result is shown in Fig. 8.7b, and indicates that resonator heating significantly dominates waveguide heating and has a stronger time dependence. This points to parasitic optical absorption in the intrinsic baths of the acoustic and microwave modes as the dominant source of transducer heating. Additionally, we measured the scaling of the intensity of this thermal emission with optical pump power and observed it to be sub-linear as shown by the results plotted in Fig. 8.7c. Finally, from the time dynamics of heating in Fig. 8.7a, we observe that while most of the thermal emission decays on the timescale of a few microseconds, a small component persists as steady state heating and is observed prior to the arrival of the optical pump pulse. We attribute this to a slower component of the hot bath generated by optical absorption and characterize it by varying the repetition rate of the optical pulses. The result shown in Fig. 8.7d confirms slow decay of this component of heating with an exponential decay time of $33 \pm 6 \mu$s. The measurements described in this section were performed on the same device used for the SPDC experiments in the previous chapters, but after a partial warm up and cooldown to base temperature. After this thermal cycle, we observed frequency shifts of the microwave and acoustic modes by a few MHz and an increase in the normal mode splitting. However, the thermal noise quanta generated by the optical pulse sequence used for the experiments in the previous chapters remained nearly the same.

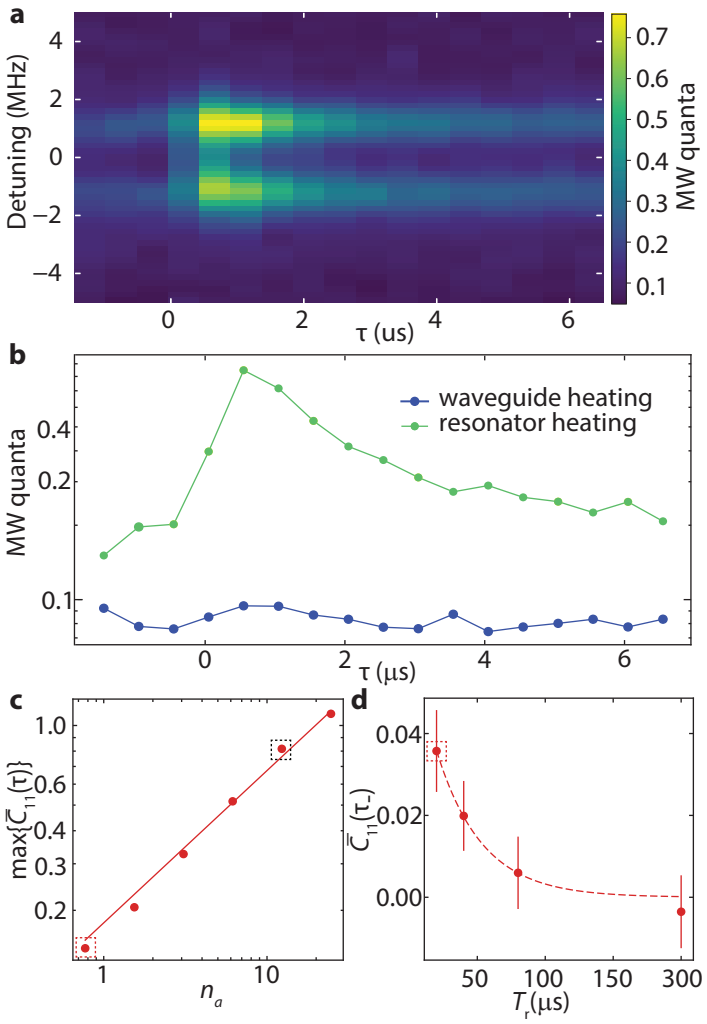

Figure 8.7: **Transducer heating dynamics. a.** Power spectral density of the unconditional microwave signal as a function of delay, τ from the center of the optical pump pulse. Detuning is defined with respect to the mean frequency of the hybridized electromechanical modes. Legend indicates microwave quanta emitted at the output port in a 100 kHz bandwidth. Measurement is performed with optical pump pulses of peak power, n_a = 12, pulse duration of 160 ns, and 50 kHz repetition rate. **b.** Time dependence of waveguide and resonator components of heating extracted by fitting the data in panel **a.**. **c.** Thermal emission in the transducer microwave output as a function of optical pump power. Pump power is plotted in terms of peak intra-cavity occupation of the optical mode, n_a and microwave intensity is plotted in terms of occupation of the temporal mode, $\bar{C}_{11}$ measured at the delay, τ at which it is maximized. All measurements were performed with the 160 ns pulse duration and 50 kHz repetition rate used for data in the previous chapters. Dashed red box denotes the power used for the experiment in the previous chapters (n_a = 0.8) while the dashed black box denotes the power used for measurements in panels **a,b**. Solid line is a power law fit revealing an exponent, 0.58 ± 0.03. **d.** Decay of the slow component of the thermal emission probed by varying the repetition period, T_r of the pump pulse sequence. Microwave quanta in the unconditional state, $\bar{C}_{11}$ are measured versus prior to the pump pulse at the delay τ_- as defined in the previous chapters. Dashed line is an exponential fit revealing a decay time of 33 ± 6 μs. Dashed red box denotes the repetition rate used for the experiment in the previous chapters.

8.11 Simulation of the Conditional Microwave State

As detailed in 8.1, the dynamics of the transducer are governed by the Hamiltonian,

$$\hat{H}_{abc}(t) = \hat{H}_o + \hat{H}_{\mathrm{om}}(t) + \hat{H}_{\mathrm{pe}}, \tag{8.18}$$

where $\hat{H}_o$, $\hat{H}_{\mathrm{om}}(t)$, and $\hat{H}_{\mathrm{pe}}$ contain the mode frequencies, optomechanical interaction, and piezoelectric interaction terms, respectively. These are defined as

$$\hat{H}_o = -\hbar\Delta_a \hat{a}^\dagger \hat{a} + \hbar\omega_b \hat{b}^\dagger \hat{b} + \hbar\omega_c \hat{c}^\dagger \hat{c}, \tag{8.19a}$$

$$\hat{H}_{\mathrm{om}}(t) = \hbar G_{\mathrm{om}}(t)(\hat{a}^\dagger \hat{b}^\dagger + \hat{a}\hat{b}), \tag{8.19b}$$

$$\hat{H}_{\mathrm{pe}} = \hbar g_{\mathrm{pe}}(\hat{b}^\dagger \hat{c} + \hat{b}\hat{c}^\dagger). \tag{8.19c}$$

We have explicitly included the time dependence of the optomechanical coupling $G_{\mathrm{om}}(t) = \sqrt{n_a(t)} g_{\mathrm{om}}$ due to the temporal shape of the intra-cavity pump photon number, $n_a(t) = \kappa_{\mathrm{e},a}/(\Delta_a^2 + \kappa_a^2/4) P_{\mathrm{in}}(t)$. $P_{\mathrm{in}}(t)$, the optical pump power at the device follows a Gaussian shape with parameters described in the previous chapters. In our experiment, we use a blue detuned pump with $\Delta_a = \omega_b$. Further, our device is in the sideband resolved regime with $\omega_b \gg \kappa_a$.

In addition to unitary evolution due to couplings among the internal modes of the transducer, the system is also subject to dissipation and heating due to coupling to the environment. This is captured by the master equation,

$$\dot{\hat{\rho}}(t) = \mathcal{L}(t)\hat{\rho}(t). \tag{8.20}$$

Defining the Lindblad superoperator as $\mathcal{D}(\hat{o})\hat{\rho} = \hat{o}\hat{\rho}\hat{o}^\dagger - \frac{1}{2}\left\{\hat{o}^\dagger \hat{o}, \hat{\rho}\right\}$ the action of $\mathcal{L}(t)$ on the density matrix is written as

$$\mathcal{L}(t)\hat{\rho}(t) = -\frac{i}{\hbar}\left[\hat{H}_{abc}, \hat{\rho}(t)\right] + \left(\mathcal{L}_a + \mathcal{L}_b(t) + \mathcal{L}_c(t)\right)\hat{\rho}(t), \tag{8.21}$$

where the superoperators, $\mathcal{L}_a, \mathcal{L}_b, \mathcal{L}_c$ describe the coupling of the respective transducer modes to the environment according to the relations below.

$$\mathcal{L}_a\hat{\rho}(t) = \kappa_a \mathcal{D}(\hat{a})\hat{\rho}(t), \tag{8.22a}$$

$$\begin{aligned}\mathcal{L}_b(t)\hat{\rho}(t) = {} & n_{\mathrm{th},b}(t)\kappa_{\mathrm{i},b}\mathcal{D}(\hat{b}^\dagger)\hat{\rho}(t) \\ & + \left[n_{\mathrm{th,b}}(t) + 1\right]\kappa_{i,b}\mathcal{D}(\hat{b})\hat{\rho}(t),\end{aligned} \tag{8.22b}$$

$$\begin{aligned}\mathcal{L}_c(t)\hat{\rho}(t) = {} & n_{\mathrm{th},c}(t)\kappa_{\mathrm{i},c}\mathcal{D}(\hat{c}^\dagger)\hat{\rho}(t) \\ & + \left[n_{\mathrm{th},c}(t) + 1\right]\kappa_{i,c}\mathcal{D}(\hat{c})\hat{\rho}(t) \\ & + n_{\mathrm{th},w}\kappa_{\mathrm{e},c}\mathcal{D}(\hat{c}^\dagger)\hat{\rho}(t) \\ & + \left[n_{\mathrm{th},w} + 1\right]\kappa_{e,c}\mathcal{D}(\hat{c})\hat{\rho}(t).\end{aligned} \tag{8.22c}$$

Here the total dissipation rate of the optical mode, $\kappa_a = \kappa_{e,a}+\kappa_{i,a}$. To capture heating of the transducer modes due to parasitic absorption of the optical pump, we assume that the acoustic and microwave modes are coupled to intrinsic baths with time dependent thermal occupation, $n_{\mathrm{th},b}(t)$ and $n_{\mathrm{th},c}(t)$, respectively. $n_{\mathrm{th},w}$, the thermal occupation of the microwave waveguide is set to a constant value much smaller than $n_{\mathrm{th},b}(t)$ and $n_{\mathrm{th},c}(t)$ based on the measurements detailed in Section 11. We note that while these baths may be significantly more complex and involve several components possessing different, time-dependent coupling strengths, our model is aimed at capturing the total influx of thermal excitations into the transducer modes generated by the optical pulse. With this endeavor in mind, we assume that the acoustic (microwave) mode couples to a single intrinsic bath at a fixed dissipation rate, $\kappa_{i,b}$ ($\kappa_{i,c}$) and ascribe the time-dependence of the heating dynamics entirely to the thermal occupation of the bath. This phenomenological approach to heating induced by optical absorption has previously been used to model photon correlations in optomechanics experiments [95].

While Eq. (8.20) can be numerically solved in principle, this is computationally intensive owing to the large state space involving the three modes of the transducer. Instead, we take advantage of the fact that $\kappa_a \gg G_{\mathrm{om}}$ to adiabatically eliminate the optical mode [96]. Moving into a frame rotating with the mechanical and microwave modes and defining the optomechanical scattering rate, $\Gamma_{\mathrm{om}}(t) = 4|G_{\mathrm{om}}(t)|^2/\kappa_a$, we arrive at the simplified master equation,

$$\dot{\hat{\rho}}_r(t) = \mathcal{L}_r(t)\hat{\rho}_r(t), \tag{8.23}$$

where $\hat{\rho}_r = \mathrm{Tr}_a\{\hat{\rho}\}$ denotes the reduced density matrix spanning only the acoustic and microwave modes. $\mathcal{L}_r$ is defined by its action on the reduced density matrix,

$$\begin{aligned}\mathcal{L}_r(t)\hat{\rho}_r(t) = &-\frac{i}{\hbar}\left[\hat{H}_{\mathrm{pe}}, \hat{\rho}_r(t)\right] \\ &+ \left(\mathcal{L}_{\mathrm{om}}(t) + \mathcal{L}_b(t) + \mathcal{L}_c(t)\right)\hat{\rho}_r(t),\end{aligned} \tag{8.24}$$

where we have introduced optomechanical scattering as a coupling of the reduced system to an effective bath according to the relation,

$$\mathcal{L}_{\mathrm{om}}(t)\hat{\rho}_r(t) = \Gamma_{\mathrm{om}}(t)\mathcal{D}(\hat{b}^\dagger)\hat{\rho}_r(t). \tag{8.25}$$

The Lindblad superoperator, $\mathcal{D}(\hat{b}^\dagger)$ contains a non-number preserving quantum jump operator which adds a phonon to the system due to optomechanical SPDC.

This process is naturally correlated with the creation of an optical photon, which is routed with finite collection efficiency to a single photon detector. Given that optical decay ($\kappa_a/2\pi = 1.3$ GHz) occurs on a much faster timescale than the dynamics of the rest of the system ($\kappa_a \gg \kappa_b, g_{\mathrm{pe}}, \kappa_c$), optical detection is assumed to be instantaneous. Under this approximation, in the event of a click on the optical detector caused by a quantum jump at time t_J, the resultant conditional state of the reduced system is,

$$\hat{\rho}_\mathrm{J}(t_\mathrm{J}) = \frac{\hat{b}^\dagger \hat{\rho}_r(t_\mathrm{J}) \hat{b}}{\mathrm{Tr}\left\{\hat{b}^\dagger \hat{\rho}_r(t_\mathrm{J}) \hat{b}\right\}}. \tag{8.26}$$

This state then evolves according to Eq. (8.23). Since we operate in the weak pump regime where the integrated jump probability over the optical pulse duration, $\int \Gamma_{\mathrm{om}}(t)dt \ll 1$, we neglect two-fold SPDC events.

While the treatment above describes the evolution of the internal modes of the transducer, we experimentally measure the emission in the temporal mode, $\hat{C}$ in the transducer microwave output port. This temporal mode is linearly related to the internal microwave mode of the transducer as $\hat{C}(t) := \int \hat{c}_{\mathrm{out}}(t+t')f^*(t')dt' = \sqrt{\kappa_{e,c}} \int \hat{c}(t+t')f^*(t')dt'$. We can thus compute the occupation of the temporal mode as

$$\begin{aligned}
& \langle \hat{C}^\dagger(t)\hat{C}(t)\rangle \\
= \; & \kappa_{e,c} \langle \int \hat{c}^\dagger(t+t'')f(t'')dt'' \int \hat{c}(t+t')f^*(t')dt' \rangle \\
= \; & \kappa_{e,c} \int \langle \hat{c}^\dagger(t+t'')\hat{c}(t+t')\rangle f(t'')f^*(t')dt''dt' \\
= \; & \kappa_{e,c} \int \langle \hat{c}^\dagger(t'+\tau')\hat{c}(t')\rangle f(t'+\tau'-t)f^*(t'-t)dt'd\tau',
\end{aligned} \tag{8.27}$$

where the correlator, $\langle \hat{c}^\dagger(t'+\tau')\hat{c}(t')\rangle$ inside the integral on the final line can be numerically computed using the quantum regression theorem [97]. Further, to model the conditional state due to a quantum jump at time t_J, this correlator is computed using $\hat{\rho}_\mathrm{J}(t_\mathrm{J})$ in Eq. (8.26) for times, $t > t_\mathrm{J}$. For times $t < t_\mathrm{J}$, we use the value for the unconditional state. Performing this calculation for a sequence of jump times, $\{t_\mathrm{J}\}$ associated with detector clicks received within the optical gating window, we obtain a sequence of conditional time traces for the occupation of the temporal mode, $\{\langle \hat{C}^\dagger \hat{C}\rangle|_{t_\mathrm{J}}\}$. The final conditional trace, $\langle \hat{C}^\dagger \hat{C}\rangle|_{\mathrm{click}}$ is given by a weighted average over this sequence with weights determined by the infinitesimal jump probability, $\delta p_\mathrm{J} \propto \Gamma_{\mathrm{om}}(t_\mathrm{J})dt$ in an interval dt at time t_J. The effects of detector

dark counts as well as the optical pump filter in our experiment are incorporated via appropriate modifications to these weights.

We perform a numerical simulation of our system by implementing the above model using the QuTiP software package [94]. Solutions to the master equation as well as the required correlators are evaluated in a 10×10 Fock space of the acoustic and microwave modes. To incorporate effects of heating of the microwave and acoustic baths separately in our model, we measured the unconditional microwave emission from the transducer in response to optical pump pulses under two conditions (i) mechanics far detuned from the microwave mode, $\omega_c - \omega_b \gg 2g_{\mathrm{pe}}$, (ii) mechanics on resonance with the microwave mode, $\omega_b = \omega_c$. The results of the measurement are shown with the dotted traces in Fig. 8.8d. Under condition (i), which is achieved at zero magnetic field, the microwave emission is approximately entirely due to heating of the microwave bath alone. On the other hand, condition (ii) corresponds to maximal electro-mechanical hybridization and is relevant to the SPDC experiments described in the previous chapters. In this setting, heating of both microwave and acoustic baths is expected to contribute to the measured microwave output signal. Using measurements of the microwave emission under both conditions, we invert the master equation to determine $n_{\mathrm{th,b}}(t)$ and $n_{\mathrm{th,c}}(t)$ approximated as a piece-wise linear function over coarse samples as shown in Fig. 8.8b. The inversion is performed by choosing an ansatz for $n_{\mathrm{th,b}}(t)$ and $n_{\mathrm{th,c}}(t)$, iteratively solving the master equation and performing least mean square optimization with respect to the experimentally measured thermal microwave emission. The resulting occupations of the acoustic mode, $\hat{b}$ and of the unconditional temporal microwave mode, $\hat{C}$ obtained by solving the master equation are shown in Fig. 8.8c and with the solid traces in Fig. 8.8d, respectively. While the model for the hot baths is determined entirely using microwave measurements, we observe that the simulated occupation of the acoustic mode is in reasonable agreement with an experimental measurement shown by the gray data point in Fig. 8.8c. This data point corresponds to the optomechanical sideband asymmetry measurement described in Section 6, and represents the thermal occupation of the acoustic mode averaged over the duration of the optical pump pulse. Finally, the conditional microwave emission determined using our model shown with the solid purple trace in Fig. 8.9 is in good agreement with the corresponding experimental result shown via the dotted purple trace. The simulated conditional and unconditional intensity traces plotted in this figure predict a value of $g^{(2)}_{AC}(\tau_o) = 3.97$, which is in good agreement with the experimentally observed value of 3.90.

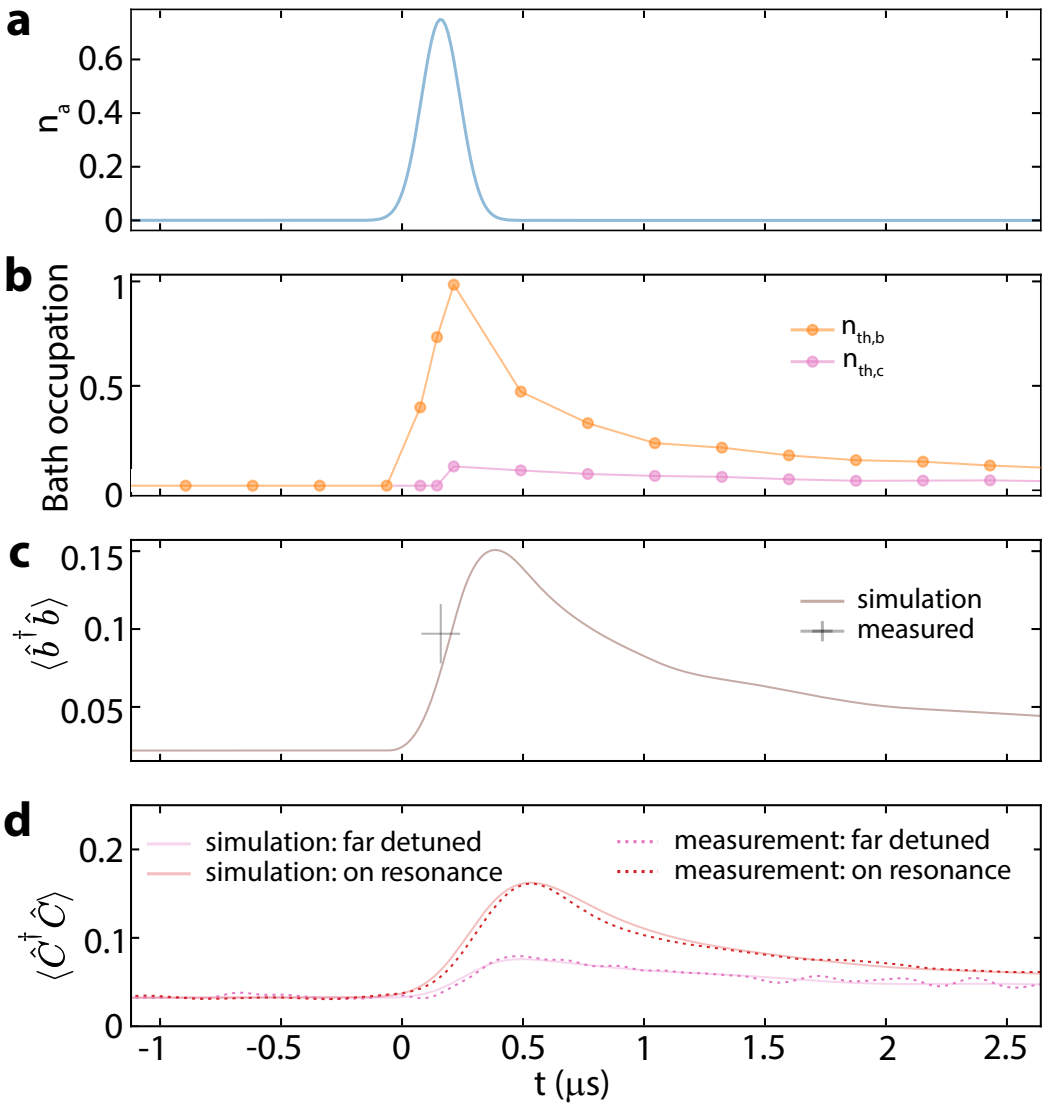

Figure 8.8: **Simulation of transducer heating dynamics. a.** Time trace of the optical pump pulse plotted in terms of the intra-cavity occupation of the optical mode, n_a. **b.** Model used for time dependent thermal occupation of the intrinsic baths of the acoustic and microwave modes, $n_{\mathrm{th},b}(t)$, $n_{\mathrm{th},c}(t)$. **c.** Time dependent occupation of the acoustic mode, $\langle \hat{b}^\dagger \hat{b} \rangle$ obtained from the master equation simulation. Gray data point corresponds to experimentally recorded thermal occupation of the acoustic mode as inferred from an optomechanical sideband asymmetry measurement. The vertical bar on the point represents a confidence interval spanning two standard deviations while the horizontal bar indicates the FWHM duration of the optical pulse. **c.** Time dependent occupation of the temporal mode, $\langle \hat{C}^\dagger \hat{C} \rangle$ in the microwave output port of the transducer from the master equation simulation (solid traces) and from experimental heterodyne data (dotted traces). The condition where the acoustic mode is far detuned (on resonance) with respect to the microwave mode is shown with pink (red) traces.

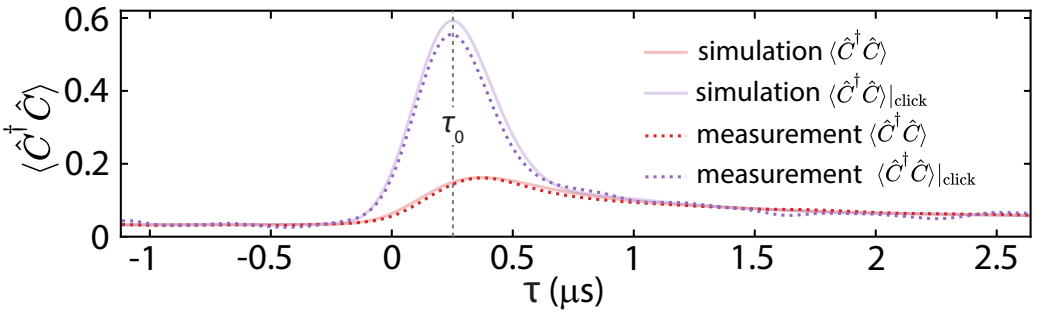

Figure 8.9: **Simulation of the conditional microwave state.** Occupation of the temporal mode, $\hat{C}$ in the microwave output port of the transducer from simulation (solid traces) and from experimental heterodyne data (dotted traces). The occupation of the microwave state conditioned on an optical click, $\langle \hat{C}^\dagger \hat{C} \rangle|_{\text{click}}$ is shown with purple traces. The occupation of the unconditional microwave state, $\langle \hat{C}^\dagger \hat{C} \rangle$ is shown with red traces for comparison.

Simulation of $g^{(2)}_{CC}|_{\text{click}}$ requires evaluation of $\langle \hat{C}^{\dagger 2} \hat{C}^2 \rangle|_{\text{click}}$. Extending the approach of Eq. (8.27) to the second order moment is a nontrivial computational endeavor as it requires calculation of the four-time correlator, $\langle \hat{c}^\dagger(t+t'''')\hat{c}^\dagger(t+t''')\hat{c}(t+t'')\hat{c}(t+t')\rangle$. For the purpose of this work, we pursue the more tractable task of placing bounds on $g^{(2)}_{CC}|_{\text{click}}$. First, we consider the conditional state of the acoustic mode immediately after the addition of a phonon as triggered by an SPDC event. Since the extraction of this acoustic state into the microwave output port is accompanied by loss and addition of noise, we expect the function, $g^{(2)}_{bb}|_{\text{click}} = \langle \hat{b}^{\dagger 2} b^2 \rangle|_{\text{click}} / (\langle \hat{b}^\dagger b \rangle|_{\text{click}})^2$ to provide a lower bound for $g^{(2)}_{CC}|_{\text{click}}$. Our model estimates $g^{(2)}_{bb}|_{\text{click}}(0) = 0.24$. Next, we consider a choice of the emission envelope function, $f(t) = \delta(t - T_o - \tau_o)$, where T_o is the time corresponding to the peak intensity of the pump pulse. Physically, employing this function results in collecting the microwave emission at all frequencies from the transducer at a fixed time. This is strictly less optimal than the choice in our measurements, namely a function coherently matched to the theoretically expected single photon wavepacket as discussed in Sec. 8.7. In the event of this sub-optimal choice, moments of the temporal mode, $\hat{C}$ are proportional to the corresponding moments of the internal microwave mode, $\hat{c}$ and the function, $g^{(2)}_{cc}|_{\text{click}} = \langle \hat{c}^{\dagger 2} c^2 \rangle|_{\text{click}} / (\langle \hat{c}^\dagger c \rangle|_{\text{click}})^2$, serves as an upper bound for $g^{(2)}_{CC}|_{\text{click}}$. Our model estimates $g^{(2)}_{cc}|_{\text{click}}(\tau_o) = 0.77$. In summary, the above arguments allow us to use numerical simulations to bound $g^{(2)}_{CC}|_{\text{click}}(\tau_o)$ to the interval $(0.24, 0.77)$, which has substantial overlap with the experimental observation of $g^{(2)}_{CC}|_{\text{click}}(\tau_o) = 0.42^{+0.27}_{-0.28}$.

8.12 Data Analysis for Correlation Functions

For measurements of $g^{(2)}_{AC}$ and $g^{(2)}_{CC}|_{\text{click}}$ presented in 8.4, 9.1×10^4 heterodyne voltage traces were acquired over a one month period. For every ~16 minutes of acquisition of conditional microwave data, we interleaved the acquisition of voltage samples of amplifier noise and the unconditional microwave signal. The unconditional microwave intensity signal, $\bar{C}_{11}(\tau)$ used to evaluate the normalized cross-correlation function, $g^{(2)}_{AC}$ was obtained from 1.4×10^7 heterodyne voltage traces. Likewise, the measurement of the normalized second order intensity correlation function, $g^{(2)}_{CC}(\tau_o)$ used 3.2×10^7 heterodyne voltage samples.

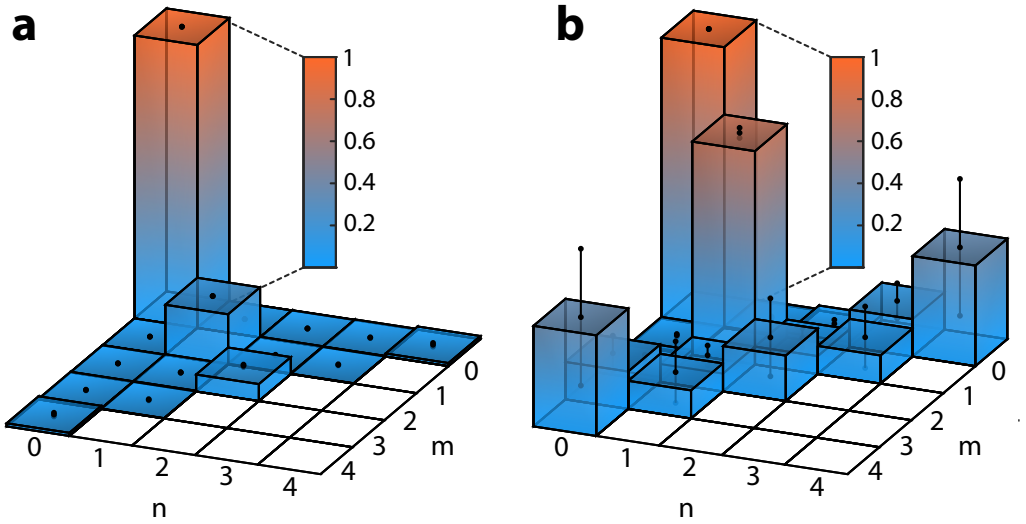

Figure 8.10: **Microwave moments. a.** Moments matrix for the unconditional microwave output of the transducer, $\bar{C}_{mn}$. **b.** Moments matrix for the microwave output of the transducer conditioned on receipt of an optical click, $\bar{C}_{mn}|_{\text{click}}$. Error bars calculated via bootstrapping with replacement are indicated by the black pins.

To minimize the effect of long term fluctuations in the added noise and gain of the TWPA, we divide the dataset into chunks corresponding to acquisition over one day, and invert each separately to extract the moments $\bar{C}^{(k)}_{mn}$, $\bar{C}^{(k)}_{mn}|_{\text{click}}$, where the index k runs over the daily chunks. This inversion process follows the methods detailed in Sec. 8.6 and assumes that no correlations exist between $\hat{H}$ and $\hat{A}$ as well as $\hat{H}$ and $\hat{C}$. We then take a weighted average to compute the entries of the moments matrix, $\bar{C}_{mn} = \sum_k w^{(k)}\bar{C}^{(k)}_{mn}$ and $\bar{C}_{mn}|_{\text{click}} = \sum_k w^{(k)}_{\text{click}}\bar{C}^{(k)}_{mn}|_{\text{click}}$, where $w^{(k)}$, $w^{(k)}_{\text{click}}$ denote the fraction of records in the k^{th} chunk of the unconditional and conditional datasets, respectively. The moments matrices constructed from this process are shown in Fig. 8.10b.

The acquisition rate for the moments of the conditional heterodyne output, $\bar{S}_{\text{mn}}|_{\text{click}}$

is determined by the optical heralding rate, $R_{\text{click}} = 0.14$ Hz. This is much slower compared to that for the amplifier noise moments, $\bar{H}_{\text{mn}}$, which can be acquired at the 50 kHz repetition rate of the experiment and determined with high accuracy. As a result, the error in $g^{(2)}_{CC}|_{\text{click}}$ is dominated by uncertainty in $\bar{S}_{\text{mn}}|_{\text{click}}$. To calculate error in $g^{(2)}_{CC}$ and $g^{(2)}_{CC}|_{\text{click}}$, we employ bootstrapping with replacement using 10^5 bootstraps to construct the probability density functions shown in Fig. 8.11a. Finally, error estimates were calculated by numerical integration of the distributions such that they they cover a 34.1% confidence interval above and below the mean. The error estimates calculated using this process vs. number of bootstraps is shown in Fig. 8.11b-c for the conditional and unconditional datasets. We find that the use of 10^5 bootstraps yields acceptable convergence in the error estimate.

To mitigate the effects of long term drifts in frequencies of the microwave modes, we periodically measured the unconditional microwave power spectrum and monitored the resonance frequencies, $\omega_{\pm}$. This additionally allowed us to characterize the spectral diffusion of the microwave modes. In our data analysis, we excluded intervals of the measurement where the mode frequencies drifted by more than twice the standard deviation associated with spectral diffusion, which represented 3% of all recorded traces.

8.13 Classical Bound on the Conditional Second Order Intensity Correlation

In the previous chapters, we claim that the conditional microwave autocorrelation function is expected to satisfy the inequality, $g^{(2)}_{CC}|_{\text{click}} \geq 1$ for classical microwave-optical states. This can be proved by rewriting the conditional quantities defined in the previous chapters in terms of correlators of the joint microwave-optical state,

$$\begin{aligned} g^{(2)}_{CC}(\tau)|_{\text{click}} &= \frac{\left\langle \hat{C}^{\dagger 2}(\tau)\hat{C}^{2}(\tau)\middle|\hat{C}^{\dagger 2}(\tau)\hat{C}^{2}(\tau)\right\rangle|_{\text{click}}}{\left(\left\langle \hat{C}^{\dagger}(\tau)\hat{C}(\tau)\middle|\hat{C}^{\dagger}(\tau)\hat{C}(\tau)\right\rangle|_{\text{click}}\right)^2} \\ &= \frac{\left\langle \hat{A}^{\dagger}\hat{C}^{\dagger 2}(\tau)\hat{C}^{2}(\tau)\hat{A}\middle|\hat{A}^{\dagger}\hat{C}^{\dagger 2}(\tau)\hat{C}^{2}(\tau)\hat{A}\right\rangle\left\langle \hat{A}^{\dagger}\hat{A}\middle|\hat{A}^{\dagger}\hat{A}\right\rangle}{\left(\left\langle \hat{A}^{\dagger}\hat{A}\middle|\hat{A}^{\dagger}\hat{A}\right\rangle\left\langle \hat{C}^{\dagger}(\tau)\hat{C}(\tau)\middle|\hat{C}^{\dagger}(\tau)\hat{C}(\tau)\right\rangle\right)^2}, \end{aligned} \tag{8.28}$$

where the above correlators are explicitly written in normal order. Using the the optical equivalence theorem, we can recast the expectation values of the above

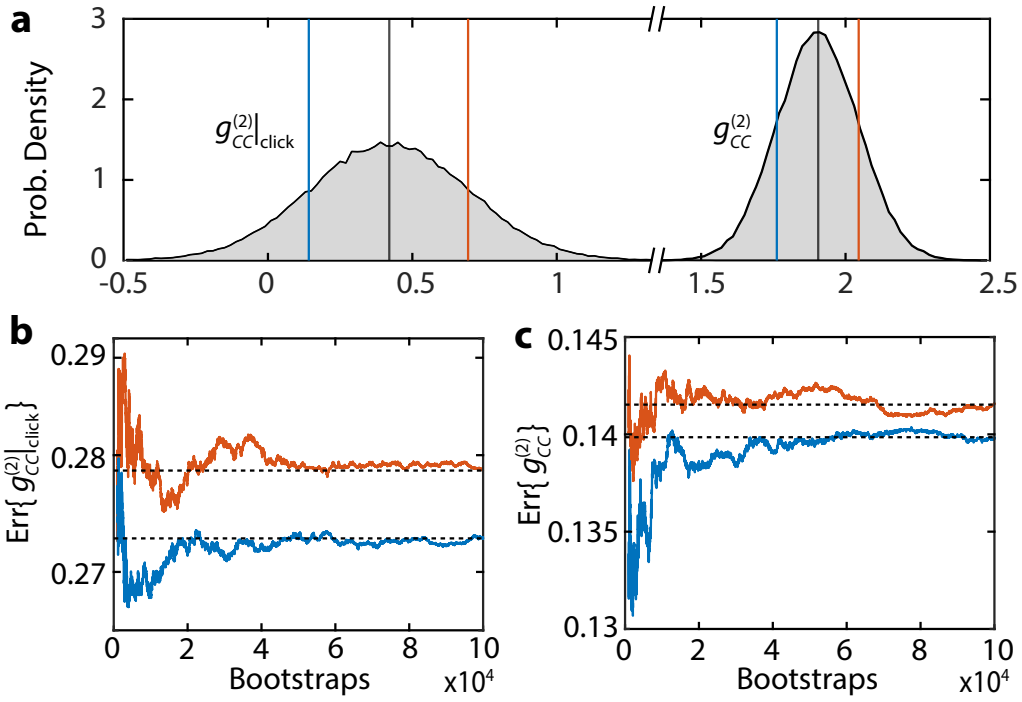

Figure 8.11: $g^{(2)}_{CC}$ **probability distribution.a.** Probability distribution for $g^{(2)}_{CC}$ and $g^{(2)}_{CC}|_{\text{click}}$ calculated from bootstrapping. Vertical blue and red lines correspond to one standard deviation above and below the distribution mean, respectively. **b,c.** Convergence of the error estimate vs. number of bootstraps for all traces, and optically heralded traces, respectively. Blue lines correspond to positive error, red lines to negative error, and black lines indicate the error estimate used in the previous chapters.

correlators in phase space using the Sudarshan-Glauber P representation [88, 98] as

$$\left\langle \hat{A}^{\dagger m}\hat{C}^{\dagger n}(\tau)\hat{A}^{m}\hat{C}^{n}(\tau)\middle|\hat{A}^{\dagger m}\hat{C}^{\dagger n}(\tau)\hat{A}^{m}\hat{C}^{n}(\tau)\right\rangle = \int |\alpha|^{2m}|\gamma|^{2n}P_{\tau}(\alpha,\gamma)d^{2}\alpha d^{2}\gamma$$
$$:= \left\langle |\alpha|^{2m}|\gamma|^{2n}\middle||\alpha|^{2m}|\gamma|^{2n}\right\rangle_{P_{\tau}}, \tag{8.29}$$

where $P_{\tau}(\alpha,\gamma)$ is the joint phase space density cprresponding to modes $\hat{A}$ and $\hat{C}$ with relative delay τ. Applying this directly to Eq. (8.28) gives,

$$g^{(2)}_{CC}(\tau)|_{\text{click}} = \frac{\left\langle |\alpha|^{2}_{P}|\gamma|^{4}\middle||\alpha|^{2}_{P}|\gamma|^{4}\right\rangle_{P_{\tau}}\left\langle |\alpha|^{2}\middle||\alpha|^{2}\right\rangle_{P_{\tau}}}{\left\langle |\alpha|^{2}|\gamma|^{2}\middle||\alpha|^{2}|\gamma|^{2}\right\rangle^{2}_{P_{\tau}}} \geq 1, \tag{8.30}$$

which follows directly from the Cauchy-Schwarz inequality.

8.14 Convergence of $g^{(2)}_{AC}$ to the Classical Bound

The results of pump power dependent measurements of the normalized intensity cross-correlation function, $g^{(2)}_{AC}$ are shown in Fig. 8.12.

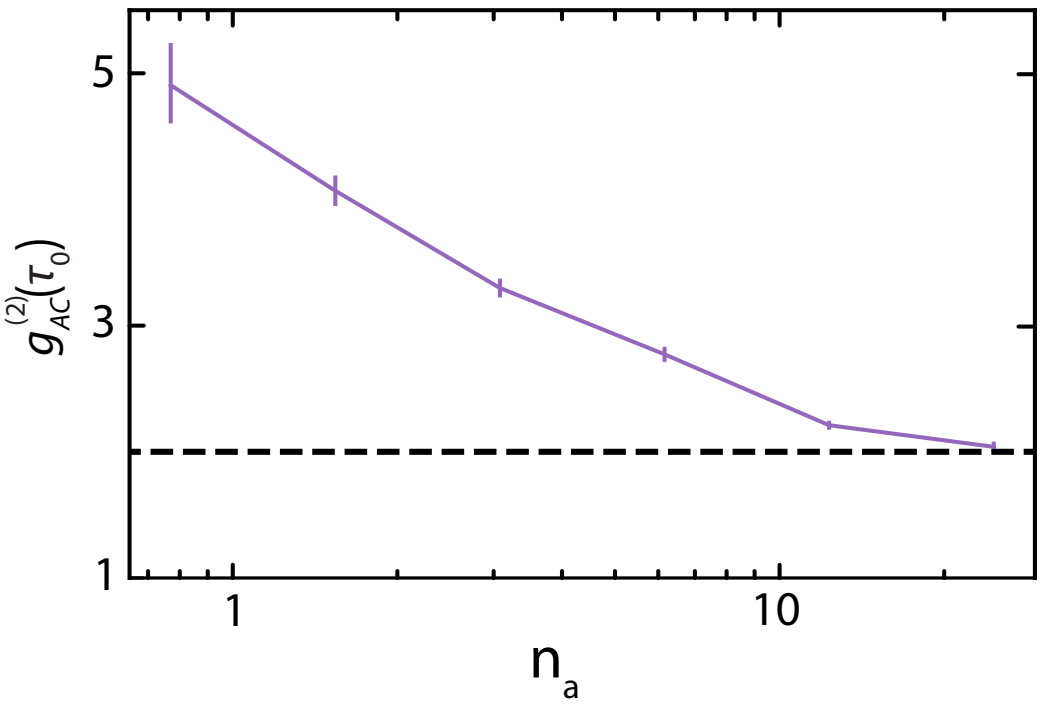

Figure 8.12: $g^{(2)}_{AC}$ **power dependence.**Maximum value of $g^{(2)}_{AC}$ versus increasing pump power plotted on the horizontal axis as the peak intra-cavity occupation of the optical mode, n_a. Dashed line denotes the classical upper bound of 2.

All measurements were performed with the same pump pulse duration and repetition rate used to acquire data in the previous chapters. We observe that at higher pump powers, the value of $g^{(2)}_{AC}$ approaches the classical upper bound of 2 as expected from the increased thermal noise added to the photon pair generated in SPDC. The data in this figure was collected from the same device used for the experiments in the previous chapters albeit after a partial warm up and cooldown to base temperature. This thermal cycle led to modified device parameters, which produced an increase in $g^{(2)}_{AC}$ at the lowest pump power of $n_a = 0.8$ compared to the result presented in the previous chapters.

8.15 Outlook

Towards entanglement of remote quantum processors, the microwave emission from such a transducer can be efficiently absorbed in a superconducting qubit [99] in a separate processor module [100]. Following the DLCZ protocol [101], interference of optical emission from two transducers and single photon detection can herald entanglement between remote superconducting qubits [102]. In this work, we demonstrate both a capable transducer and key experimental techniques for such a remote entanglement scheme. In the near term, for two nodes separated by tens of

meters in a single facility, propagation delays for optical photons will be much shorter than decoherence times of state-of-the-art transmon qubits [103]. Thus the fidelity of the Bell state heralded between remote qubits will be primarily determined by the fidelity of a single microwave photon heralded with an individual transducer. With our current pair source, a simulation of the conditional microwave state estimates this fidelity at $\sim 40\%$ (Section 8.12). With a modest increase in piezoelectric coupling, g_{pe} by a factor of few, the main source of infidelity, microwave loss during piezoelectric conversion, can be significantly reduced to increase the fidelity to $\sim 80\%$. The heralding rate of $0.14\mathrm{s}^{-1}$ in the present work can be increased by nearly an order of magnitude if the optomechanical coupling, g_{om} and fiber to waveguide coupling efficiency can each be improved by a factor of two. These improvements to fidelity and heralding rate are well within reach of our current design with better fabrication yield. In addition to these transducer performance improvements, dual rail encoding of microwave and optical photons in time bin [74] or frequency bin [75] degrees of freedom allows for detection of photon loss errors via a parity check. Since this approach involves generation of microwave-optical Bell pairs in a single node, it also provides a natural setting to explicitly verify microwave-optical entanglement. The sub-linear scaling of noise with pump power indicates that long-term improvements to fidelity and heralding rate will need to be driven by mitigation of pump-induced noise. In agreement with our previous work [48], we find that the noise for a given scattering probability in piezo-optomechanical transducers is significantly higher than that in pure silicon OMCs [84, 85]. Understanding this large gap will require more detailed studies of pump-induced heating, which could be performed via efficient microwave readout as shown in this work. From the standpoint of engineering improved chip-scale optomechanical transducers, higher acoustic energy participation in silicon [104] with a stronger piezoelectric material [72, 105], electrostatic approaches [106], and OMCs with better thermalization of the acoustic mode [107] are promising avenues towards low noise at higher heralding rates.

Chapter 9

MICROWAVE-OPTICAL BELL STATE

9.1 Introduction

Entanglement is an extraordinary feature of quantum mechanics. Sources of entangled optical photons were essential to test the foundations of quantum physics through violations of Bell's inequalities. More recently, entangled many-body states have been realized via strong non-linear interactions in microwave circuits with superconducting qubits. Here we demonstrate a chip-scale source of entangled optical and microwave photonic qubits. Our device platform integrates a piezo-optomechanical transducer with a superconducting resonator which is robust under optical illumination. We drive a photon-pair generation process and employ a dual-rail encoding intrinsic to our system to prepare entangled states of microwave and optical photons. We place a lower bound on the fidelity of the entangled state by measuring microwave and optical photons in two orthogonal bases. This entanglement source can directly interface telecom wavelength time-bin qubits and GHz frequency superconducting qubits, two well-established platforms for quantum communication and computation, respectively.

Our work arises from the need for scalable techniques to connect superconducting quantum processors of increasing size and complexity [103]. In analogy with classical information processing networks, quantum networks have recently been envisioned with optical channels as low loss, room temperature links between superconducting processors cooled in separate dilution refrigerator nodes. Over the past two decades, optical distribution of remote entanglement has been achieved with atoms, ions, color centers, quantum dots and mechanical oscillators [108–112]. The majority of such demonstrations towards optical quantum networks rely on the DLCZ protocol [101] and its variants, which are based on a quantum light-matter interface in each node of the network. In these experiments, entanglement is heralded between distant matter qubits through interference of emitted optical photons followed by single photon detection measurements. Remarkably, the fidelity of the entangled pair is insensitive to optical losses since the heralding operation naturally selects events within the computational subspace. Popular variants of this scheme also provide insensitivity to differences in optical path length, and rely on

preparation of entangled states between the matter qubit and an optical photonic qubit as a key ingredient [113–116]. Recently, there have been proposals to develop this fundamental capability for superconducting qubits by using quantum transducers to prepare microwave-optical Bell states [74, 75]. In this work, we bring this first enabling step of a well-established optical entanglement distribution toolkit into the realm of superconducting microwave circuits.

Microwave-optical entanglement generation with transducers has been elusive due to relatively weak nonlinearities, noise from parasitic optical absorption and losses from device integration challenges. In recent progress, a bulk electro-optic transducer was used to infer continuous variable entanglement between microwave and optical fields at the output ports of the device [117]. In contrast, the entanglement fidelity in our approach is insensitive to losses in collection and detection of optical and microwave photons which are inevitable in a realistic experimental setting. Moreover, our discrete variable approach offers the advantage that a microwave photonic qubit can be directly mapped onto a matter qubit such as a transmon with high fidelity [118]. Our demonstration builds on recent technical advances with piezo-optomechanical transducers, where integration with light-robust superconducting circuits has allowed the generation of microwave-optical photon pairs via spontaneous parametric down-conversion (SPDC) [119]. We drive emission from such a transducer into dual-rail optical and microwave photonic qubits, each containing exactly one photon in the microwave and optical output ports, respectively. To define the optical photonic qubit, we use a time-bin encoding, the preferred choice in long-distance optical quantum communication [120]. To define the microwave photonic qubit, we use two orthogonal modes which naturally arise from strongly hybridized acoustic and electrical resonances in our device. We verify entanglement by correlating microwave quantum state tomography results with detection of a single optical photon in a chosen time-bin, or coherent superposition of time-bins achieved with a time-delay interferometer.

Fig. 9.1a shows a simplified schematic of our microwave-optical entanglement source, which we operate in a dilution refrigerator setup at a temperature of ~20mK. Details of the device geometry and fabrication process have been provided in previous work [119]. Pump laser pulses are used to excite a piezo-optomechanical transducer containing a silicon optomechanical crystal resonator which supports optical and acoustic resonances at frequencies, $\omega_{\mathrm{o}} \approx 2\pi \times 200\mathrm{THz}$ and $\omega_{\mathrm{m}} \approx 2\pi \times 5\mathrm{GHz}$, respectively. Co-localized telecom photons and microwave

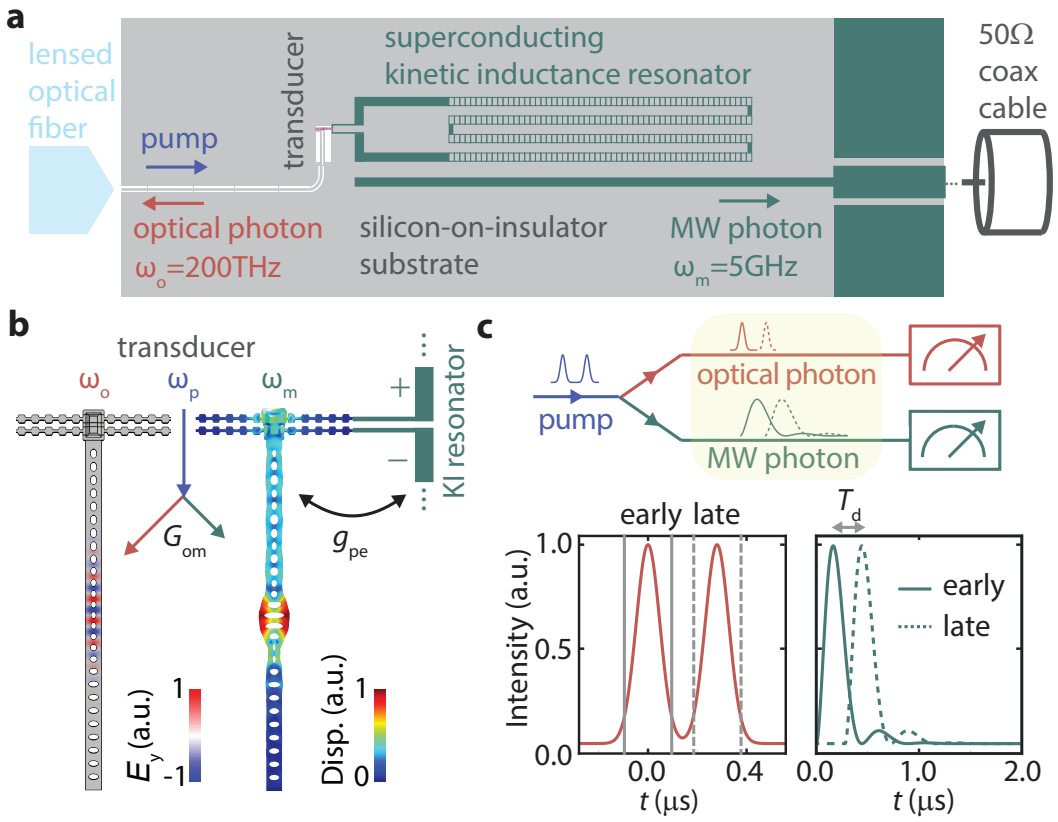

Figure 9.1: **Microwave-optical entanglement source. a.** Simplified schematic of various components of the chip-scale microwave-optical entanglement source, not shown to scale to aid presentation. The terminals of the superconducting kinetic inductance resonator are galvanically connected to the electrical terminals of the piezo-optomechanical transducer, shown in detail in panel b. The optical cavity in the transducer is coupled to an optical waveguide, which terminates on the left edge of the chip, where a lensed optical fiber is used to launch pump pulses into the device, and to collect emitted optical photons in the reverse direction. Microwave (MW) photons emitted by the device are capacitively coupled from the superconducting resonator to an on-chip transmission line and eventually collected in a 50ohm coax cable. **b.** Illustration of the SPDC process in the transducer where a pump photon at frequency, ω_p decays into optical and microwave excitations at frequencies, ω_o and ω_m, respectively, due to the parametric optomechanical interaction at a rate, G_om. The microwave excitation is shared between the transducer acoustic mode and the electrical mode of a superconducting kinetic inductance (KI) resonator, which are strongly hybridized with the piezoelectric interaction strength, g_pe. Simulated profiles of the optical electric field (left) and microwave acoustic displacement field (right) in the transducer are shown. **c.** Schematic for generation of Bell states between dual-rail optical and MW photonic qubits. Two consecutive Gaussian pump pulses induce emission of single optical and MW photons into early and late modes centered at their respective frequencies. Theoretically calculated intensity envelopes of these modes are shown when the device is excited with two Gaussian pump pulses separated by a time delay, T_d = 279ns, which ensures orthogonality of early and late modes used for the dual-rail encoding.

phonons in this wavelength-scale resonator can interact via radiation pressure and the photoelastic effect [84]. By tuning the pump laser frequency to $\omega_\mathrm{p} = \omega_\mathrm{o} + \omega_\mathrm{m}$ we induce spontaneous parametric down-conversion into a photon-phonon pair at frequencies ω_o and ω_m, as illustrated in Fig. 9.1b. The optomechanical interaction

occurs with a parametrically enhanced strength, $G_{\mathrm{om}} = \sqrt{n_{\mathrm{p}}} g_{\mathrm{om}}$, where n_{p} is the number of intra-cavity pump photons and $g_{\mathrm{om}}/2\pi = 270\mathrm{kHz}$ is the optomechanical coupling rate at the single photon and phonon level in the device under study. Single phonons from the SPDC process are converted into single microwave photons in a niobium nitride superconducting kinetic inductance resonator tuned into resonance with the transducer acoustic mode. This conversion process is mediated by a compact aluminum nitride piezoelectric component in the transducer, and occurs at a rate, $g_{\mathrm{pe}}/2\pi = 1.2\mathrm{MHz}$, which exceeds damping rates of the acoustic and electrical modes in the device under study [79]. Finally, as shown in Fig. 9.1a, both optical and microwave photons emitted from the device decay into on-chip waveguides and are routed into a lensed optical fiber and a 50ohm microwave coaxial cable, respectively.

9.2 Preparing Entangled States

To prepare entangled microwave-optical states, we excite the device with two consecutive pump pulses. Each pump pulse can produce a microwave-optical photon-pair in well-defined temporal modes, separated in time and centered at frequencies, ω_{m} and ω_{o} in the microwave and optical outputs, respectively. Fig. 9.1c shows theoretically expected intensity envelopes of these 'early' and 'late' modes in the optical and microwave output ports of the device. The optical early and late mode envelopes adiabatically follow the pump pulses since the optomechanical interaction strength, G_{om} is much smaller than the decay rate of the optical cavity. In our experiments, we use Gaussian pump pulses with two sigma width, $T_{\mathrm{p}} = 96\mathrm{ns}$, and define time-bin modes for dual-rail encoding of the optical photonic qubit. The corresponding microwave early and late modes exhibit damped oscillatory behavior due to strongly coupled electrical and acoustic resonators in the device. By matching the duration between the pump pulses, $T_{\mathrm{d}} = 279\mathrm{ns}$ to the electro-acoustic oscillation period expected from microwave spectroscopy [79], we can achieve orthogonal early and late modes for dual-rail encoding of the microwave photonic qubit. Physically, a single phonon scattered by the SPDC process into the electro-acoustic coupled mode system oscillates between the acoustic and electrical resonators as it preferentially decays into the microwave output waveguide. With our specific choice of the pump pulse delay, T_{d}, we excite the transducer with the late pump pulse precisely at the moment when the phonon from the early pump pulse has been maximally swapped into the electrical mode. In this setting, the joint wavefunction of early and late

modes in the optical and microwave output ports of the device can be written as

$$|\Psi\rangle \approx |00\rangle_{\mathrm{o}}|00\rangle_{\mathrm{m}} + \sqrt{p}\left(|10\rangle_{\mathrm{o}}|10\rangle_{\mathrm{m}} + e^{i\phi_{\mathrm{p}}}|01\rangle_{\mathrm{o}}|01\rangle_{\mathrm{m}}\right) + O(p), \tag{9.1}$$

where $|kl\rangle_{\mathrm{o}}$ ($|kl\rangle_{\mathrm{m}}$) denotes the direct product of a k-photon state in the early mode and an l-photon state in the late mode on the optical (microwave) output port. The phase ϕ_{p}, is set by the relative phase between early and late pump pulses. When the scattering probability, $p \ll 1$, the $O(p)$ terms may be neglected and detection of a single optical photon can be used to post-select an entangled state between an optical photonic qubit in the $\{|10\rangle_{\mathrm{o}}, |01\rangle_{\mathrm{o}}\}$ manifold and a microwave photonic qubit in the $\{|10\rangle_{\mathrm{m}}, |01\rangle_{\mathrm{m}}\}$ manifold. The state vectors within curly brackets define the native measurement basis of the photonic qubits, which we call the Z-basis in reference to the north and south poles of the Bloch sphere. We refer to a rotated measurement basis on the equator of this Bloch sphere as the X-basis. To verify entanglement, we characterize correlations between the photonic qubits in these two orthogonal bases. In our experiments, we operate with optical pulses with a peak power of 83nW corresponding to an intra-cavity optical photon number, $n_{\mathrm{p}} = 0.8$, which leads to $p = 1.0\times10^{-4}$. The power level is chosen to limit noise added due to pump-induced heating of the transducer, and thereby, preserve microwave-optical entanglement. With external optical collection efficiency, $\eta_{\mathrm{opt}} = 5.5 \times 10^{-2}$ and a pulse repetition rate, $R = 50$kHz, we detect heralding events at a rate, $R_{\mathrm{click}} = 0.26\mathrm{s}^{-1}$. Microwave phonon to photon conversion is expected to occur with efficiency, $\eta_{\mathrm{mw}} = 0.59$ based on the piezoelectric coupling rate and microwave damping rates in our device.

9.3 Characterization of Entangled States

We first measure the time-resolved microwave output intensity from the device conditioned on the detection time of single optical photons. This allows us to characterize microwave-optical intensity correlations in the Z-basis. In this measurement, depicted schematically in Fig. 9.2a, optical emission from the device is detected on a superconducting nanowire single photon detector (SNSPD) after transmission through a filter setup to reject pump photons. Fig.9.2b shows a histogram of single optical photon detection times revealing two nearly Gaussian envelopes associated with the SPDC signal. We use gating windows of width, $2T_{\mathrm{p}} = 192$ns centered around each pulse to define the early and late optical modes, $\hat{A}_{\mathrm{e}}$ and $\hat{A}_{\mathrm{l}}$, respectively. Simultaneously, as shown in Fig. 9.2a, microwave emission from the device is directed to an amplification chain with a near-quantum-limited Josephson

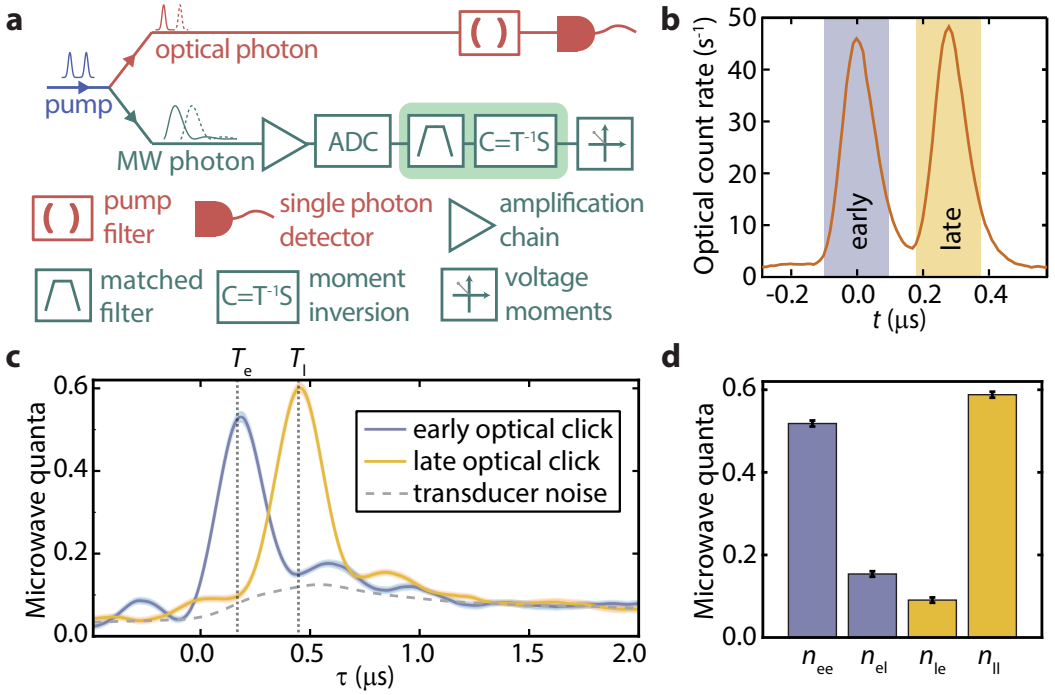

Figure 9.2: **Z-basis intensity correlations. a.** Simplified schematic of experimental setup used to detect correlations between microwave (MW) and optical emission in the Z-basis of the dual-rail qubits. Shaded green box on the MW detection path indicates post-processing on voltage traces from the heterodyne setup after analog-to-digital conversion (ADC). **b.** Histogram of single optical photon detection times plotted as a time trace of optical count rate. Shaded vertical regions indicate gating windows used to define early and late optical time-bin modes, $\hat{A}_\mathrm{e}$ and $\hat{A}_\mathrm{l}$. **c.** Quanta in the transducer microwave output mode defined by a filter function matched to the theoretically expected emission envelope, $f(t-\tau)$ centered at the MW resonance frequency, ω_m [79]. The variable readout delay, τ is shown on the x-axis and the occupation of the mode for a given τ is shown on the y-axis. Blue and yellow traces show MW output quanta conditioned on early and late optical clicks, respectively, and the dashed gray trace shows unconditional MW output quanta, which correspond to transducer-added noise. Dotted vertical lines indicate readout delays, T_e and T_l used to define early and late MW modes, $\hat{C}_\mathrm{e}$ and $\hat{C}_\mathrm{l}$. The conditional traces are an average over $\approx 3\times10^5$ heralding events. Shaded regions around traces span a confidence interval of two standard deviations about the mean. **d.** Output quanta, n_{ij} in MW mode j conditioned on an optical click in mode i, where i, j run over the early and late modes denoted by e,l. Data in this panel corresponds to $\approx 3\times10^5$ heralding events. Error bars indicate $+/-$ one standard deviation.

traveling wave parametric amplifier (TWPA) as the first stage. The amplified microwave signal is down-converted in a room-temperature heterodyne receiver and the resulting voltage quadratures are sent to an analog-to-digital conversion (ADC) card, allowing us to record a digitized, complex-valued voltage trace for each experimental trial. We capture emission at the microwave resonance frequency, ω_m using a digital filter matched to the theoretically expected microwave emission envelope, $f(t-\tau)$, where τ is a variable readout delay [79]. We then subtract independently calibrated amplifier-added thermal noise of approximately 2.6 quanta via a moment inversion procedure [83]. Upon post-selecting measurement records from

trials which produced optical clicks, we observe that the microwave intensity conditioned on a late click is delayed with respect to that conditioned on an early click as shown by the solid traces in Fig. 9.2c. These conditional signals contain a finite amount of pump-induced thermal noise from the transducer. Since $p \ll 1$, such noise is simply given by the unconditional microwave output intensity, shown with the dashed time trace in Fig. 9.2c. The ratio of the conditional and unconditional microwave intensities yields the normalized microwave-optical cross-correlation function, $g^{(2)}_{AC}$ which reaches a maximum value of 6.8 for early optical clicks, and 5.0 for late optical clicks. Both values exceed the Cauchy-Schwarz bound of 2 for thermal states, and signify non-classical microwave-optical correlations [119]. By performing the matched filter operation at optimal microwave readout delays, T_e and $T_\mathrm{l} = T_\mathrm{e} + T_\mathrm{d}$, shown by the dotted vertical lines in Fig. 9.2c, which maximize the cross-correlation, we define microwave early and late modes, $\hat{C}_\mathrm{e}$ and $\hat{C}_\mathrm{l}$. Fig. 9.2d shows conditional occupations of these modes with the symbol n_{ij} for the occupation of microwave mode j conditioned on an optical click detected in mode i. Using these four conditional microwave mode occupations, we define the Z-basis visibility, $V_\mathrm{z} = (n_\mathrm{ee} - n_\mathrm{el} - n_\mathrm{le} + n_\mathrm{ll})/(n_\mathrm{ee} + n_\mathrm{el} + n_\mathrm{le} + n_\mathrm{ll})$. For a Bell state without additional noise or microwave loss, we expect $n_\mathrm{ee} = n_\mathrm{ll} = 1$ and $n_\mathrm{el} = n_\mathrm{le} = 0$, resulting in $V_\mathrm{z} = 1$. On the contrary, when the microwave and optical intensities are fully uncorrelated, we expect $V_\mathrm{z} = 0$. From the data in Fig. 9.2d, we find $V_\mathrm{z} = 0.633 \pm 0.014$, indicating significant intensity correlations between early and late modes in the microwave and optical outputs.

This observation of Z-basis correlations is also compatible with a statistical mixture of early and late microwave-optical photon pairs. To rule out this scenario, we characterize intensity correlations in the X-basis, which are indicative of the phase coherence of the entangled microwave-optical state. On the optics side, the measurement basis rotation is performed with a time-delay interferometer inserted into the detection path as shown in Fig.9.3 a. The interferometer is built with a fiber delay line in one arm to achieve the time delay, $T_\mathrm{d} = 279$ns required to interfere early and late optical time-bins. Additionally, the setup imprints a relative phase between the time-bins, ϕ_o, which is actively stabilized through feedback on a piezoelectric fiber stretcher in one of the arms. The relative phase between the pump pulses used to excite the transducer, ϕ_p, is controlled using an electro-optic phase modulator [121]. With one output port of the interferometer connected to the single photon detection path, clicks registered on the SNSPD correspond to measurement of a single photon in the mode, $(\hat{A}_\mathrm{e} + e^{i(\phi_\mathrm{p}+\phi_\mathrm{o})}\hat{A}_\mathrm{l})/\sqrt{2}$. The measurement phase, $\phi_\mathrm{p}+\phi_\mathrm{o}$ can be indepen-

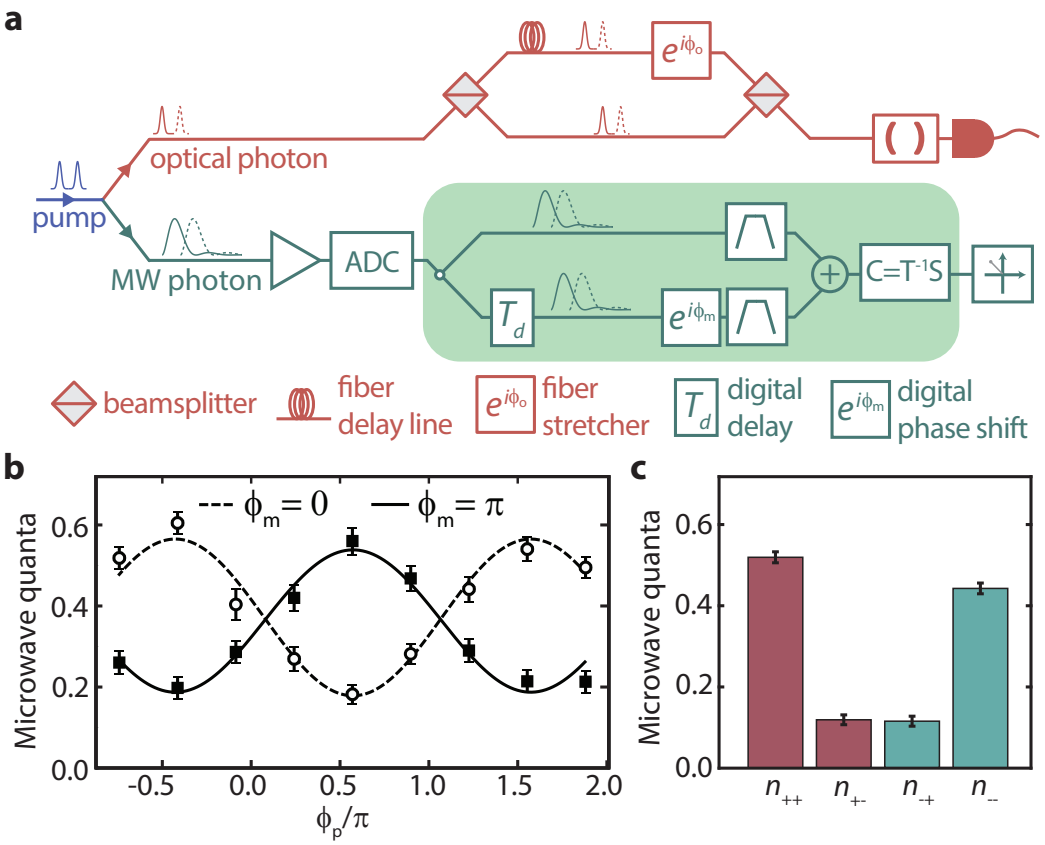

Figure 9.3: **X-basis intensity correlations. a.** Simplified schematic of experimental setup used to detect correlations between microwave (MW) and optical emission in the X-basis of the dual-rail qubits. A time-delay interferometer in the optical path is used to interfere early and late optical time-bins with a relative phase, ϕ_o. The interference operation in MW detection with a relative phase, ϕ_m is performed in digital post-processing as shown in the shaded green box. **b.** Output quanta in the MW mode, $(\hat{C}_e + e^{i\phi_m}\hat{C}_l)/\sqrt{2}$, for two phase settings, $\phi_m = 0$ (open circles) and $\phi_m = \pi$ (filled squares), conditioned on an optical click in the mode, $(\hat{A}_e + e^{i(\phi_p+\phi_o)}\hat{A}_l)/\sqrt{2}$ at the output of the time-delay interferometer. The relative phase between the pump pulses, ϕ_p is varied along the horizontal axis while ϕ_o is kept constant at 0.31π. The uncertainty in the calibrated optical phase over the duration of the measurement is $\pm 0.03\pi$. Solid and dashed lines are cosine fits. Data in this plot is acquired at three times the pump power used for the main dataset, and represents an average over $\approx 1 \times 10^4$ heralding events per optical phase setting. All error bars indicate +/− one standard deviation. **c.** Output quanta, n_{ij} in MW mode j conditioned on an optical click in mode i, where i, j run over the X-basis MW and optical measurement modes denoted by +, − and corresponding to phase settings, $\phi_m = 0.56\pi, 1.56\pi$ and $\phi_p + \phi_o = 0.56\pi, 1.56\pi$, respectively, where ϕ_o is kept constant at 0.28π. The uncertainty in the calibrated optical phase over the duration of the measurement is $\pm 0.04\pi$. Data in this panel corresponds to an average over $\approx 7 \times 10^4$ heralding events for + and − optical outcomes. All error bars indicate +/− one standard deviation.

dently calibrated by transmitting coherent optical pulses through the interferometer [79]. To perform a basis rotation on the microwave side, we add the early and late complex voltage quadratures with a relative phase, ϕ_m in post-processing as shown in Fig.9.3 a. After subtracting amplifier-added noise in a manner similar to the Z-basis measurement, we measure the moments of the microwave mode, $(\hat{C}_e + e^{i\phi_m}\hat{C}_l)/\sqrt{2}$,

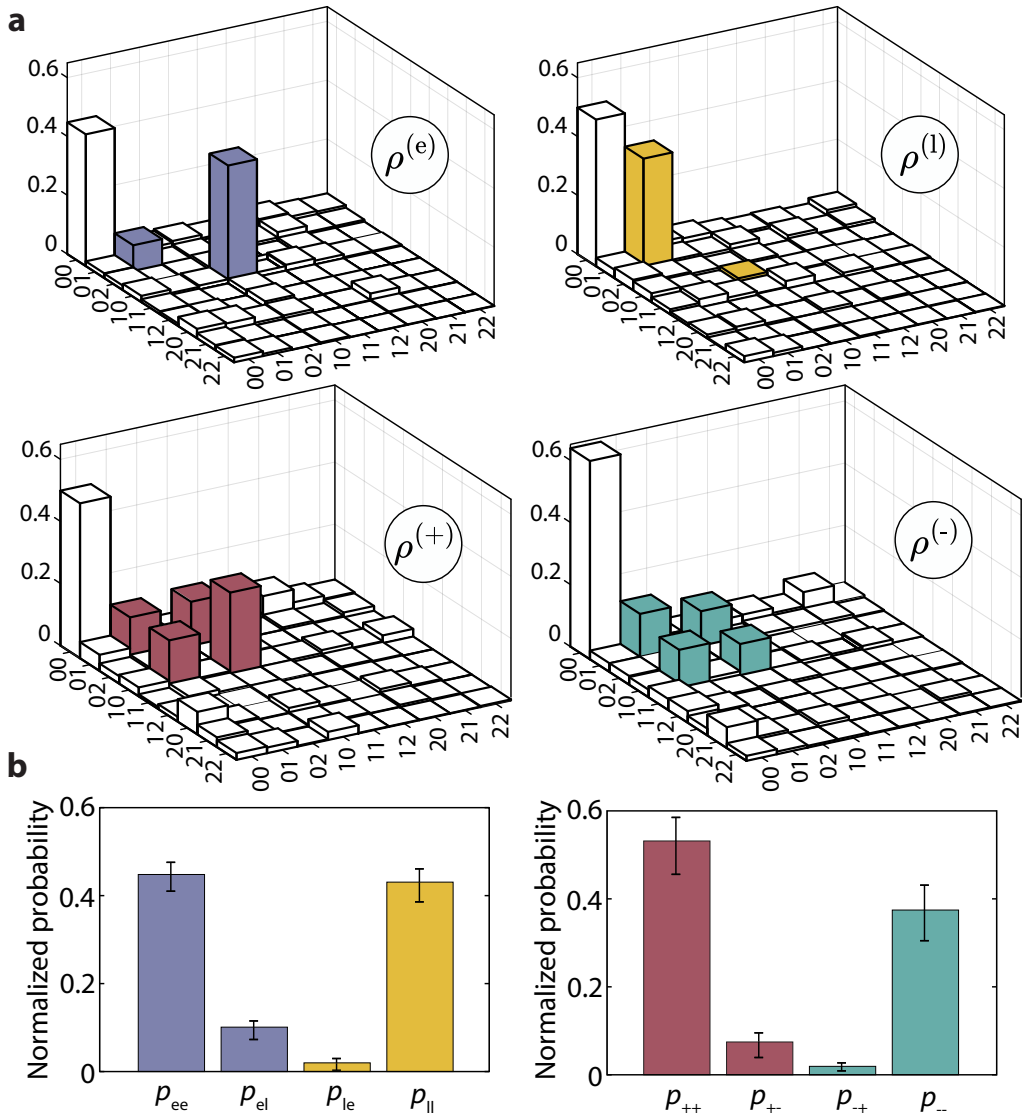

Figure 9.4: **Quantum state tomography of conditional microwave states. a.** Conditional density matrices, $\rho^{(e)}, \rho^{(l)}$, $\rho^{(+)}, \rho^{(-)}$ of the microwave output state corresponding to early, late, + and − optical clicks, respectively, plotted in the joint Fock basis of early and late microwave modes. The matrices are obtained from a maximum likelihood reconstruction procedure performed over a joint Fock space of up to six photons in each mode, but are plotted in a truncated space of up to two photons in each mode for better visualization. Entries which are expected to be non-zero for a pure microwave-optical Bell state are highlighted in color. **b.** Conditional probability, p_{ij} of a single photon in microwave mode j conditioned on receipt of an optical click in mode i, calculated from the density matrices in panel a after post-selecting the single photon subspace. Error bars denote uncertainties of +/- one standard deviation.

averaged over experimental trials. In Fig.9.3 b, we show conditional microwave output quanta measured in the X-basis by fixing $\phi_m = 0, \pi$. As the optical phase is swept by tuning ϕ_p between the pump pulses, we observe correlation fringes in the conditional microwave intensity, a clear signature of coherence of the entangled

microwave-optical state. Due to the need for data at multiple optical phase settings for this measurement, we used three times higher pump power ($n_\mathrm{p} = 2.4$) compared to the main dataset to speed up acquisition. We then lower the pump power back to $n_\mathrm{p} = 0.8$, the setting used in the Z-basis measurements, and repeat the X-basis measurement for two optical phase settings, $\phi_\mathrm{p} + \phi_\mathrm{o} = 0.56\pi, 1.56\pi$ at which we define the optical modes, $\hat{A}_\pm$, respectively. We measure conditional microwave output quanta in the modes, $\hat{C}_\pm$ for $\phi_\mathrm{m} = 0.56\pi, 1.56\pi$, respectively and obtain the results shown in Fig. 9.3c for the four combinations of the X-basis modes. In a manner similar to the Z-basis correlation measurement, we define the X-basis visibility, V_x, expected to equal 1 for Bell states, and 0 for an equal statistical mixture of early and late microwave-optical photon pairs. With the data in Fig. 9.3c, we observe $V_\mathrm{x} = 0.611 \pm 0.034$. As an additional consistency check, we swept the microwave readout phase, ϕ_m in post-processing, and found that the maximum in V_x occurs for the phase settings, $\phi_\mathrm{m} = 0.62\pi, 1.62\pi$, offset by 0.06π from the theoretically expected modes, $\hat{C}_\pm$. This can be attributed to a systematic offset in the calibrated optical phase arising from small differences in optical frequency and polarization between calibration and data acquisition [79]. The microwave and optical emission from the device exhibit intensity correlations in both Z- and X-bases which are characteristic of a Bell pair prepared from the pure state in Eq. 9.1 via optical detection. However, since the experimentally prepared states have finite transducer-added noise and microwave loss, the conditional microwave intensities have contributions from outside the computational subspace where the dual-rail photonic qubits are defined. In order to characterize entanglement more precisely, we must measure both optical and microwave outputs in the single-photon subspace. Since we operate in an experimental regime where the scattering probability, $p \ll 1$, we fulfill the condition that nearly all optical detection events arise from within the single optical photon subspace [79]. On the microwave side, we use statistical moments of conditional heterodyne voltages to perform maximum likelihood state tomography in the joint Fock basis of the early and late modes [83, 91], and project onto the single photon subspace. This post-selection operation is strictly local and cannot generate microwave-optical entanglement. It can be implemented in practice by performing a parity check [74], a well-established capability in circuit quantum electrodynamics. Fig. 9.4a shows conditional density matrices, $\rho^{(\mathrm{e})}, \rho^{(\mathrm{l})}, \rho^{(+)}, \rho^{(-)}$ of the microwave output state corresponding to an optical click in the early, late, + and − modes, respectively. For a pure Bell state, the entries highlighted with colored bars in $\rho^{(\mathrm{e})}, \rho^{(\mathrm{l})}$ are expected to have the values $\rho^{(\mathrm{e})}_{10,10} = \rho^{(\mathrm{l})}_{01,01} = 1$, $\rho^{(\mathrm{e})}_{01,01} = \rho^{(\mathrm{l})}_{10,10} = 0$;

likewise, the the entries highlighted with colored bars in $\rho^{(+)}, \rho^{(-)}$ are expected to have a magnitude of 0.5. The main deviation in the measured conditional microwave states is due to the non-zero vacuum component, primarily from finite conversion efficiency, $\eta_{\mathrm{mw}} = 0.59$ of a single phonon into the microwave waveguide. Using the entries highlighted with colored bars in Fig. 9.4a, which denote the computational subspace of the dual-rail photonic qubit, we obtain the conditional probability, p_{ij} of a single microwave photon in mode j conditioned on receipt of an optical click in mode i [79]. Here i, j run over early and late (+ and −) modes for Z- (X-) basis measurements, and the results are shown in Fig. 9.4b. Error bars on the probabilities account for statistical error obtained by bootstrapping with replacement over the microwave dataset. These conditional probabilities allow us to establish a lower bound on the Bell state fidelity given by [74, 114]

$$F_{\mathrm{lb}} = \frac{1}{2}(p_{\mathrm{ee}} + p_{\mathrm{ll}} - p_{\mathrm{el}} - p_{\mathrm{le}} + p_{++} + p_{--} - 2\sqrt{p_{+-}p_{-+}}). \tag{9.2}$$

We find that $F_{\mathrm{lb}} = 0.794^{+0.048}_{-0.071}$, which exceeds the classical limit of 0.5 by over four standard deviations, indicating the preparation of entangled microwave-optical states. A simple model accounting for pump-induced thermal noise in the transducer [79] predicts Bell state fidelity exceeding 0.83, which agrees with the measured lower bound. In addition to the primary reduction in the fidelity due to pump-induced noise, we expect smaller contributions due to dark counts and imperfections in optical time-bin interference and microwave mode matching.

9.4 Outlook

We envision that the microwave photonic qubit emitted by our entanglement source can be absorbed in a dual-rail superconducting qubit [74] or a superconducting qutrit [118], both of which can be realized with standard transmons and can enable detection of microwave photon loss errors. Such a transmon module can be connected to the transducer with minimal impact of optical pump light on qubit coherence [100, 122–124].

In the near term, piezo-optomechanical transducers with greater acoustic participation in silicon [104, 106] and improved thermalization with the substrate [107] can improve transducer noise performance, enabling microwave-optical entanglement generation rates in the kHz range. Transducer operation in this performance regime can facilitate the integration of superconducting qubit nodes into optical quantum

networks for applications in secure communication [125–127] and distributed sensing [128–130].

Part II

Part II: Light-robust Lithium Niobate Transducer

Chapter 10

INTRODUCTION

In this chapter we will discuss the advancement of our piezo-optomechanical transducers with the introduction of lithium niobate (LN). LN has an effective piezo coupling rate an order of magnitude larger than aluminum nitride. Large coupling per piezo volume means we can design a smaller cavity while maintaining the same coupling as a larger AlN cavity. The hybridized mechanical supermode as described in Chapter 2 requires energy participation in the piezo region as well as the OMC. The inherently lower mechanical quality factor of piezo materials compared to silicon typically means a hybridized piezo-OMC cavity will have more loss than a pure OMC cavity. This lower Q factor translates to more loss during the transduction process and a lower efficiency. The fundamental solution to this problem is to reduce the energy participation of the LN cavity as much as possible while maintaining large enough piezo coupling. There is also an upper bound for the piezo coupling to avoid cross coupling between adjacent mechanical modes. For our design the sweet spot is about 5-10 MHz of coupling. This rate is possible with AlN, but requires a much large piezo cavity than LN, which can achieve similar coupling with a 5X lower volume. With that said the advantage of LN is clear, however the fabrication of small LN features in non-trivial compared to AlN and in this chapter we will focus on the fabrication and intial characterization of the next-generation transducer devices.

Chapter 11

FABRICATION CHALLENGES

11.1 Lithium Niobate Etch Development

Lithium niobate is a very chemically stable material, so it is challenging to etch. In the past, a few different processes have been used to etch lithium niobate mainly for application in nanophotonics. These range from mechanical processes like dicing [131, 132] and chemical-mechanical polishing (CMP) [133–135] to wet etching [136–142] and dry etching [143–153]. We are interested in etching lithium niobate piezo-acoustic cavities with sub 1μm dimensions. In the literature, mechanical processes for micro-machining LN tend to be limited to feature sizes on the order of $\sim$ few μm which is too large for our purposes. For wet etching lithium niobate, the most common etchant used is a mix of hydrofluoric acid (HF) and nitric acid (HNO_3) [136–139]. Unfortunately, this mixture is also a silicon etchant [154], so it is also not suitable for our purposes. Undercutting below the mask is another common issue with wet-etching and makes it difficult to achieve tight dimension control for sub μm size features.

To prevent damage to the silicon (Si) device layer of our SOI substrate, it is important to develop an etch that is selective between LN and Si. To this end, we started investigating etchants that could etch LN without attacking Si. As mentioned earlier, the most commonly used wet etchant for LN is a mix of HF and HNO_3, but this etchant readily attacks Si. However [140, 141] showed that concentrated HF at elevated temperatures is able to etch -Z cut LN. HF does not etch Si and is commonly used to etch away native silicon oxide from the surface of Si wafers. However, there are significant safety concerns associated with heating HF to elevated temperatures. We decided to investigate if room temperature 48% concentrated HF could selectively etch -Z cut LN without attacking Si. The challenge with using concentrated HF as an etchant is to find a suitable etch mask since most materials are etched by HF. Gold (Au) is one of the few materials that is inert in HF. Since gold can be readily deposited using e-beam evaporation, we decided to use a gold mask for our HF etch. We again used e-beam lithography, e-beam evaporation, and metal liftoff to pattern our gold mask similar to the process used to pattern the chrome mask for dry etching. To improve the adhesion of gold to our LN thin film, we first

evaporate a thin 'adhesion layer' (~5-10nm) of chrome (Cr) followed by 110nm of gold. Such a Cr/Au mask is commonly used in etching of glass using HF.

Since our etchant (concentrated HF) selectively etches the -Z crystal face of LN much faster than any other crystal face, it is possible to achieve a highly anisotropic etch. To test our Cr/Au mask and the anistropy of the etch, we try to etch simple LN 'boxes' as shown in Fig. 11.2a. It is clear from the figure that this etch is fairly anisotropic giving sidewall angles as high as ~50 °. Further, the sidewall roughness is much reduced compared to the dry etch. However, in Fig. 11.2a, we have not yet etched all the way through the LN to the Si device layer. We find that while the HF etches the -Z surface of LN quite well and does not attack Si, when the etch reaches the interface between the LN and the underlying Si, it causes 'delamination' of our LN boxes as shown in Fig. 11.2c. We suspect that there is some native oxide present at the interface between the LN and the Si which is rapidly attacked by the HF causing the LN box to peel off.

In the previous sections, we have seen the advantages and disadvantages of the dry and wet etch processes for etching LN. The dry etch has the advantage of being anisotropic and not attacking the interface between LN and Si. However it is not selective between LN and Si, and hence causes significant damage to the Si surface. The wet etch using 48% HF on the other hand can be anisotropic and selective between LN and Si however it rapidly attacks the LN-Si interface. Here we propose a two step wet etch. In the first step we etch most of the way through the LN with concentrated HF. To avoid delamination of the LN box via etching of the interface layer by HF, in the second step we etch the last $\tilde{3}$0nm with a heated Standard Clean 1 (SC1) which is a mixture of amonium hydroxide and hydrogen peroxide. While this etches LN very slowly ($\tilde{2}$nm/min) it is selective to LN and does not etch the silicon substrate or the LN/Si interface layer. This two step process allows us to maintain an undamaged Si device layer without delaminating the LN boxes. Suggested steps for our proposed hybrid etch process are detailed below. We assume that we are starting with 150 nm of -Z cut LN on SOI.

Layer 1: Markers. Markers are used for alignment for subsequent e-beam lithography steps. In our group, we typically use $20\mu\text{m} \times 20\mu\text{m}$ squares of ~150 nm thick e-beam evaporated niobium (Nb) as our markers. However in this process we simplify this step by using the same gold layer used for the wet etch mask to define markers.

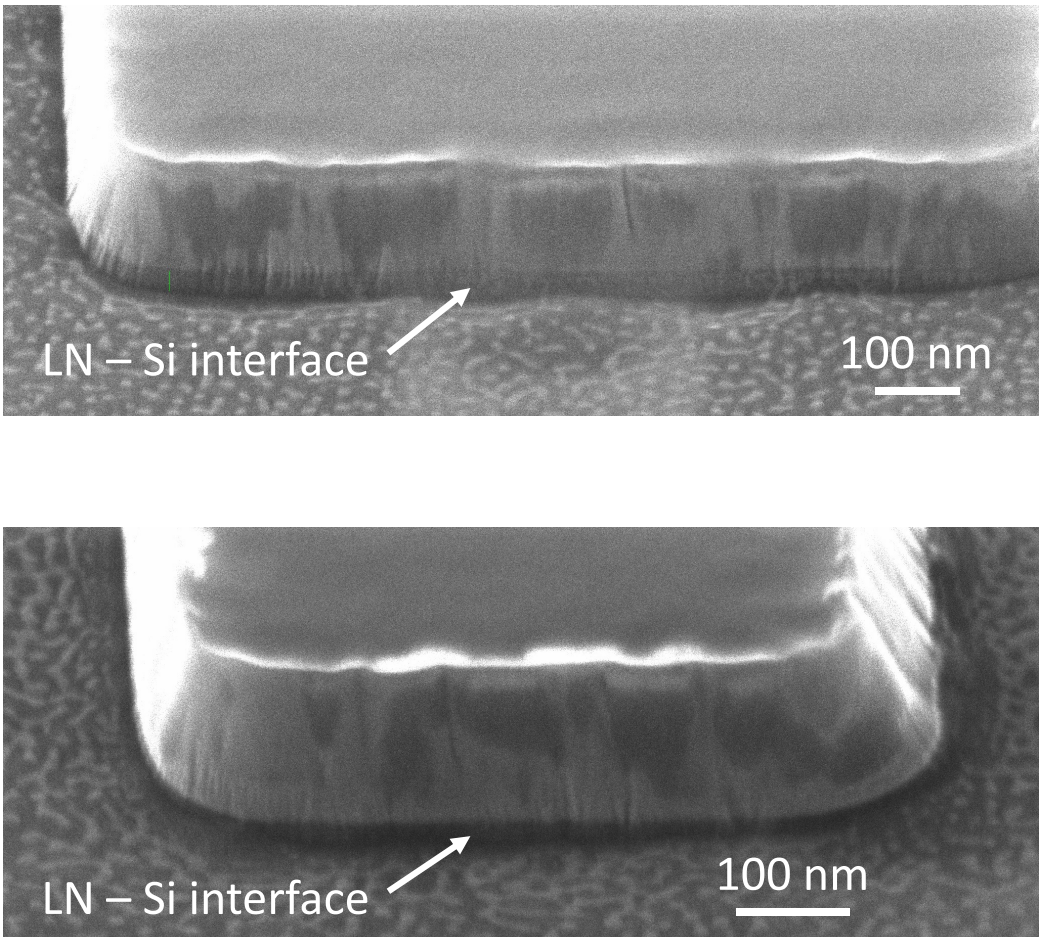

Figure 11.1: **LN piezo box etched using a combination of wet and dry etches.** Smooth sidewalls of a LN piezo box etched using a wet etch most of the way followed by a dry etch to clear the last ~40 nm of LN and expose the LN-Si interface. The damage to the silicon substrate as a result of the dry etch can be seen as roughness in these images.

1. Chip Cleaning
    - Acetone 5min sonication
    - IPA 5min sonication
    - N_2 blow dry
    - O_2 plasma ash at 150W, 12sccm O_2 flow for 2min
    - 15s dip in 10:1 Buffered HF (BHF) followed by 2x 10s DI H_20 rinse
2. Spin on Conductive Layer for E-beam Lithography
   Since LN is an insulating substrate, we need to deposit a conducting layer to

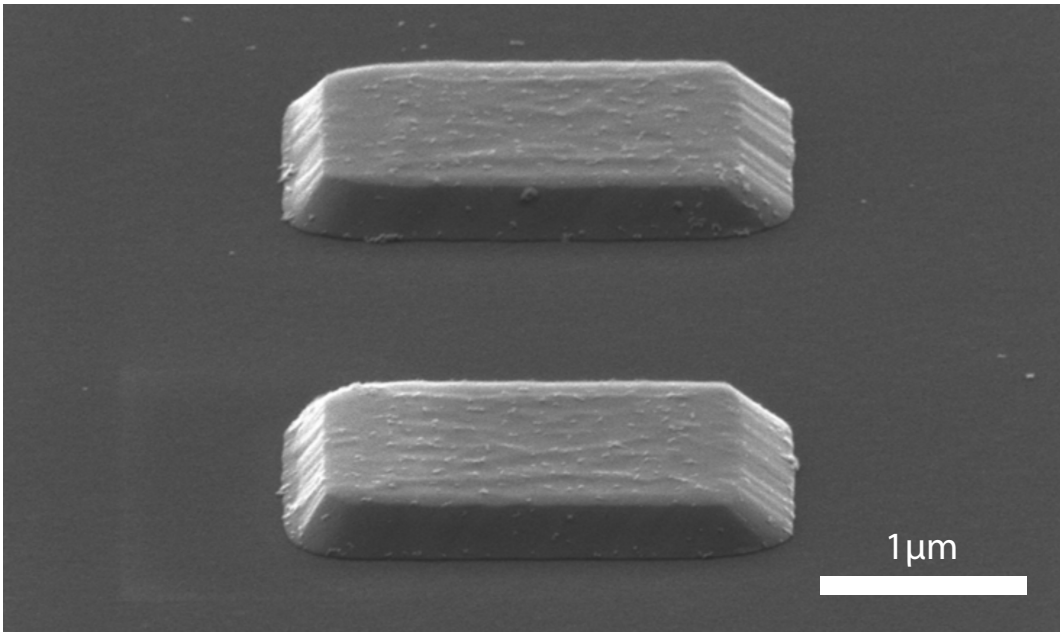

Figure 11.2: **Wet etched LN boxes.** LN box etched using 48% HF + SC1. Note that the etch has not progressed all the way to Si. There is a thin adhesion layer which is not etched by SC1.

prevent charging effects during electron-beam lithography. There are commercially available conductive polymers (such as AquaSave) which can be spun on top of e-beam resist and help disperse charge.

- Spin on AquaSave at 2200 rpm for 1 min

3. Spin/Bake ZEP 520a
   - Pre-bake at 180°C for 3min
   - Spin ZEP 520a at 3000 rpm for 1 min
   - Post-bake at 180°C for 3min
4. E-Beam Lithography
   - Beam current 50nA
   - Fracturing resolution 20nm
   - Dose 230 $\mu C/cm^2$
5. Development
   - ZED N50 for 2.5min
   - MIBK for 30s

- N_2 blow dry
- O_2 plasma ash at 150W, 12sccm O_2 flow for 2min

6. E-beam Evaporation of Au with Cr Adhesion layer
    - Evaporate 10nm thick Cr at 0.2nm/s
    - Evaporate 110nm thick Au at 0.2nm/s
7. Liftoff
    - NMP at 150°C for 2hr
    - Acetone 5min sonication
    - IPA 5min sonication
    - N_2 blow dry
    - O_2 plasma ash at 150W, 12sccm O_2 flow for 2min
8. LN Etch
    - Concentrated (49%) HF for 3min
    - Water
    - 70°C SC1 for 15min
    - Water
    - N_2 blow dry

11.2 Protection of LN Adhesion Layer

Growth of thin film LN is not possible without severe damage to the substrate. The method of depositing thin film LN on silicon is to bond a bulk LN crystal to the substrate followed by dicing of the remaining bulk crystal. This technique requires robust adhesion between LN and silicon. LN and silicon do not naturally adhere to each other so to promote adhesion we infer the proprietary process developed by the manufacturer utilizes a thin oxide layer between the LN and silicon. Our silicon on insulator (SOI) substrate requires hydrofluoric (HF) acid processing to mechanically suspend our mechanical structures. This HF processing reacts with the LN-Si adhesion layer resulting in liftoff of our LN features. To avoid this we have added a thin capping layer over the LN to prevent this. There are two challenges with this approach. One, the capping layer will add distance between the electric (electrodes) and mechanical fields (piezo cavity) reducing the integrated

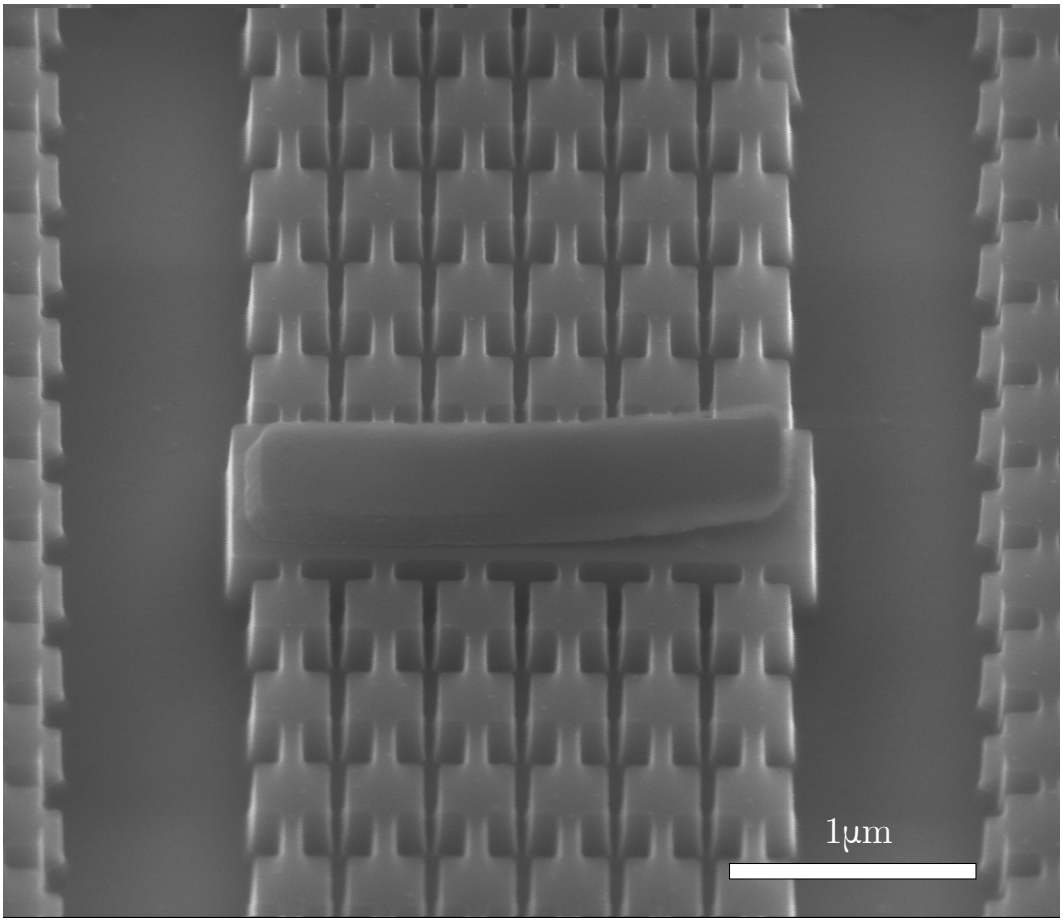

Figure 11.3: **Delaminated LN box.**
Any HF processing following the etching of the LN box will result in the box delaminating from the substrate. In the case seen in this image the box is lifting up on the right side, but remains partially anchored.

field overlap resulting in a diminished piezoelectric coupling. A thin capping layer is required to maintain large coupling, but must also be robust enough to protect the interface layer during HF processing. And second, the dielectric and mechanical loss properties of capping material are integral to maintaining high Q cavities as it will be subject to large electric and mechanical fields. Atomic layer deposited (ALD) Al_2O_3 (alumina) was selected to satisfy these requirements. We have demonstrated experimentally films thinner than 4nm do not sufficiently protect the boxes while capping films thicker than a few nanometers substantially impact the Q factor and piezoelectric coupling of the cavity. In our experiments we have settled on a 4nm thick thermal ALD alumina process following the definition of the LN box. To adequately protect the box from this problem we need to add one more step. The primary benefit of the HF + SC1 wet etch is that it does not etch this adhesion layer,

leaving the box in place following the etch. However, if we place the capping layer immediately on top of the box following the SC1 etch the box will not be protected as the capping layer will be on top of the adhesion layer. This will make the boxes vulnerable to the same undercutting problem we saw in the past. To prevent this we will need to remove the adhesion layer around the box. This step needs to be thought through carefully if we want to maintain the adhesion layer underneath the box while removing it around the box. A wet etch is not likely to allow for precise control of lateral etching while a dry etch will allow for better control, but will damage the silicon underneath. To mitigate these issues we have experimented with a small trench etched around the box to expose the silicon without damaging the key regions where the optomechanical crystal will be. Several etch chemistries

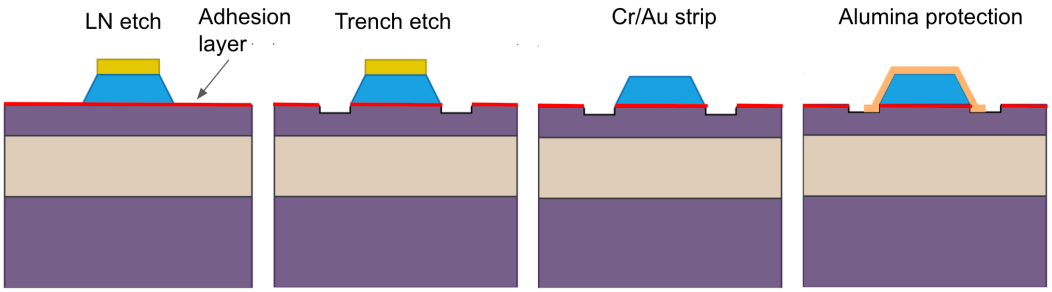

Figure 11.4: **Proposed hybrid etch process for LN.**

were experimented for finding the best trench etch. Ideally we can find a chemistry which selectively etches the adhesion layer while leaving the LN box undamaged. We tried three chemistries: C_4F_8/O_2, SF_6, and Ar. We found C_4F_8/O_2 chemistry did not etch the adhesion layer at all. SF_6 did etch the adhesion layer, but also began to undercut the boxes as seen in 11.5. The result of the Ar etch was difficult to determine because of hardened organics which were not removable. At this point the fluorine chemistries did not seem promising so we proceeded with the Ar etch. We tested the etch again, but this time using a bi-layer resist which should be more resilient to resist hardening.

With this bi-layer Ar tench etch we found the walls of the boxes were slightly roughened, but otherwise the integrity of the LN was maintained. Next we moved on to the alumina capping layer. We did not have any trouble with the atomic layer deposition (ALD) process, but found the etching of the capping layer to be non-trivial. We began by etching the alumina with phosphouric acid which will selectively etch the capping layer, but not attack the underlying silicon. We found resist masks would not adequately hold up to this wet etch which resulted

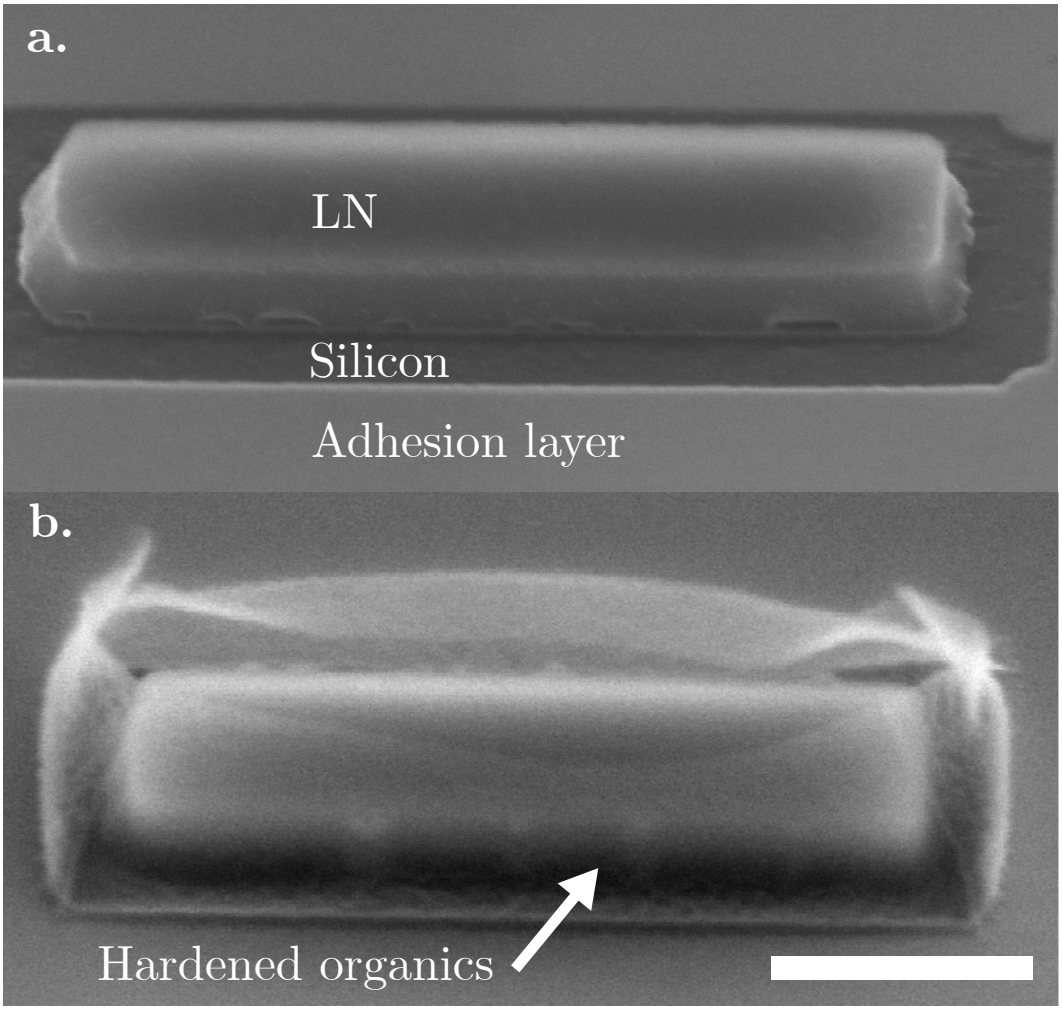

Figure 11.5: **Trench etch. a.** SF_6 chemistry reactive ion etch shown. At the bottom of the LN box small cavities appear. These cavities indicate the SF6 chemistry is undercutting the box. **b.** Ar chemistry etch shown. This etch left behind segments of the organic resist used to pattern the trench. The hardened organics are not able to be removed without damaging the box or substrate. Scale bar for both images is 1μm.

in inconsistent dimensions of the capping layer. Typically to resolve sub-micron features with a wet etch a hard mask is required. To overcome this issue we moved this process to a silicon dioxide hard mask. The hard mask is etched with C_4F_8/O_2 dry etch and can be readily removed with vapor HF following processing.

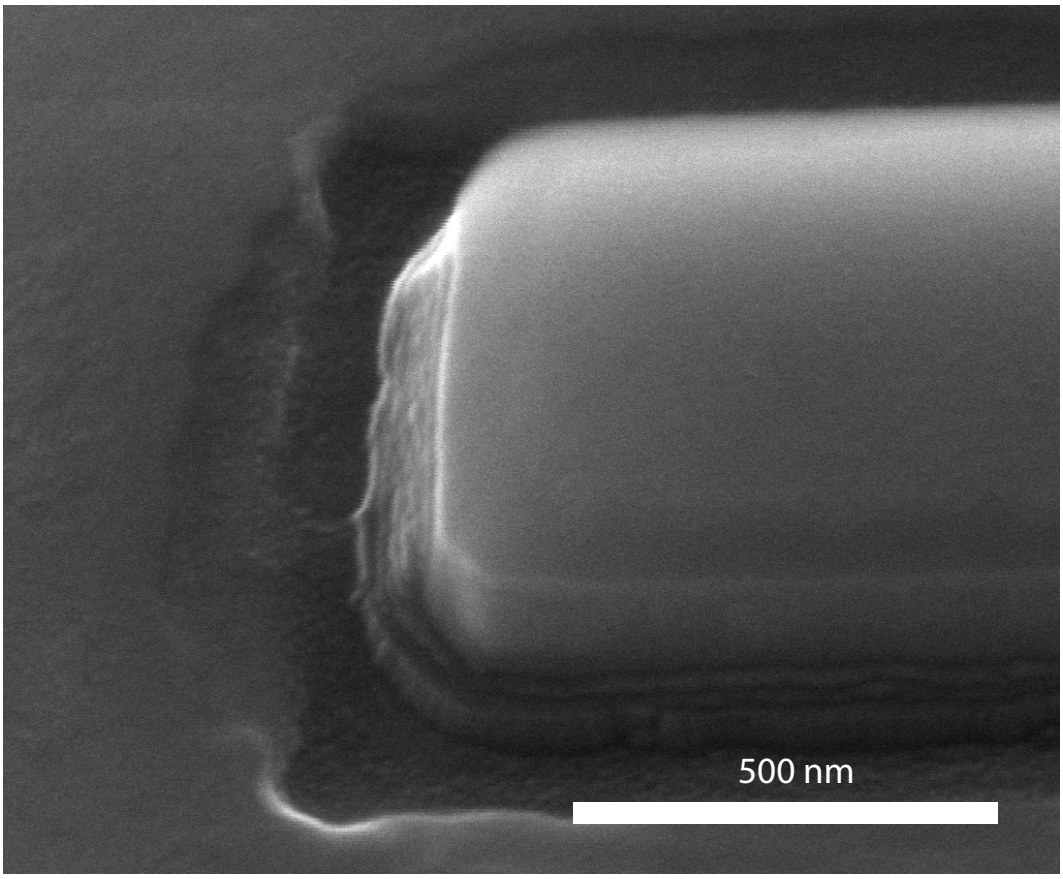

Figure 11.6: **Argon trench with bi-layer resist.** In this Ar trench etch the bi-layer resist yielded much better results with no resist hardening effects.

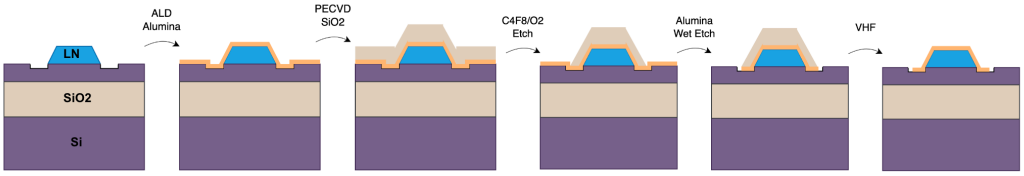

Figure 11.7: **Oxide mask process.** In this process we will use a phosphoric acid wet etch with a silicon dioxide hard mask then remove the mask with VHF following the alumina etch.

Chapter 12

LN TRANSDUCER MEASUREMENTS

12.1 Direct Coupled Device Fabrication

The first stage of measurement to ensure the efficient operation of our LN piezoacoustic cavities is to measure the electrical response at room temperature. LN boxes were fabricated using the following procedure: **Layer 1: Markers and LN Mask.**

1. Chip Cleaning
   - Acetone 5min sonication
   - IPA 5min sonication
   - N_2 blow dry
   - O_2 plasma ash at 150W, 12sccm O_2 flow for 2min
   - 15s dip in 10:1 Buffered HF (BHF) followed by 2x 10s DI H_20 rinse
2. Spin on Conductive Layer for E-beam Lithography
   - Spin on AquaSave at 2200 rpm for 1 min
3. Spin/Bake ZEP 520a
   - Pre-bake at 180°C for 3min
   - Spin ZEP 520a at 3000 rpm for 1 min
   - Post-bake at 180°C for 3min
4. E-Beam Lithography
   - Beam current 50nA
   - Fracturing resolution 20nm
   - Dose 230 $\mu C/cm^2$
5. Development
   - ZED N50 for 2.5min

- MIBK for 30s
- N_2 blow dry
- O_2 plasma ash at 150W, 12sccm O_2 flow for 2min

6. E-beam Evaporation of Au with Cr Adhesion layer
   - Evaporate 10nm thick Cr at 0.2nm/s
   - Evaporate 110nm thick Au at 0.2nm/s
7. Liftoff
   - NMP at 150°C for 2hr
   - Acetone 5min sonication
   - IPA 5min sonication
   - N_2 blow dry
   - O_2 plasma ash at 150W, 12sccm O_2 flow for 2min
8. LN Etch
   - Concentrated (49%) HF for 3min
   - H_2O for 1min
   - 70°C SC1 for 15min
   - H_2O for 1min
   - N_2 blow dry

Layer 2: LN Mask Removal and Trench Etch. Now that we have defined our LN boxes the gold mask can be removed, but we will continue to use the gold markers for layer alignment. We will use this layer to selectively remove the LN mask while leaving behind the gold markers. We will also use this layer to define the small trench surrounding the LN box to allow for adequate capping to prevent delamination during subsequent steps. We found reactive ion etching (RIE) with argon to etch through the adhesion layer to be the most controllable method. RIE with Ar is known to make exposed organic resist films difficult to strip, to avoid this issue we have implemented a bi-layer resist process which allows for easier stripping.

1. Chip Cleaning

- O_2 plasma ash at 150W, 12sccm O_2 flow for 2min

2. Spin on Resist Adhesion Layer
   - Pre-bake at 170°C for 3min
   - Spin on SurPass 3000 at 3000 rpm for 1 min
3. Spin/Bake MAA EL 11
   - Spin MAA EL 11 at 2200 rpm for 1 min
   - Post-bake at 170°C for 3min
4. Spin/Bake 950 PMMA A4
   - Spin 950 PMMA A4 at 2200 rpm for 1 min
   - Post-bake at 170°C for 3min
5. E-Beam Lithography
   - Beam current 1nA
   - Fracturing resolution 2nm
   - Dose 450 $\mu C/cm^2$
6. Cold Development
   - 1:3 H_2O:IPA at 1°C for 10min
   - IPA at 1°C for 10s
   - N_2 blow dry
7. Argon Etch
   - 30 sccm Ar 30W RF, 300W ICP power
   - O_2 plasma ash at 150W, 12sccm O_2 flow for 2min
8. Chrome + Gold Etch
   - Transene gold etch TFA for 3min
   - H_2O for 30s
   - Transene chrome etch 1020AC for 45s
   - H_2O for 30s

- N_2 blow dry

9. Resist Strip
    - NMP at 150°C for 2hr
    - Acetone 5min sonication
    - IPA 5min sonication
    - N_2 blow dry
    - O_2 plasma ash at 150W, 12sccm O_2 flow for 2min

Layer 3: Alumina Capping. In this layer we use atomic layer deposition (ALD) to grow a low-loss thin alumina (Al_2O_3) capping layer. To etch the capping layer we use a wet etch with a silicon dioxide (SiO_2) mask.

1. ALD Alumina
    - Thermal ALD at 150°C with TMA and H_2O precursors for 100 cycles
2. SiO_2 Mask
    - Plasma enhanced chemical vapor deposition (PECVD) at 350°C of SiO_2 for 2min
    - O_2 plasma ash at 150W, 12sccm O_2 flow for 2min
3. Spin/Bake ZEP 520a
    - Pre-bake at 180°C for 3min
    - Spin ZEP 520a at 3000 rpm for 1 min
    - Post-bake at 180°C for 3min
4. E-Beam Lithography
    - Beam current 50nA
    - Fracturing resolution 20nm
    - Dose 230 $\mu C/cm^2$
5. Development
    - ZED N50 for 2.5min

- MIBK for 30s
- N_2 blow dry

6. SiO_2 Etch
   - C_4F_8:O_2 40:3 sccm 33W RF, 1300W ICP power
7. Resist Strip
   - NMP at 150°C for 2hr
   - Acetone 5min sonication
   - IPA 5min sonication
   - N_2 blow dry
   - O_2 plasma ash at 150W, 12sccm O_2 flow for 2min
8. Alumina Etch
   - Transene Alumina Etchant Type A at 45°C for 4min
   - H_2O for 30s
   - N_2 blow dry
9. SiO_2 Strip
   - Vapor HF 1 cycle
   - O_2 plasma ash at 150W, 12sccm O_2 flow for 2min

Layer 4: Silicon Etch

1. Spin/Bake ZEP 520a
   - Pre-bake at 180°C for 3min
   - Spin ZEP 520a at 8000 rpm for 1 min
   - Post-bake at 180°C for 3min
2. E-Beam Lithography
   - Beam current 150pA
   - Fracturing resolution 1nm

- Dose 220 $\mu C/cm^2$

3. Development

   - ZED N50 for 2.5min
   - MIBK for 30s
   - N_2 blow dry

4. Si Etch

   - C_4F_8:SF_6 72:30 sccm 18W RF, 600W ICP power

5. Resist Strip

   - NMP at 150°C for 2hr
   - Acetone 5min sonication
   - IPA 5min sonication
   - N_2 blow dry
   - O_2 plasma ash at 150W, 12sccm O_2 flow for 2min

Layer 5: Aluminum Liftoff. The evaporation is separated into three steps with two angled steps to coat the steep sidewalls of the LN box.

1. Spin/Bake ZEP 520a

   - Pre-bake at 180°C for 3min
   - Spin ZEP 520a at 3000 rpm for 1 min
   - Post-bake at 180°C for 3min

2. E-Beam Lithography

   - Beam current 1nA
   - Fracturing resolution 2nm
   - Dose 250 $\mu C/cm^2$

3. Development

   - ZED N50 for 2.5min
   - MIBK for 30s

- N_2 blow dry
- O_2 plasma ash at 150W, 12sccm O_2 flow for 2min

4. Aluminum Evaporation
    - 20nm 60° angled aluminum evaporation at 0.3nm/s
    - 20nm -60° angled aluminum evaporation at 0.3nm/s
    - 60nm aluminum evaporation at 0.3nm/s
5. Liftoff
    - NMP at 150°C for 2hr
    - Acetone 5min sonication
    - IPA 5min sonication
    - N_2 blow dry
    - O_2 plasma ash at 150W, 12sccm O_2 flow for 2min

Vapor HF Release

12.2 Direct Coupled Microwave Measurement

Following the development of a successful process we fabricate direct coupled LN mechanical transducers. These devices are used as a model to determine the piezoelectric coupling rate and yield of our process without the added complexity of optomechanical crystals which are needed for the full microwave to optical transducer. Instead of electrical coupling to the piezo-cavity via a superconducting microwave resonator we implement direct coupling to microwave feedline waveguides. This design change allows for spectroscopy of the mechanical modes at room temperature, but will reduce our effective piezoelectric coupling as a function of the electrical impedance which the piezo-caivty is situated in. In the case of our microwave-to-optical transducer, we have designed a microwave circuit with high electrical impedance to increase our piezo coupling, but in the case of a direct coupled device we are limited to 50Ω. Practically, this means our piezo-cavities which we would expect 10s of MHz coupling to a superconducting resonator will have kHz coupling in the direct coupled device. By knowing the impedance of both the direct coupled environment as well as our supercondicting circuits we can use a Butterworth-Van Dyke (BVD) circuit model we fit our data to extract the expected piezoelectric coupling rate. We couple our vector network analyzer (VNA) to the

transducer via large aluminum pads which are directly connected to the transducer. We found this process to be a significant improvement in terms of device yield, but

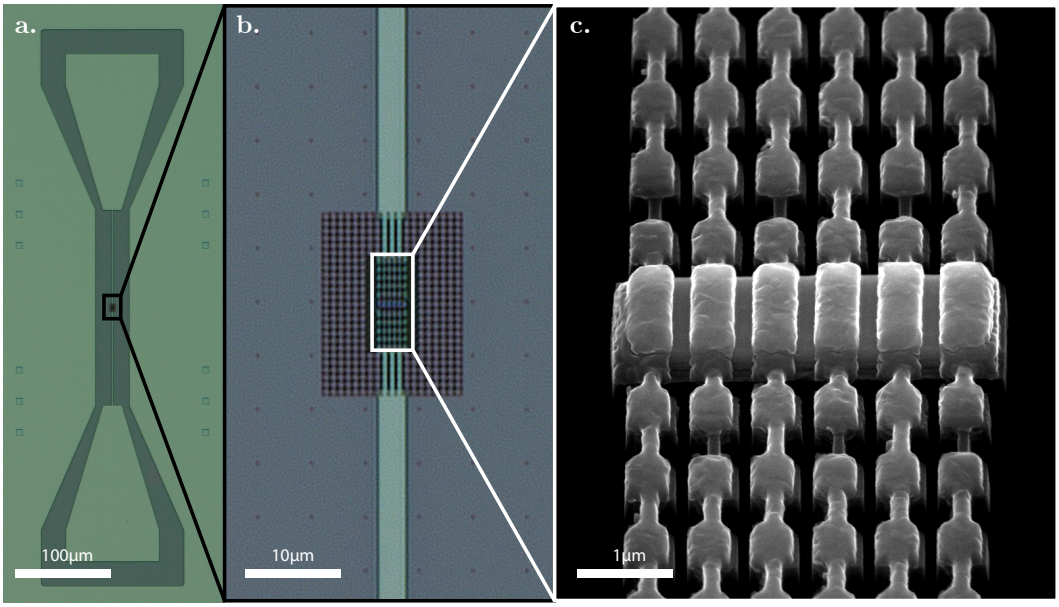

Figure 12.1: **Direct coupled transducer. a.** Optical microscope image of direct coupled LN transducer where the device is measured in microwave transmission spectroscopy to determine piezoelectric coupling. **b.** Optical microscope image at higher magnification showing piezoelectric transducer with phononic shield surrounding to reduce mechanical clamping loss. **c.** Scanning electron microscope image of piezo-acoustic cavity. Rectangle in the center of the image is LN with aluminum electrodes climbing over the piezo-cavity forming an interdigitated transducer.

the piezoelectric coupling rate measured was lower than expected according to our previous measurements of LN transducers. In past devices the fabrication procedure use resulted in a device yield of about 30% whereas with this new process we have a yield of 70%. However we also found the coupling numbers extracted using the BVD fit were about a factor of two lower than previous measurements with similar LN transducers with different fabrication procedures. To determine this we decided to continue fabrication, but this time with transducers with optical devices and more on a single chip such that statistics of the coupling could be extracted.

12.3 DC Room Temperature Transduction

Following the direct coupled microwave measurements we fabricate a new device with an optomechanical crystal (OMC) coupled to the piezo cavity. In addition to measuring more yield and coupling statistics, we are also experimentally verifying the mechanical hybridization between the piezoacoustic cavity and the OMC. As discussed in Chapter 2 the hybridization impacts the noise and efficiency and must be experimentally verified. Additionally, the hybridization is sensitive to fabrication

disorder. To explore the appropriate hybridization window we will sweep the dimensions of both the piezo cavity and the OMC cavity. With a two dimensional parameter sweep we will be able to identify the design for optimal OMC-piezo hybridization. Plotting the microwave spectroscopy data from these devices we

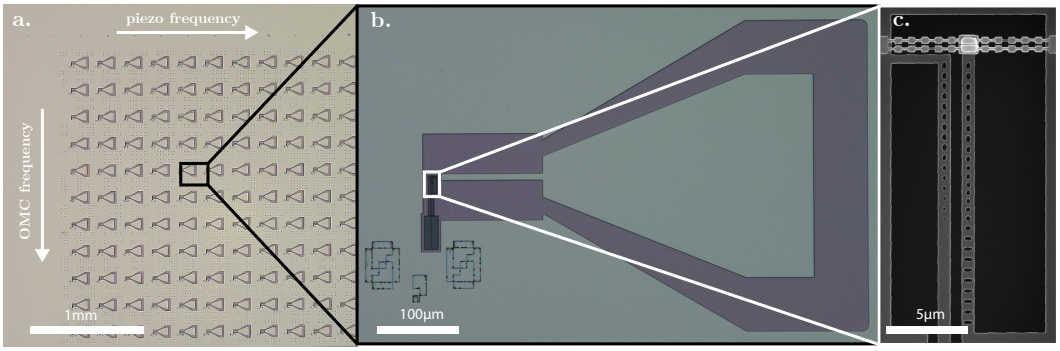

Figure 12.2: **Direct coupled transducer with OMC. a.** Optical microscope image of array of direct coupled LN transducer where the device is measured in microwave reflection spectroscopy and optical reflection spectoscopy. **b.** Optical microscope image at higher magnification showing piezoelectric transducer. **c.** Scanning electron microscope image of piezo-acoustic cavity with attached OMC. The photonic crystal structure to the left of the OMC is a mirror which allows us to effectively couple light in and out of the optical cavity.

can notice several trends related to the piezoelectric coupling. First we can see a large peak around zero g_{pe} indicating there are many devices with coupling much lower than expected and another peak at 5 MHz which is closer to the expected value. We can also look at the trend of frequency with respect to g_{pe} and g_{OM} and we can see there is not a strong correlation between mechanical frequency and optimal hybridization. In other words, modes which share large g_{pe} and g_{OM} do not bunch around a specific frequency. This indicates our design has a broad hybridization window. What we also found from this experiment is that our average piezoelectric coupling was much lower than expected from previous measurements. Compared to the previous measurements the PECVD oxide mask was the main different. We fabricated and measured surface acoustic wave (SAW) transducers to determine the effect of the various added processing steps. SAW devices do not require patterning of LN which makes them much easier to fabricate, but will still allow us to measure relative changes to the piezoelectricity due to processing steps. We tested several steps in isolation on the SAW devices to determine the relative effect on the transducer devices. We tested O_2 plasma cleaning, thermal cycling to the temperature required for PECVD (350°C), vapor HF and PECVD + vapor HF. We found the O_2 plasma and vapor HF has negligible effect on the piezoelectric properties of the film. However, thermal cycling and PECVD + vapor

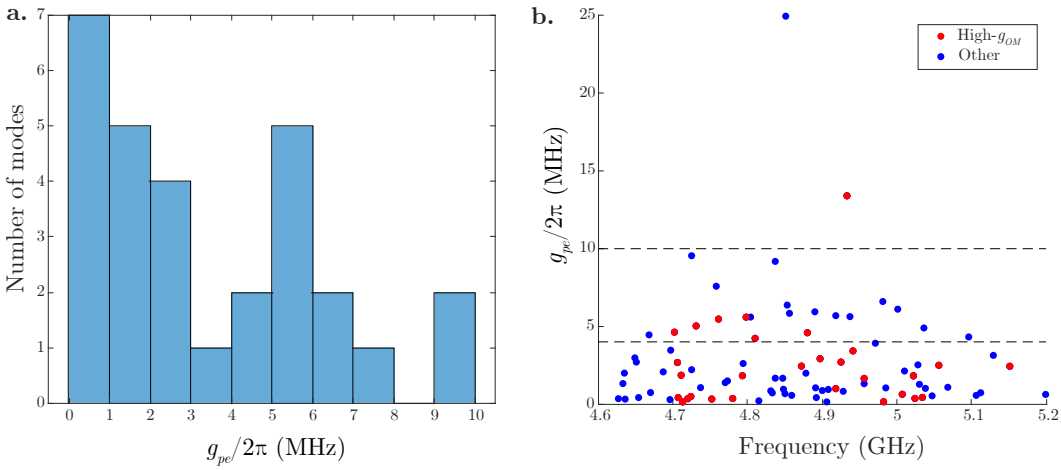

Figure 12.3: **Piezoelectric coupling statistics. a.** Histogram plotting the frequency of devices with a rang of piezoelectric coupling. There is a large peak around zero and another peak around 5 MHz. **b.** Scatter plot of piezoelectric coupling vs mode frequency used to determine optimal mechanical hybridization point. Red points are highlighted as modes which also have large optomechanical coupling relative to other modes.

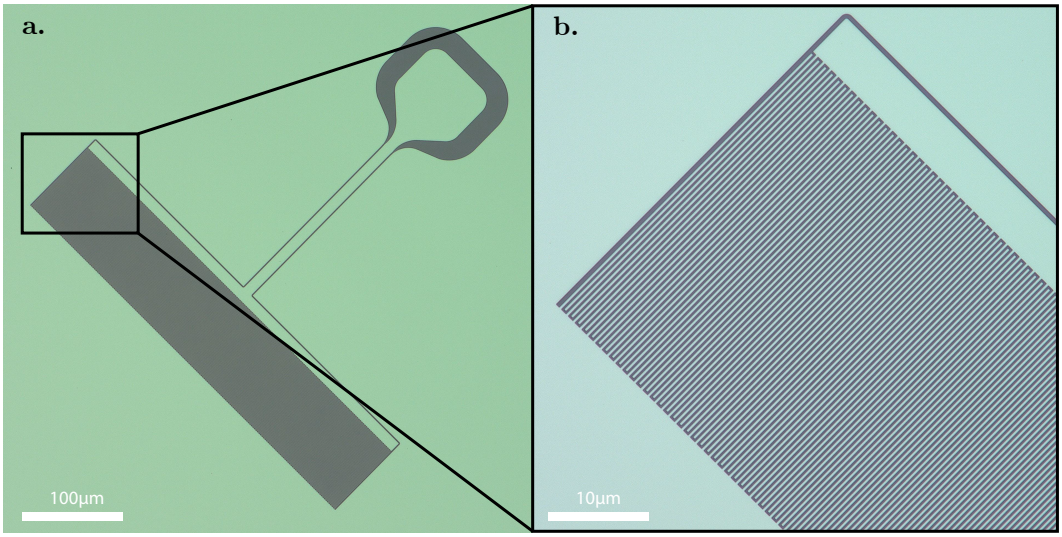

Figure 12.4: **LN surface acoustic wave (SAW) transducer. a.** Optical microscope image of SAW device connected to a landing pad to interface with a microwave probe. **b.** Higher magnification optical microscope image of the device seen in **a.** The individual finges comprising the SAW are seen. The pitch of the fingers sets the frequency and the length determines the piezoelectric coupling rate.

HF led to a substantial reduction in measured piezoelectric coupling by 20% and 40%, respectively. This result is discouraging for use of PECVD oxide during our process. The alternative of using an organic resist mask which does not require extra processing steps is also not an option.

Chapter 13

OUTLOOK

While LN transducers are very promising in terms of efficiency and added noise, there are many other factors to consider. The remaining challenges that face the development of LN transducers, yield for example, are great and will require significant effort to overcome. In the near-term our transducer efforts have focused on the development of AlN devices, but the next generation LN transducers will bring large leaps in device performance.

BIBLIOGRAPHY

[1] B. T. Gard, K. Jacobs, R. McDermott, and M. Saffman. "Microwave-to-optical frequency conversion using a cesium atom coupled to a superconducting resonator". In: *Phys. Rev. A* 96.1 (2017), p. 013833.

[2] J. Han, T. Vogt, C. Gross, D. Jaksch, M. Kiffner, and W. Li. "Coherent microwave-to-optical conversion via six-wave mixing in Rydberg atoms". In: *Phys. Rev. Lett.* 120.9 (2018), p. 093201.

[3] T. Vogt, C. Gross, J. Han, S. B. Pal, M. Lam, M. Kiffner, and W. Li. "Efficient microwave-to-optical conversion using Rydberg atoms". In: *Phys. Rev. A* 99.2 (2019), p. 023832.

[4] L. A. Williamson, Y.-H. Chen, and J. J. Longdell. "Magneto-optic modulator with unit quantum efficiency". In: *Phys. Rev. Lett.* 113.20 (2014), p. 203601.

[5] X. Fernandez-Gonzalvo, Y.-H. Chen, C. Yin, S. Rogge, and J. J. Longdell. "Coherent frequency up-conversion of microwaves to the optical telecommunications band in an Er: YSO crystal". In: *Phys. Rev. A* 92.6 (2015), p. 062313.

[6] X. Fernandez-Gonzalvo, S. P. Horvath, Y.-H. Chen, and J. J. Longdell. "Cavity-enhanced Raman heterodyne spectroscopy in Er^{3+}: Y_2SiO_5 for microwave to optical signal conversion". In: *Phys. Rev. A* 100.3 (2019), p. 033807.

[7] J. G. Bartholomew, J. Rochman, T. Xie, J. M. Kindem, A. Ruskuc, I. Craiciu, M. Lei, and A. Faraon. "On-chip coherent microwave-to-optical transduction mediated by ytterbium in YVO_4". In: *Nat. Commun.* 11.1 (2020), pp. 1–6.

[8] C. Javerzac-Galy, K. Plekhanov, N. R. Bernier, L. D. Toth, A. K. Feofanov, and T. J. Kippenberg. "On-chip microwave-to-optical quantum coherent converter based on a superconducting resonator coupled to an electro-optic microresonator". In: *Phys. Rev. A* 94.5 (2016), p. 053815.

[9] M. Soltani, M. Zhang, C. Ryan, G. J. Ribeill, C. Wang, and M. Loncar. "Efficient quantum microwave-to-optical conversion using electro-optic nanophotonic coupled resonators". In: *Phys. Rev. A* 96.4 (2017), p. 043808.

[10] A. Rueda, W. Hease, S. Barzanjeh, and J. M. Fink. "Electro-optic entanglement source for microwave to telecom quantum state transfer". In: *npj Quantum Inf.* 5.1 (2019), pp. 1–11.

[11] A. Rueda, F. Sedlmeir, M. C. Collodo, U. Vogl, B. Stiller, G. Schunk, D. V. Strekalov, C. Marquardt, J. M. Fink, O. Painter, et al. "Efficient microwave to optical photon conversion: an electro-optical realization". In: *Optica* 3.6 (2016), pp. 597–604.

[12] L. Fan, C.-L. Zou, R. Cheng, X. Guo, X. Han, Z. Gong, S. Wang, and H. X. Tang. "Superconducting cavity electro-optics: a platform for coherent photon conversion between superconducting and photonic circuits". In: *Sci. Adv.* 4.8 (2018), eaar4994.

[13] W. Fu, M. Xu, X. Liu, C.-L. Zou, C. Zhong, X. Han, M. Shen, Y. Xu, R. Cheng, S. Wang, et al. "Cavity electro-optic circuit for microwave-to-optical conversion in the quantum ground state". In: *Phys. Rev. A* 103.5 (2021), p. 053504.

[14] J. Holzgrafe, N. Sinclair, D. Zhu, A. Shams-Ansari, M. Colangelo, Y. Hu, M. Zhang, K. K. Berggren, and M. Lončar. "Cavity electro-optics in thin-film lithium niobate for efficient microwave-to-optical transduction". In: *Optica* 7.12 (2020), pp. 1714–1720.

[15] T. P. McKenna, J. D. Witmer, R. N. Patel, W. Jiang, R. Van Laer, P. Arrangoiz-Arriola, E. A. Wollack, J. F. Herrmann, and A. H. Safavi-Naeini. "Cryogenic microwave-to-optical conversion using a triply resonant lithium-niobate-on-sapphire transducer". In: *Optica* 7.12 (2020), pp. 1737–1745.

[16] A. H. Safavi-Naeini and O. Painter. "Proposal for an optomechanical traveling wave phonon–photon translator". In: *New J. Phys.* 13.1 (2011), p. 013017.

[17] K. Stannigel, P. Rabl, A. S. Sørensen, P. Zoller, and M. D. Lukin. "Optomechanical transducers for long-distance quantum communication". In: *Phys. Rev. Lett.* 105.22 (2010), p. 220501.

[18] S. Barzanjeh, M. Abdi, G. J. Milburn, P. Tombesi, and D. Vitali. "Reversible optical-to-microwave quantum interface". In: *Phys. Rev. Lett.* 109.13 (2012), p. 130503.

[19] T. Bagci, A. Simonsen, S. Schmid, L. G. Villanueva, E. Zeuthen, J. Appel, J. M. Taylor, A. Sørensen, K. Usami, A. Schliesser, et al. "Optical detection of radio waves through a nanomechanical transducer". In: *Nature* 507.7490 (2014), pp. 81–85.

[20] R. W. Andrews, R. W. Peterson, T. P. Purdy, K. Cicak, R. W. Simmonds, C. A. Regal, and K. W. Lehnert. "Bidirectional and efficient conversion between microwave and optical light". In: *Nat. Phys.* 10.4 (2014), pp. 321–326.

[21] A. P. Higginbotham, P. S. Burns, M. D. Urmey, R. W. Peterson, N. S. Kampel, B. M. Brubaker, G. Smith, K. W. Lehnert, and C. A. Regal. "Harnessing electro-optic correlations in an efficient mechanical converter". In: *Nat. Phys.* 14.10 (2018), pp. 1038–1042.

[22] J. Bochmann, A. Vainsencher, D. D. Awschalom, and A. N. Cleland. "Nanomechanical coupling between microwave and optical photons". In: *Nat. Phys.* 9.11 (2013), pp. 712–716.

[23] K. C. Balram, M. I. Davanço, J. D. Song, and K. Srinivasan. "Coherent coupling between radiofrequency, optical and acoustic waves in piezo-optomechanical circuits". In: *Nat. Photonics* 10.5 (2016), pp. 346–352.

[24] M. Forsch, R. Stockill, A. Wallucks, I. Marinković, C. Gärtner, R. A. Norte, F. van Otten, A. Fiore, K. Srinivasan, and S. Gröblacher. "Microwave-to-optics conversion using a mechanical oscillator in its quantum ground state". In: *Nat. Phys.* 16.1 (2020), pp. 69–74.

[25] W. Jiang, C. J. Sarabalis, Y. D. Dahmani, R. N. Patel, F. M. Mayor, T. P. McKenna, R. Van Laer, and A. H. Safavi-Naeini. "Efficient bidirectional piezo-optomechanical transduction between microwave and optical frequency". In: *Nat. Commun.* 11.1 (2020), pp. 1–7.

[26] W. Jiang, R. N. Patel, F. M. Mayor, T. P. McKenna, P. Arrangoiz-Arriola, C. J. Sarabalis, J. D. Witmer, R. Van Laer, and A. H. Safavi-Naeini. "Lithium niobate piezo-optomechanical crystals". In: *Optica* 6.7 (2019), pp. 845–853.

[27] A. Vainsencher, K. J. Satzinger, G. A. Peairs, and A. N. Cleland. "Bi-directional conversion between microwave and optical frequencies in a piezoelectric optomechanical device". In: *Appl. Phys. Lett.* 109.3 (2016), p. 033107.

[28] L. Shao, M. Yu, S. Maity, N. Sinclair, L. Zheng, C. Chia, A. Shams-Ansari, C. Wang, M. Zhang, K. Lai, et al. "Microwave-to-optical conversion using lithium niobate thin-film acoustic resonators". In: *Optica* 6.12 (2019), pp. 1498–1505.

[29] X. Han, W. Fu, C. Zhong, C.-L. Zou, Y. Xu, A. Al Sayem, M. Xu, S. Wang, R. Cheng, L. Jiang, et al. "Cavity piezo-mechanics for superconducting-nanophotonic quantum interface". In: *Nat. Commun.* 11.1 (2020), pp. 1–8.

[30] M. Mirhosseini, A. Sipahigil, M. Kalaee, and O. Painter. "Superconducting qubit to optical photon transduction". In: *Nature* 588.7839 (2020), pp. 599–603.

[31] M. Aspelmeyer, T. J. Kippenberg, and F. Marquardt. "Cavity optomechanics". In: *Rev. Mod. Phys.* 86.4 (2014), p. 1391.

[32] T. J. Kippenberg and K. J. Vahala. "Cavity opto-mechanics". In: *Opt. Express* 15.25 (2007), pp. 17172–17205.

[33] J. Chan, A. H. Safavi-Naeini, J. T. Hill, S. Meenehan, and O. Painter. "Optimized optomechanical crystal cavity with acoustic radiation shield". In: *Appl. Phys. Lett.* 101.8 (2012), p. 081115.

[34] A. H. Safavi-Naeini and O. Painter. "Optomechanical crystal devices". In: *Cavity Optomechanics*. Springer, 2014, pp. 195–231.

[35] S. M. Meenehan, J. D. Cohen, S. Gröblacher, J. T. Hill, A. H. Safavi-Naeini, M. Aspelmeyer, and O. Painter. "Silicon optomechanical crystal resonator at millikelvin temperatures". In: *Phys. Rev. A* 90.1 (2014), p. 011803.

[36] J. D. Cohen, S. M. Meenehan, G. S. MacCabe, S. Gröblacher, A. H. Safavi-Naeini, F. Marsili, M. D. Shaw, and O. Painter. "Phonon counting and intensity interferometry of a nanomechanical resonator". In: *Nature* 520.7548 (2015), pp. 522–525.

[37] S. M. Meenehan, J. D. Cohen, G. S. MacCabe, F. Marsili, M. D. Shaw, and O. Painter. "Pulsed excitation dynamics of an optomechanical crystal resonator near its quantum ground state of motion". In: *Phys. Rev. X* 5.4 (2015), p. 041002.

[38] K. W. Murch, K. L. Moore, S. Gupta, and D. M. Stamper-Kurn. "Observation of quantum-measurement backaction with an ultracold atomic gas". In: *Nat. Phys.* 4.7 (2008), pp. 561–564.

[39] F. Brennecke, S. Ritter, T. Donner, and T. Esslinger. "Cavity optomechanics with a Bose-Einstein condensate". In: *Science* 322.5899 (2008), pp. 235–238.

[40] O. Arcizet, P.-F. Cohadon, T. Briant, M. Pinard, and A. Heidmann. "Radiation-pressure cooling and optomechanical instability of a micromirror". In: *Nature* 444.7115 (2006), pp. 71–74.

[41] I. Favero, C. Metzger, S. Camerer, D. König, H. Lorenz, J. P. Kotthaus, and K. Karrai. "Optical cooling of a micromirror of wavelength size". In: *Appl. Phys. Lett.* 90.10 (2007), p. 104101.

[42] S. Gigan, H. R. Böhm, M. Paternostro, F. Blaser, G. Langer, J. B. Hertzberg, K. C. Schwab, D. Bäuerle, M. Aspelmeyer, and A. Zeilinger. "Self-cooling of a micromirror by radiation pressure". In: *Nature* 444.7115 (2006), pp. 67–70.

[43] G. S. MacCabe, H. Ren, J. Luo, J. D. Cohen, H. Zhou, A. Sipahigil, M. Mirhosseini, and O. Painter. "Nano-acoustic resonator with ultralong phonon lifetime". In: *Science* 370.6518 (2020), pp. 840–843.

[44] D. K. Biegelsen. "Frequency dependence of the photoelastic coefficients of silicon". In: *Phys. Rev. B* 12.6 (1975), p. 2427.

[45] B. J. Frey, D. B. Leviton, and T. J. Madison. "Temperature-dependent refractive index of silicon and germanium". In: *Optomechanical Technologies for Astronomy*. Vol. 6273. International Society for Optics and Photonics. 2006, 62732J.

[46] N. Samkharadze, A. Bruno, P. Scarlino, G. Zheng, D. P. DiVincenzo, L. DiCarlo, and L. M. K. Vandersypen. "High-kinetic-inductance superconducting nanowire resonators for circuit QED in a magnetic field". In: *Phys. Rev. Appl.* 5.4 (2016), p. 044004.

[47] V. Dimitrova, D. Manova, and E. Valcheva. “Optical and dielectric properties of dc magnetron sputtered AlN thin films correlated with deposition conditions”. In: *Materials Science and Engineering: B* 68.1 (1999), pp. 1–4. ISSN: 0921-5107. DOI: https://doi.org/10.1016/S0921-5107(99)00221-4.

[48] M. Mirhosseini, A. Sipahigil, M. Kalaee, and O. J. Painter. “Superconducting qubit to optical photon transduction”. In: *Nature* 588 (2020), pp. 599–603.

[49] J. A. Nelder and R. Mead. “A simplex method for function minimization”. In: *Comput. J.* 7.4 (1965), pp. 308–313.

[50] J. C. Lagarias, J. A. Reeds, M. H. Wright, and P. E. Wright. “Convergence properties of the Nelder–Mead simplex method in low dimensions”. In: *SIAM J. Optim.* 9.1 (1998), pp. 112–147.

[51] D. K. Biegelsen. “Photoelastic tensor of silicon and the volume dependence of the average gap”. In: *Phys. Rev. Lett.* 32.21 (1974), p. 1196.

[52] S. G. Johnson, M. Ibanescu, M. A. Skorobogatiy, O. Weisberg, J. Joannopoulos, and Y. Fink. “Perturbation theory for Maxwell’s equations with shifting material boundaries”. In: *Phys. Rev. E* 65.6 (2002), p. 066611.

[53] J. Chan. “Laser cooling of an optomechanical crystal resonator to its quantum ground state of motion”. PhD thesis. California Institute of Technology, 2012.

[54] E. A. Wollack, A. Y. Cleland, P. Arrangoiz-Arriola, T. P. McKenna, R. G. Gruenke, R. N. Patel, W. Jiang, C. J. Sarabalis, and A. H. Safavi-Naeini. “Loss channels affecting lithium niobate phononic crystal resonators at cryogenic temperature”. In: *Appl. Phys. Lett.* 118.12 (2021), p. 123501.

[55] A. Stesmans. “Passivation of P_{b0} and P_{b1} interface defects in thermal (100) Si/SiO_2 with molecular hydrogen”. In: *Appl. Phys. Lett.* 68.15 (1996), pp. 2076–2078.

[56] M. Borselli, T. J. Johnson, and O. Painter. “Measuring the role of surface chemistry in silicon microphotonics”. In: *Appl. Phys. Lett.* 88.13 (2006), p. 131114.

[57] A. Leo, G. Grimaldi, R. Citro, A. Nigro, S. Pace, and R. Huebener. “Quasiparticle scattering time in niobium superconducting films”. In: *Phys. Rev. B* 84.1 (2011), p. 014536.

[58] M. Johnson. “Direct real time measurement of quasiparticle lifetimes in a superconductor”. In: *Phys. Rev. Lett.* 67.3 (1991), p. 374.

[59] H. Ren, M. H. Matheny, G. S. MacCabe, J. Luo, H. Pfeifer, M. Mirhosseini, and O. Painter. “Two-dimensional optomechanical crystal cavity with high quantum cooperativity”. In: *Nat. Commun.* 11.1 (2020), pp. 1–10.

[60] J. M. Martinis, M. Ansmann, and J. Aumentado. “Energy decay in superconducting Josephson-junction qubits from nonequilibrium quasiparticle excitations”. In: *Phys. Rev. Lett.* 103.9 (2009), p. 097002.

[61] C. Wang, Y. Y. Gao, I. M. Pop, U. Vool, C. Axline, T. Brecht, R. W. Heeres, L. Frunzio, M. H. Devoret, G. Catelani, et al. “Measurement and control of quasiparticle dynamics in a superconducting qubit”. In: *Nat. Commun.* 5.1 (2014), pp. 1–7.

[62] R. Barends, J. J. A. Baselmans, S. J. C. Yates, J. R. Gao, J. N. Hovenier, and T. M. Klapwijk. “Quasiparticle relaxation in optically excited high-Q superconducting resonators”. In: *Phys. Rev. Lett.* 100.25 (2008), p. 257002.

[63] R. P. S. M. Lobo, J. D. LaVeigne, D. H. Reitze, D. B. Tanner, Z. H. Barber, E. Jacques, P. Bosland, M. J. Burns, and G. L. Carr. “Photoinduced time-resolved electrodynamics of superconducting metals and alloys”. In: *Phys. Rev. B* 72 (2 July 2005), p. 024510. DOI: 10.1103/PhysRevB.72.024510.

[64] S. B. Kaplan, C. C. Chi, D. N. Langenberg, J.-J. Chang, S. Jafarey, and D. J. Scalapino. “Quasiparticle and phonon lifetimes in superconductors”. In: *Phys. Rev. B* 14.11 (1976), p. 4854.

[65] D. C. Mattis and J. Bardeen. “Theory of the Anomalous Skin Effect in Normal and Superconducting Metals”. In: *Phys. Rev.* 111 (2 July 1958), pp. 412–417. DOI: 10.1103/PhysRev.111.412.

[66] M. Tinkham. *Introduction to superconductivity*. McGraw-Hill, 1996.

[67] M. R. Vissers, J. Hubmayr, M. Sandberg, S. Chaudhuri, C. Bockstiegel, and J. Gao. “Frequency-tunable superconducting resonators via nonlinear kinetic inductance”. In: *Applied Physics Letters* 107.6 (Aug. 2015), p. 062601. ISSN: 0003-6951. DOI: 10.1063/1.4927444. eprint: https://pubs.aip.org/aip/apl/article-pdf/doi/10.1063/1.4927444/14466852/062601_1_online.pdf.

[68] Y. Xu, A. A. Sayem, L. Fan, C.-L. Zou, S. Wang, R. Cheng, W. Fu, L. Yang, M. Xu, and H. X. Tang. “Bidirectional interconversion of microwave and light with thin-film lithium niobate”. In: *Nat. Commun.* 12.4453 (2021). DOI: 10.1038/s41467-021-24809-y.

[69] W. Fu, M. Xu, X. Liu, C.-L. Zou, C. Zhong, X. Han, M. Shen, Y. Xu, R. Cheng, S. Wang, L. Jiang, and H. X. Tang. “Cavity electro-optic circuit for microwave-to-optical conversion in the quantum ground state”. In: *Phys. Rev. A* 103 (5 May 2021), p. 053504. DOI: 10.1103/PhysRevA.103.053504.

[70] C. Zhong, Z. Wang, C. Zou, M. Zhang, X. Han, W. Fu, M. Xu, S. Shankar, M. H. Devoret, H. X. Tang, and L. Jiang. “Proposal for Heralded Generation and Detection of Entangled Microwave–Optical-Photon Pairs”. In: *Phys. Rev. Lett.* 124 (1 Jan. 2020), p. 010511. DOI: 10.1103/PhysRevLett.124.010511.

[71] M. D. Henry, S. Wolfley, T. Young, T. Monson, C. J. Pearce, R. Lewis, B. Clark, L. Brunke, and N. Missert. "Degradation of Superconducting Nb/NbN Films by Atmospheric Oxidation". In: *IEEE Transactions on Applied Superconductivity* 27.4 (2017), pp. 1–5. DOI: 10.1109/TASC.2017.2669583.

[72] M. J. Weaver, P. Duivestein, A. C. Bernasconi, S. Scharmer, M. Lemang, T. C. van Thiel, F. Hijazi, B. Hensen, S. Gröblacher, and R. Stockill. *An integrated microwave-to-optics interface for scalable quantum computing*. 2022. arXiv: 2210.15702.

[73] W. Jiang, C. J. Sarabalis, Y. D. Dahmani, R. N. Patel, F. M. Mayor, T. P. McKenna, R. Van Laer, and A. H. Safavi-Naeini. "Efficient bidirectional piezo-optomechanical transduction between microwave and optical frequency". In: *Nat. Commun.* 11.1 (Mar. 2020). ISSN: 2041-1723. DOI: 10.1038/s41467-020-14863-3.

[74] C. Zhong, Z. Wang, C. Zou, M. Zhang, X. Han, W. Fu, M. Xu, S. Shankar, M. H. Devoret, H. X. Tang, and L. Jiang. "Proposal for Heralded Generation and Detection of Entangled Microwave–Optical-Photon Pairs". In: *Phys. Rev. Lett.* 124 (1 Jan. 2020), p. 010511. DOI: 10.1103/PhysRevLett.124.010511.

[75] C. Zhong, X. Han, H. X. Tang, and L. Jiang. "Entanglement of microwave-optical modes in a strongly coupled electro-optomechanical system". In: *Phys. Rev. A* 101 (3 Mar. 2020), p. 032345. DOI: 10.1103/PhysRevA.101.032345.

[76] C. Zhong, X. Han, and L. Jiang. *Quantum transduction with microwave and optical entanglement*. 2022. arXiv: 2202.04601.

[77] J. Zmuidzinas. "Superconducting Microresonators: Physics and Applications". In: *Annu. Rev. Condens. Matter Phys.* 3.1 (2012), pp. 169–214. DOI: 10.1146/annurev-conmatphys-020911-125022.

[78] M. Xu, X. Han, W. Fu, C.-L. Zou, and H. X. Tang. "Frequency-tunable high-Q superconducting resonators via wireless control of nonlinear kinetic inductance". In: *Appl. Phys. Lett.* 114.19 (2019), p. 192601. DOI: 10.1063/1.5098466.

[79] In: *See supplementary information* ().

[80] C. Macklin, K. O'Brien, D. Hover, M. E. Schwartz, V. Bolkhovsky, X. Zhang, W. D. Oliver, and I. Siddiqi. "A near quantum-limited Josephson traveling-wave parametric amplifier". In: *Science* 350.6258 (2015), pp. 307–310. DOI: 10.1126/science.aaa8525.

[81] A. A. Clerk, M. H. Devoret, S. M. Girvin, F. Marquardt, and R. J. Schoelkopf. "Introduction to quantum noise, measurement, and amplification". In: *Rev. Mod. Phys.* 82 (2 Apr. 2010), pp. 1155–1208. DOI: 10.1103/RevModPhys.82.1155.

[82] C. M. Caves. "Quantum limits on noise in linear amplifiers". In: *Phys. Rev. D* 26 (8 Oct. 1982), pp. 1817–1839. DOI: 10.1103/PhysRevD.26.1817.

[83] C. Eichler, D. Bozyigit, C. Lang, L. Steffen, J. Fink, and A. Wallraff. "Experimental State Tomography of Itinerant Single Microwave Photons". In: *Phys. Rev. Lett.* 106 (22 June 2011), p. 220503. DOI: 10.1103/PhysRevLett.106.220503.

[84] S. M. Meenehan, J. D. Cohen, G. S. MacCabe, F. Marsili, M. D. Shaw, and O. Painter. "Pulsed excitation dynamics of an optomechanical crystal resonator near its quantum ground state of motion". In: *Phys. Rev. X* 5 (4 Oct. 2015), p. 041002. DOI: 10.1103/PhysRevX.5.041002.

[85] R. Riedinger, S. Hong, R. A. Norte, J. A. Slater, J. Shang, A. G. Krause, V. Anant, M. Aspelmeyer, and S. Gröblacher. "Non-classical correlations between single photons and phonons from a mechanical oscillator". In: *Nature* 530.7590 (Feb. 2016), pp. 313–316. ISSN: 1476-4687. DOI: 10.1038/nature16536.

[86] G. S. MacCabe, H. Ren, J. Luo, J. D. Cohen, H. Zhou, A. Sipahigil, M. Mirhosseini, and O. J. Painter. "Nano-acoustic resonator with ultralong phonon lifetime". In: *Science* 370.6518 (Nov. 2020), pp. 840–843. ISSN: 1095-9203. DOI: 10.1126/science.abc7312.

[87] J. F. Clauser. "Experimental distinction between the quantum and classical field-theoretic predictions for the photoelectric effect". In: *Phys. Rev. D* 9.4 (1974), p. 853.

[88] A. Kuzmich, W. P. Bowen, A. D. Boozer, A. Boca, C. W. Chou, L.-M. Duan, and H. J. Kimble. "Generation of nonclassical photon pairs for scalable quantum communication with atomic ensembles". In: *Nature* 423.6941 (June 2003), pp. 731–734. ISSN: 1476-4687. DOI: 10.1038/nature01714.

[89] D. Bozyigit, C. Lang, L. Steffen, J. M. Fink, C. Eichler, M. Baur, R. Bianchetti, P. J. Leek, S. Filipp, M. P. da Silva, A. Blais, and A. Wallraff. "Antibunching of microwave-frequency photons observed in correlation measurements using linear detectors". In: *Nat. Phys.* 7.2 (Feb. 2011), pp. 154–158. ISSN: 1745-2481. DOI: 10.1038/nphys1845.

[90] B. Kannan, D. L. Campbell, F. Vasconcelos, R. Winik, D. K. Kim, M. Kjaergaard, P. Krantz, A. Melville, B. M. Niedzielski, J. L. Yoder, T. P. Orlando, S. Gustavsson, and W. D. Oliver. "Generating spatially entangled itinerant photons with waveguide quantum electrodynamics". In: *Sci. Adv.* 6.41 (2020), eabb8780. DOI: 10.1126/sciadv.abb8780.

[91] V. S. Ferreira, G. Kim, A. Butler, H. Pichler, and O. Painter. *Deterministic Generation of Multidimensional Photonic Cluster States with a Single Quantum Emitter*. 2022. arXiv: 2206.10076.

[92] M. P. da Silva, D. Bozyigit, A. Wallraff, and A. Blais. "Schemes for the observation of photon correlation functions in circuit QED with linear detectors". In: *Phys. Rev. A* 82 (4 Oct. 2010), p. 043804. DOI: 10.1103/PhysRevA.82.043804.

[93] S. M. Barnett, G. Ferenczi, C. R. Gilson, and F. C. Speirits. "Statistics of photon-subtracted and photon-added states". In: *Phys. Rev. A* 98 (1 July 2018), p. 013809. DOI: 10.1103/PhysRevA.98.013809.

[94] J. Johansson, P. Nation, and F. Nori. "QuTiP 2: A Python framework for the dynamics of open quantum systems". In: *Computer Physics Communications* 184.4 (2013), pp. 1234–1240. ISSN: 0010-4655. DOI: https://doi.org/10.1016/j.cpc.2012.11.019.

[95] S. Hong, R. Riedinger, I. Marinković, A. Wallucks, S. G. Hofer, R. A. Norte, M. Aspelmeyer, and S. Gröblacher. "Hanbury Brown and Twiss interferometry of single phonons from an optomechanical resonator". In: *Science* 358.6360 (2017), pp. 203–206. DOI: 10.1126/science.aan7939. eprint: https://www.science.org/doi/pdf/10.1126/science.aan7939.

[96] I. Wilson-Rae, N. Nooshi, J. Dobrindt, T. J. Kippenberg, and W. Zwerger. "Cavity-assisted backaction cooling of mechanical resonators". In: *New Journal of Physics* 10.9 (Sept. 2008), p. 095007. DOI: 10.1088/1367-2630/10/9/095007.

[97] C. W. Gardiner and P. Zoller. *Quantum Noise*. Springer Series in Synergetics, Springer, 2004.

[98] L. Mandel and E. Wolf. *Optical coherence and quantum optics*. Cambridge university press, 1995.

[99] P. Kurpiers, P. Magnard, T. Walter, B. Royer, M. Pechal, J. Heinsoo, Y. Salathé, A. Akin, S. Storz, J.-C. Besse, S. Gasparinetti, A. Blais, and A. Wallraff. "Deterministic quantum state transfer and remote entanglement using microwave photons". In: *Nature* 558.7709 (June 2018), pp. 264–267. ISSN: 1476-4687. DOI: 10.1038/s41586-018-0195-y.

[100] R. D. Delaney, M. D. Urmey, S. Mittal, B. M. Brubaker, J. M. Kindem, P. S. Burns, C. A. Regal, and K. W. Lehnert. "Superconducting-qubit readout via low-backaction electro-optic transduction". In: *Nature* 606 (2022), pp. 489–493. DOI: 10.1038/s41586-022-04720-2.

[101] L.-M. Duan, M. D. Lukin, J. I. Cirac, and P. Zoller. "Long-distance quantum communication with atomic ensembles and linear optics". In: *Nature* 414 (Nov. 2001). Article, 413 EP -.

[102] S. Krastanov, H. Raniwala, J. Holzgrafe, K. Jacobs, M. Lončar, M. J. Reagor, and D. R. Englund. "Optically Heralded Entanglement of Superconducting Systems in Quantum Networks". In: *Phys. Rev. Lett.* 127 (4 July 2021), p. 040503. DOI: 10.1103/PhysRevLett.127.040503.

[103] M. Kjaergaard, M. E. Schwartz, J. Braumüller, P. Krantz, J. I.-J. Wang, S. Gustavsson, and W. D. Oliver. "Superconducting Qubits: Current State of Play". In: *Annual Review of Condensed Matter Physics* 11.1 (2020), pp. 369–395. DOI: 10.1146/annurev-conmatphys-031119-050605.

[104] P. Chiappina, J. Banker, S. Meesala, D. Lake, S. Wood, and O. Painter. "Design of an ultra-low mode volume piezo-optomechanical quantum transducer". In: *Opt. Express* 31.14 (July 2023), pp. 22914–22927. DOI: 10.1364/OE.493532.

[105] W. Jiang, F. M. Mayor, S. Malik, R. Van Laer, T. P. McKenna, R. N. Patel, J. D. Witmer, and A. H. Safavi-Naeini. *Optically heralded microwave photons*. 2022. arXiv: 2210.10739.

[106] H. Zhao, A. Bozkurt, and M. Mirhosseini. "Electro-optic transduction in silicon via gigahertz-frequency nanomechanics". In: *Optica* 10.6 (June 2023), pp. 790–796. DOI: 10.1364/OPTICA.479162.

[107] H. Ren, M. H. Matheny, G. S. MacCabe, J. Luo, H. Pfeifer, M. Mirhosseini, and O. J. Painter. "Two-dimensional optomechanical crystal cavity with high quantum cooperativity". In: *Nat. Comm.* 11.1 (July 2020). ISSN: 2041-1723.

[108] D. L. Moehring, P. Maunz, S. Olmschenk, K. C. Younge, D. N. Matsukevich, L.-M. Duan, and C. Monroe. "Entanglement of single-atom quantum bits at a distance". In: *Nature* 449.7158 (Sept. 2007), pp. 68–71. ISSN: 1476-4687. DOI: 10.1038/nature06118.

[109] J. Hofmann, M. Krug, N. Ortegel, L. Gérard, M. Weber, W. Rosenfeld, and H. Weinfurter. "Heralded Entanglement Between Widely Separated Atoms". In: *Science* 337.6090 (2012), pp. 72–75. DOI: 10.1126/science.1221856.

[110] H. Bernien, B. Hensen, W. Pfaff, G. Koolstra, M. Blok, L. Robledo, T. H. Taminiau, M. Markham, D. J. Twitchen, L. Childress, and R. Hanson. "Heralded entanglement between solid-state qubits separated by three metres". In: *Nature* 497.7447 (May 2013), pp. 86–90. DOI: 10.1038/nature12016.

[111] A. Delteil, Z. Sun, W.-b. Gao, E. Togan, S. Faelt, and A. Imamoğlu. "Generation of heralded entanglement between distant hole spins". In: *Nature Physics* 12.3 (Mar. 2016), pp. 218–223. ISSN: 1745-2481. DOI: 10.1038/nphys3605.

[112] R. Riedinger, A. Wallucks, I. Marinković, C. Löschnauer, M. Aspelmeyer, S. Hong, and S. Gröblacher. "Remote quantum entanglement between two micromechanical oscillators". In: *Nature* 556.7702 (Apr. 2018), pp. 473–477. ISSN: 1476-4687. DOI: 10.1038/s41586-018-0036-z.

[113] S. D. Barrett and P. Kok. "Efficient high-fidelity quantum computation using matter qubits and linear optics". In: *Phys. Rev. A* 71 (6 June 2005), p. 060310. DOI: 10.1103/PhysRevA.71.060310.

[114] B. B. Blinov, D. L. Moehring, L.-. M. Duan, and C. Monroe. "Observation of entanglement between a single trapped atom and a single photon". In: *Nature* 428.6979 (Mar. 2004), pp. 153–157. ISSN: 1476-4687. DOI: 10.1038/nature02377.

[115] E. Togan, Y. Chu, A. S. Trifonov, L. Jiang, J. Maze, L. Childress, M. V. G. Dutt, A. S. Sørensen, P. R. Hemmer, A. S. Zibrov, and M. D. Lukin. "Quantum entanglement between an optical photon and a solid-state spin qubit". In: *Nature* 466.7307 (Aug. 2010), pp. 730–734. ISSN: 1476-4687. DOI: 10.1038/nature09256.

[116] W. B. Gao, P. Fallahi, E. Togan, J. Miguel-Sanchez, and A. Imamoglu. "Observation of entanglement between a quantum dot spin and a single photon". In: *Nature* 491.7424 (Nov. 2012), pp. 426–430. ISSN: 1476-4687. DOI: 10.1038/nature11573.

[117] R. Sahu, L. Qiu, W. Hease, G. Arnold, Y. Minoguchi, P. Rabl, and J. M. Fink. "Entangling microwaves with light". In: *Science* 380.6646 (2023), pp. 718–721. DOI: 10.1126/science.adg3812.

[118] P. Kurpiers, M. Pechal, B. Royer, P. Magnard, T. Walter, J. Heinsoo, Y. Salathé, A. Akin, S. Storz, J.-C. Besse, S. Gasparinetti, A. Blais, and A. Wallraff. "Quantum Communication with Time-Bin Encoded Microwave Photons". In: *Phys. Rev. Appl.* 12 (4 Oct. 2019), p. 044067. DOI: 10.1103/PhysRevApplied.12.044067.

[119] S. Meesala, S. Wood, D. P. Lake, P. Chiappina, C. Zhong, A. D. Beyer, M. D. Shaw, L. Jiang, and O. J. Painter. *Non-classical microwave-optical photon pair generation with a chip-scale transducer*. 2023. arXiv: 2303.17684.

[120] I. Marcikic, H. de Riedmatten, W. Tittel, H. Zbinden, M. Legré, and N. Gisin. "Distribution of Time-Bin Entangled Qubits over 50 km of Optical Fiber". In: *Phys. Rev. Lett.* 93 (18 Oct. 2004), p. 180502. DOI: 10.1103/PhysRevLett.93.180502.

[121] A. Zivari, N. Fiaschi, R. Burgwal, E. Verhagen, R. Stockill, and S. Gröblacher. "On-chip distribution of quantum information using traveling phonons". In: *Science Advances* 8.46 (2022), eadd2811.

[122] G. Arnold and T. Werner. *All-optical single-shot readout of a superconducting qubit*. Sept. 2023. arXiv: 2310.16817 [quant-ph].

[123] H. K. Warner, J. Holzgrafe, B. Yankelevich, D. Barton, S. Poletto, C. J. Xin, N. Sinclair, D. Zhu, E. Sete, B. Langley, E. Batson, M. Colangelo, A. Shams-Ansari, G. Joe, K. K. Berggren, L. Jiang, M. Reagor, and M. Loncar. *Coherent control of a superconducting qubit using light*. 2023. arXiv: 2310.16155 [quant-ph].

[124] T. C. van Thiel, M. J. Weaver, F. Berto, P. Duivestein, M. Lemang, K. Schuurman, M. Žemlička, F. Hijazi, A. C. Bernasconi, E. Lachman, M. Field, Y. Mohan, F. de Vries, N. Bultink, J. van Oven, J. Y. Mutus, R. Stockill, and S. Gröblacher. *High-fidelity optical readout of a superconducting qubit using a scalable piezo-optomechanical transducer*. 2023. arXiv: 2310.06026 [quant-ph].

[125] M. K. Bhaskar, R. Riedinger, B. Machielse, D. S. Levonian, C. T. Nguyen, E. N. Knall, H. Park, D. Englund, M. Lončar, D. D. Sukachev, and M. D. Lukin. "Experimental demonstration of memory-enhanced quantum communication". In: *Nature* 580.7801 (Apr. 2020), pp. 60–64. ISSN: 1476-4687. DOI: 10.1038/s41586-020-2103-5.

[126] J.-P. Chen, C. Zhang, Y. Liu, C. Jiang, W.-J. Zhang, Z.-Y. Han, S.-Z. Ma, X.-L. Hu, Y.-H. Li, H. Liu, F. Zhou, H.-F. Jiang, T.-Y. Chen, H. Li, L.-X. You, Z. Wang, X.-B. Wang, Q. Zhang, and J.-W. Pan. "Twin-field quantum key distribution over a 511 km optical fibre linking two distant metropolitan areas". In: *Nature Photonics* 15.8 (Aug. 2021), pp. 570–575. ISSN: 1749-4893. DOI: 10.1038/s41566-021-00828-5.

[127] M. Pompili, C. Delle Donne, I. te Raa, B. van der Vecht, M. Skrzypczyk, G. Ferreira, L. de Kluijver, A. J. Stolk, S. L. N. Hermans, P. Pawełczak, W. Kozlowski, R. Hanson, and S. Wehner. "Experimental demonstration of entanglement delivery using a quantum network stack". In: *npj Quantum Information* 8.1 (Oct. 2022), p. 121. ISSN: 2056-6387. DOI: 10.1038/s41534-022-00631-2.

[128] D. Gottesman, T. Jennewein, and S. Croke. "Longer-Baseline Telescopes Using Quantum Repeaters". In: *Phys. Rev. Lett.* 109 (7 Aug. 2012), p. 070503. DOI: 10.1103/PhysRevLett.109.070503.

[129] E. T. Khabiboulline, J. Borregaard, K. De Greve, and M. D. Lukin. "Optical Interferometry with Quantum Networks". In: *Phys. Rev. Lett.* 123 (7 Aug. 2019), p. 070504. DOI: 10.1103/PhysRevLett.123.070504.

[130] B. C. Nichol, R. Srinivas, D. P. Nadlinger, P. Drmota, D. Main, G. Araneda, C. J. Ballance, and D. M. Lucas. "An elementary quantum network of entangled optical atomic clocks". In: *Nature* 609.7928 (Sept. 2022), pp. 689–694. ISSN: 1476-4687. DOI: 10.1038/s41586-022-05088-z.

[131] M. F. Volk, S. Suntsov, C. E. Rüter, and D. Kip. "Low loss ridge waveguides in lithium niobate thin films by optical grade diamond blade dicing". In: *Opt. Express* 24.2 (2016), pp. 1386–1391.

[132] N. Courjal, B. Guichardaz, G. Ulliac, J.-Y. Rauch, B. Sadani, H.-H. Lu, and M.-P. Bernal. "High aspect ratio lithium niobate ridge waveguides fabricated by optical grade dicing". In: *J. Phys. D: Appl. Phys.* 44.30 (2011), p. 305101.

[133] R. Wu, J. Lin, M. Wang, Z. Fang, W. Chu, J. Zhang, J. Zhou, and Y. Cheng. "Fabrication of a multifunctional photonic integrated chip on lithium niobate on insulator using femtosecond laser-assisted chemomechanical polish". In: *Opt. Lett.* 44.19 (2019), pp. 4698–4701.

[134] M. Wang, R. Wu, J. Lin, J. Zhang, Z. Fang, Z. Chai, and Y. Cheng. "Chemo-mechanical polish lithography: A pathway to low loss large-scale photonic integration on lithium niobate on insulator". In: *Quantum Eng.* 1.1 (2019), e9.

[135] J.-x. Zhou, R.-h. Gao, J. Lin, M. Wang, W. Chu, W.-b. Li, D.-f. Yin, L. Deng, Z.-w. Fang, J.-h. Zhang, et al. "Electro-optically switchable optical true delay lines of meter-scale lengths fabricated on lithium niobate on insulator using photolithography assisted chemo-mechanical etching". In: *Chin. Phys. Lett* 37.8 (2020), p. 084201.

[136] K. Nassau, H. J. Levinstein, and G. M. Loiacono. "The domain structure and etching of ferroelectric lithium niobate". In: *Appl. Phys. Lett.* 6.11 (1965), pp. 228–229.

[137] F. Laurell, J. Webjorn, G. Arvidsson, and J. Holmberg. "Wet etching of proton-exchanged lithium niobate-a novel processing technique". In: *J. Lightwave Technol.* 10.11 (1992), pp. 1606–1609.

[138] H. Hu, R. Ricken, W. Sohler, and R. Wehrspohn. "Lithium niobate ridge waveguides fabricated by wet etching". In: *IEEE Photonics Technol. Lett.* 19.6 (2007), pp. 417–419.

[139] Y. Li, T. Lan, D. Yang, M. Xiang, J. Dai, C. Li, and Z. Wang. "Research of selective etching in LiNbO3 using proton-exchanged wet etching technique". In: *Mater. Res. Express* 7.5 (2020), p. 056202.

[140] A. B. Randles, M. Esashi, and S. Tanaka. "Etch rate dependence on crystal orientation of lithium niobate". In: *IEEE Trans. Ultrason. Ferroelectr. Freq. Control* 57.11 (2010), pp. 2372–2380.

[141] C. L. Sones, S. Mailis, W. S. Brocklesby, R. W. Eason, and J. R. Owen. "Differential etch rates in z-cut LiNbO 3 for variable HF/HNO 3 concentrations". In: *J. Mater. Chem.* 12.2 (2002), pp. 295–298.

[142] R. Geiss, J. Brandt, H. Hartung, A. Tünnermann, T. Pertsch, E.-B. Kley, and F. Schrempel. "Photonic microstructures in lithium niobate by potassium hydroxide-assisted ion beam-enhanced etching". In: *J. Vac. Sci. Technol. B* 33.1 (2015), p. 010601.

[143] H. Hu, A. P. Milenin, R. B. Wehrspohn, H. Hermann, and W. Sohler. "Plasma etching of proton-exchanged lithium niobate". In: *J. Vac. Sci. Technol. A* 24.4 (2006), pp. 1012–1015.

[144] H. Nagata, N. Mitsugi, K. Shima, M. Tamai, and E. M. Haga. "Growth of crystalline LiF on CF4 plasma etched LiNbO3 substrates". In: *J. Cryst. Growth* 187.3-4 (1998), pp. 573–576.

[145] Z. Ren, P. J. Heard, J. M. Marshall, P. A. Thomas, and S. Yu. "Etching characteristics of LiNbO 3 in reactive ion etching and inductively coupled plasma". In: *J. Appl. Phys.* 103.3 (2008), p. 034109.

[146] D. Jun, J. Wei, C. Eng Png, S. Guangyuan, J. Son, H. Yang, and A. J. Danner. "Deep anisotropic LiNbO3 etching with SF6/Ar inductively coupled plasmas". In: *J. Vac. Sci. Technol. B* 30.1 (2012), p. 011208.

[147] W.-S. Tan, G. W. Fang, G. Pillai, C.-C. Chen, C.-Y. Chen, C.-H. Chin, and S.-S. Li. "Fabrication and characterization of lithium-niobate thin film MEMS piezoelectric resonators". In: *2016 IEEE 11th Annual International Conference on Nano/Micro Engineered and Molecular Systems (NEMS)*. IEEE. 2016, pp. 516–519.

[148] G. Si, A. J. Danner, S. L. Teo, E. J. Teo, J. Teng, and A. A. Bettiol. "Photonic crystal structures with ultrahigh aspect ratio in lithium niobate fabricated by focused ion beam milling". In: *J. Vac. Sci. Technol. B* 29.2 (2011), p. 021205.

[149] F. Lacour, N. Courjal, M.-P. Bernal, A. Sabac, C. Bainier, and M. Spajer. "Nanostructuring lithium niobate substrates by focused ion beam milling". In: *Opt. Mater.* 27.8 (2005), pp. 1421–1425.

[150] P. Arrangoiz-Arriola, E. A. Wollack, M. Pechal, J. D. Witmer, J. T. Hill, and A. H. Safavi-Naeini. "Coupling a superconducting quantum circuit to a phononic crystal defect cavity". In: *Phys. Rev. X* 8.3 (2018), p. 031007.

[151] C. Wang, M. Zhang, B. Stern, M. Lipson, and M. Lončar. "Nanophotonic lithium niobate electro-optic modulators". In: *Opt. Express* 26.2 (2018), pp. 1547–1555.

[152] M. Zhang, C. Wang, R. Cheng, A. Shams-Ansari, and M. Lončar. "Monolithic ultra-high-Q lithium niobate microring resonator". In: *Optica* 4.12 (2017), pp. 1536–1537.

[153] G. Ulliac, V. Calero, A. Ndao, F. I. Baida, and M.-P. Bernal. "Argon plasma inductively coupled plasma reactive ion etching study for smooth sidewall thin film lithium niobate waveguide application". In: *Opt. Mater.* 53 (2016), pp. 1–5.

[154] H. Robbins and B. Schwartz. "Chemical Etching of Silicon". In: *J. Electrochem. Soc.* 106.6 (1959), p. 505.